NIST Technical Note

NIST TN 2362

The Burning Character of 3 m to 7 m Douglas-Fir Trees with Varying Moisture Content

Giovanni Di Cristina
Erik Johnsson
Eric Mueller
Matthew Bundy
Anthony Chakalis
Marco Fernandez
Artur Chernovsky
Aika Davis
Anthony Hamins

This publication is available free of charge from:
https://doi.org/10.6028/NIST.TN.2362

NIST NATIONAL INSTITUTE OF STANDARDS AND TECHNOLOGY
U.S. DEPARTMENT OF COMMERCE

NIST Technical Note

NIST TN 2362

The Burning Character of 3 m to 7 m Douglas-Fir Trees with Varying Moisture Content

Giovanni Di Cristina
Erik Johnsson
Eric Mueller
Matthew Bundy
Anthony Chakalis
Marco Fernandez
Artur Chernovsky
Aika Davis
Anthony Hamins

Fire Research Division
Engineering Laboratory

This publication is available free of charge from:
https://doi.org/10.6028/NIST.TN.2362

June 2026

U.S. Department of Commerce
Howard Lutnick, Secretary
National Institute of Standards and Technology
Arvind Rman, NIST Director and Under Secretary of Commerce for Standards and Technology

NIST TN 2362

June 2026

NIST Technical Series Policies

Copyright, Use, and Licensing Statements

NIST Technical Series Publication Identifier Syntax

Publication History

Approved by the NIST Editorial Review Board on 2026-01-26

How to Cite this NIST Technical Series Publication

Cristina GD, Johnsson E, Mueller E, Bundy M, Chakalis A, Fernandez M, Chernovsky A, Davis A, Hamins A. (2026) The Burning Character of 3 m to 7 m Douglas-Fir Trees with Varying Moisture Content. (National Institute of Standards and Technology, Gaithersburg, MD), NIST Technical Note (TN) NIST TN 2362. https://doi.org/10.6028/NIST.TN.2362

Author ORCID iDs

Giovanni Di Cristina Torres: 0000-0002-0799-3418
Erik Johnsson: 0000-0003-1170-7370
Eric Mueller: 0000-0002-0838-6820
Matthew Bundy: 0000-0002-1138-0307
Anthony Chakalis: 0009-0004-4331-7101
Marco Fernandez: 0000-0002-4227-8866
Artur Chernovsky: 0000-0002-1215-7350
Aika Davis: 0000-0001-8620-5311
Anthony Hamins: 0000-0001-7531-4256

Contact Information:
anthony.hamins@nist.gov

Abstract

A series of experiments is reported on the burning behavior of 3.3 m to 7.4 m tall, Douglas-fir trees with the dry basis moisture content varying from 7 % to 55 %. The results quantified the transient, peak, and total heat release rates (HRR) as well as the mass loss, the yields of carbon monoxide, particulate matter, and PAH, and the near and far-field heat fluxes. Photogrammetry documented the initial and final tree geometry and characterized the crown volume, while cameras recorded multiple perspectives of the fire's evolution.

The fires exhibited rapid growth, reaching peak HRRs within 7 s to 18 s after ignition with vertical flame spread as fast as 2 m/s. Higher moisture content was found to significantly decrease both the radiative fraction and the particulate matter yield. The total heat release measured by oxygen consumption calorimetry and the ideal heat release from mass loss were in reasonable agreement. Post-fire analysis revealed thicker branch tip diameters as smaller fuel elements were consumed. The results provide unique calorimetric data useful for development of design fire scenarios and fire research and are available on the NIST Fire Calorimetry Database (FCD).

Keywords

burning rate; Douglas-fir trees; fire calorimetry database; heat release rate; radiative emission

Preface

This report extends the study by Johnsson et al. [2025], which reported fire experiments on three pairs of dry Douglas-fir trees. Johnsson et al. [2025] reported on the burning of 4 m (Trees 1 and 2), 4.5 m (Trees 3 and 4), and 6 m (Trees 5 and 6) tree specimens. Although natural variation existed among each pair, the pairs had similar widths and masses. These first six trees were conditioned to 8 % - 13 % moisture content on a dry basis (MC).

This report expands the original 6 tree dataset with 12 additional experiments investigating fires burning 6 m to 7 m Douglas-fir trees conditioned to obtain a range of moisture content targets. The second series included six trees tested at moderate moisture levels (30 % to 55 % MC). The third series included trees at relatively low moisture levels (15 % to 22 % MC). This report compares and contrasts the measurement results from all 18 Douglas-fir tree fire experiments. In addition to calorimetry, mass loss, the optically determined soot yield, the CO yield, and the near- and far-field heat fluxes, measurements on three trees also included gravimetrically determined soot yield and detailed analysis of the types of PAHs measured in the exhaust.

Table of Contents

Abstract ..... **iii**
Preface ..... **iv**
List of Figures ..... **vii**
List of Tables ..... **xvi**
Acknowledgements ..... **xviii**
1. Introduction **1**
1.1. Previous Work 2
2. Experimental Apparatus and Procedure **4**
2.1. Experimental Setup 4
2.2. Specimens 6
2.3. Instrumentation 7
2.3.1. Calorimetry 8
2.3.2. Moisture Content 8
2.3.3. Mass Loss 9
2.3.4. Heat Flux to Targets 10
2.3.4.1. Heat Flux Gauges 10
2.3.4.2. Plate Thermometers 11
2.3.5. Yield of Exhaust Products 13
2.3.6. Visual Record 15
2.3.7. Photogrammetric Characterization 16
2.4. Early Test Preparation 19
2.4.1. Tree Stands 19
2.5. Ignition Method 20
2.5.1. Burner Description 20
2.5.2. Ignition Description 22
2.6. Test Procedure 22
2.7. Post-Test Procedure 23
3. Results and Discussion **24**
3.1. Summary of Experiments 24

3.2. Mass Loss 26
3.3. Calorimetry 27
3.3.1. Near-field Heat Flux 34
3.3.2. Far-field Heat Flux 36
3.4. Total Radiated Energy and Radiative Fraction 38
3.5. Yield of Exhaust Products 42
3.6. Analysis of Branch Tips 45
4. Summary and Conclusions 49
5. References 51
Appendix A. Photos of Test Specimens Before, During, and After Testing 57
Appendix B. Calorimetry 93
Appendix C. Mass Loss 102
Appendix D. Heat Flux 109
D.1. Heat Flux Gauge and Plate Thermometer Comparisons 109
D.2. East and West Plate Thermometer Comparisons 115
D.3. Far-Field Heat Flux 121
Appendix E. Uncertainty in Photogrammetry Measurements 131
Appendix F. Gravimetric Particulate Matter and PAH Analysis 135
Appendix G. Correcting the Heat Release Rates for the Calorimetry Time Response 137
G.1. Uncertainty Estimate of $HRR'q(t = tpeak)$ 139
G.2. Uncertainty Estimate of $HRR'\boldsymbol{m}(t = tpeak)$ 141
G.3. Uncertainty Estimate of the Time of the Peak Heat Release Rate 143

List of Figures

Figure 1. Floor plan of the National Fire Research Laboratory's Room 125, housing the 20 MW exhaust hood. 4

Figure 2. A scale plan view drawing of the area under the 13.8 m × 15.4 m canopy hood showing instrumentation locations. 5

Figure 3. A photo of the front of the 10 cm x 10 cm modified plate thermometer.....12

Figure 4. Example of process for photogrammetric characterization of Tree 1. (a) Raw scan data in the form of a 3-dimensional point cloud. (b) A horizontal slice (blue plane in (a)) of voxels containing points. Voxels inside an ellipse fit to the point cloud, using total least squares, are also filled. (c) Voxelized representation of the whole crown volume. (d) Major and minor crown radius were determined by fitting an ellipse with the same normalized second central moment as the projection of the voxelized crown geometry in the z-direction. 17

Figure 5. Comparison of the maximum widths and heights determined by photogrammetry versus photography. 18

Figure 6. A photograph of the tree stand on the load cell platform. 19

Figure 7. A photograph of the plywood tree platform prior to mounting the tree. 20

Figure 8. The first version of the burner used for the shortest trees. 21

Figure 9. An early version of the burner with flames. 21

Figure 10. Flame spread evolution during testing of Tree 6 from ignition (t = 0 s) to 60 s after ignition. The images at 0 s, 2 s, and 60 s have been brightened to enhance perception of the tree. The camera was positioned 8.7 m from the tree and angled upwards approximately 45° to capture the entire flame plume. 24

Figure 11. The ideal heat release determined from the total mass loss (corrected for water) versus the total heat released (THR) determined using O2 consumption calorimetry. The dotted line represents parity, and the error bars represent the expanded combined uncertainties representing a 95 % confidence interval. 30

Figure 12. The measured net heat of combustion as a function of the (fractional) dry moisture content. The error bars represent the combined expanded (k=2) uncertainty. The dotted line represents the average Hc,net for all the data in the plot, which agrees with the value determined by Susott [1982]. 31

Figure 13. The peak HRR and the THR as a function of tree height. Best fits to a power function are also shown. The average combined expanded uncertainties (k=2) of the peak and total HRRs are 8 %. 32

Figure 14. The peak HRR as a function of the THR. A best fit line is also shown. The average combined expanded uncertainties (k=2) of the peak and total HRRs are 8 %. 32

Figure 15. The peak HRR and the THR as a function of tree height. Best fits to a power function are also shown. The average combined expanded uncertainties (k=2) of the peak and total HRRs are 8 %.....33

Figure 16. The peak HRR and the THR as a function of moisture content (MC). The average combined expanded uncertainties (k=2) of the peak and total HRRs are both 8 %. 33

Figure 17. The ratio of the peak HRR to initial mass as a function of moisture content measured in this study and compared to the results from Sung et al. [2026] and Babrauskas [2016]. A best fit power law function to all the data in the plot is also shown. 34

Figure 18. The near-field peak heat fluxes as a function of tree height for gauges located at three z positions. The average combined expanded (k=2) heat flux uncertainties were approximately 10 %. The results of Mell et al. [2009] are also shown. 35

Figure 19. The near-field heat flux as a function of moisture content. The average combined expanded heat flux uncertainties were approximately 10 %. 36

Figure 20. The peak far-field heat flux at r = 12 m measured by the northwest (NW) and southeast (SE) gauges as a function of the peak heat release rate. A best fit line forced through zero is also shown. The expanded (k=2) combined uncertainties are 8 % and 10 % for the peak HRR and peak far-field HF measurements, respectively. 36

Figure 21. The far-field (r=12 m) peak heat fluxes as a function of tree height. The average expanded (k=2) combined uncertainty of the peak heat flux was about 10 %. 37

Figure 22. The far-field (r=12 m) peak heat flux as a function of tree moisture content. The expanded (k=2) combined uncertainty of the peak heat flux was about 10 %. 38

Figure 23. The total radiated energy (TRE) as a function of the total heat released (THR) by the fire (from calorimetry). A best fit line forced through zero is also shown. The average combined expanded (k=2) uncertainties of the TRE and THR are 16 % and 8 %. 39

Figure 24. The total radiated energy at the NW and SE far-field heat flux gauges as a function of tree height. The average combined expanded (k=2) TRE uncertainty is 16 %. 40

Figure 25. The total radiated energy at the NW and SE far-field heat flux gauges as a function of the dry moisture content of the trees (MC in Table 1). The average combined expanded (k=2) uncertainty of the TRE is 16 %. 41

Figure 26. The radiative fraction as a function of dry moisture content of the trees. A best fit power law function to the data is also shown. The average combined expanded (k=2) uncertainty of χ_{rad} is 20 %. 42

Figure 27. The yields of CO and particulate matter as a function of the moisture content (MC). Best-fit lines are also shown. The average combined expanded (k=2) uncertainty of the CO and PM yields was 10 % and 17 %, respectively. 44

Figure 28. The ratio of the CO yield to the PM yield as a function of the moisture content. A best fit line to the data is also shown. The average combined expanded (k=2) uncertainty of the CO/PM ratio was 17 %.....45

Figure 29. Photographs of the progression of processing steps, removing needles from a branch tip to measure the stem thickness, then placing them on a light table for analysis. 46

Figure 30. Branch tip diameter versus distance above the tree stand base for Trees 8 and 12 before burning. 46

Figure 31. The branch tip diameter as a function of distance above the tree stand base for Tree 4 post-fire.....47

Figure 32. The branch tip diameter as a function of distance above the tree stand base for Tree 6 post-fire.....48

Figure A 1. Test 1 photo with dimensions of Tree 1.....57

Figure A 2. Test 2 photo with dimensions of Tree 2.....58

Figure A 3. Test 3 photo with dimensions of Tree 3.....59

Figure A 4. Test 4 photo with dimensions of Tree 4.....60

Figure A 5. Test 5 photo with dimensions of Tree 5.....61

Figure A 6. Test 6 photo with dimensions of Tree 6.....62

Figure A 7. Test 7 photo with dimensions of Tree 7.....63

Figure A 8. Test 8 photo with dimensions of Tree 8.....64

Figure A 9. Test 9 photo with dimensions of Tree 9.....65

Figure A 10. Test 10 photo with dimensions of Tree 10. 66

Figure A 11. Test 11 photo with dimensions of Tree 11. 67

Figure A 12. Test 12 photo with dimensions of Tree 12. 68

Figure A 13. Test 13 photo with dimensions of Tree 13. 69

Figure A 14. Test 14 photo with dimensions of Tree 14. 70

Figure A 15. Test 15 photo with dimensions of Tree 15. 71

Figure A 16. Test 16 photo with dimensions of Tree 16. 72

Figure A 17. Test 17 photo with dimensions of Tree 17. 73

Figure A 18. Test 18 photo with dimensions of Tree 18. 74

Figure A 19. Tree 1 during and after the test. 75

Figure A 20. Tree 2 during and after the test. 76

Figure A 21. Tree 3 during and after the test. 77
Figure A 22. Tree 4 during and after the test. 78
Figure A 23. Tree 5 during and after the test. 79
Figure A 24. Tree 6 during and after the test. 80
Figure A 25. Tree 7 during and after the test. 81
Figure A 26. Tree 8 during and after the test. 82
Figure A 27. Tree 9 during and after the test. 83
Figure A 28. Tree 10 during and after the test....84
Figure A 29. Tree 11 during and after the test....85
Figure A 30. Tree 12 during and after the test....86
Figure A 31. Tree 13 during and after the test....87
Figure A 32. Tree 14 during and after the test....88
Figure A 33. Tree 15 during and after the test....89
Figure A 34. Tree 16 during and after the test....90
Figure A 35. Tree 17 during and after the test....91
Figure A 36. Tree 18 during and after the test....92

Figure B1. The heat Release rate measurement using oxygen consumption calorimetry (in black) and the mass loss rate (MLR) calorimetry (in blue) for Tree 1. The MLR trace is based on the measured transient mass loss profile seen in Appendix C. 93
Figure B 2. The heat Release Rate measurement using oxygen consumption calorimetry (in black) and the mass loss rate (MLR) calorimetry (in blue) for Tree 2. The MLR trace is based on the measured transient mass loss profile seen in Appendix C. 93
Figure B 3. The heat release rate measurement using oxygen consumption calorimetry (in black) and the mass loss rate (MLR) calorimetry (in blue) for Tree 3. The MLR trace is based on the measured transient mass loss profile seen in Appendix C. 94
Figure B 4. The heat release rate measurement using oxygen consumption calorimetry (in black) and the mass loss rate (MLR) calorimetry (in blue) for Tree 4. The MLR trace is based on the measured transient mass loss profile seen in Appendix C. 94
Figure B 5. The heat release rate measurement using oxygen consumption calorimetry (in black) and the mass loss rate (MLR) calorimetry (in blue) for Tree 5. The MLR trace is based on the measured transient mass loss profile seen in Appendix C. 95

Figure B 6. The heat release rate measurement using oxygen consumption calorimetry (in black) and the mass loss rate (MLR) calorimetry (in blue) for Tree 6. The MLR trace is based on the measured transient mass loss profile seen in Appendix C. 95

Figure B 7. The heat release rate measurement using oxygen consumption calorimetry (in black) and the mass loss rate (MLR) calorimetry (in blue) for Tree 7. The MLR trace is based on the measured transient mass loss profile seen in Appendix C. 96

Figure B 8. The heat release rate measurement using oxygen consumption calorimetry for Tree 8. The time-resolved mass for Tree 10 is omitted (see explanation in Appendix C). 96

Figure B 9 The heat release rate measurement using oxygen consumption calorimetry for Tree 9. The time-resolved mass for Tree 10 is omitted (see explanation in Appendix C). 97

Figure B 10. The heat release rate measurement using oxygen consumption calorimetry for Tree 10. The time-resolved mass for Tree 10 is omitted (see explanation in Appendix C). 97

Figure B 11. The heat release rate measurement using oxygen consumption calorimetry for Tree 11. The time-resolved mass for Tree 10 is omitted (see explanation in Appendix C). 98

Figure B 12. The heat release rate measurement using oxygen consumption calorimetry for Tree 12. The time-resolved mass for Tree 10 is omitted (see explanation in Appendix C). 98

Figure B 13. The heat release rate measurement using oxygen consumption calorimetry (in black) and the mass loss rate (MLR) calorimetry (in blue) for Tree 13. The MLR trace is based on the measured transient mass loss profile seen in Appendix C. 99

Figure B 14. The heat release rate measurement using oxygen consumption calorimetry (in black) and the mass loss rate (MLR) calorimetry (in blue) for Tree 14. The MLR trace is based on the measured transient mass loss profile seen in Appendix C. 99

Figure B 15. The heat release rate measurement using oxygen consumption calorimetry (in black) and the mass loss rate (MLR) calorimetry (in blue) for Tree 15. The MLR trace is based on the measured transient mass loss profile seen in Appendix C. 100

Figure B 16. The heat release rate measurement using oxygen consumption calorimetry (in black) and the mass loss rate (MLR) calorimetry (in blue) for Tree 16. The MLR trace is based on the measured transient mass loss profile seen in Appendix C. 100

Figure B 17. The heat release rate measurement using oxygen consumption calorimetry (in black) and the mass loss rate (MLR) calorimetry (in blue) for Tree 17. The MLR trace is based on the measured transient mass loss profile seen in Appendix C. 101

Figure B 18. The heat release rate measurement using oxygen consumption calorimetry (in black) and the mass loss rate (MLR) calorimetry (in blue) for Tree 18. The MLR trace is based on the measured transient mass loss profile seen in Appendix C. 101

Figure C 1. Tree 1 transient load cell (wet) mass measurements with ignition at time zero. 102
Figure C 2. Tree 2 transient load cell (wet) mass measurements with ignition at time zero. 102
Figure C 3. Tree 3 transient load cell (wet) mass measurements with ignition at time zero. 103
Figure C 4. Tree 4 transient load cell (wet) mass measurements with ignition at time zero. 103
Figure C 5. Tree 5 transient load cell (wet) mass measurements with ignition at time zero. 104
Figure C 6. Tree 6 transient load cell (wet) mass measurements with ignition at time zero. 104
Figure C 7. Tree 7 transient load cell (wet) mass measurements with ignition at time zero. 105
Figure C 8. Tree 13 transient load cell (wet) mass measurements with ignition at time zero. 105
Figure C 9. Tree 14 transient load cell (wet) mass measurements with ignition at time zero. 106
Figure C 10. Tree 15 transient load cell (wet) mass measurements with ignition at time zero. 106
Figure C 11. Tree 16 transient load cell (wet) mass measurements with ignition at time zero. 107
Figure C 12. Tree 17 transient load cell (wet) mass measurements with ignition at time zero. 107
Figure C 13. Tree 18 transient load cell (wet) mass measurements with ignition at time zero. 108

Figure D 1. Tree 1 heat flux gauge and plate thermometer comparison. 109
Figure D 2. Tree 2 heat flux gauge and plate thermometer comparison. 109
Figure D 3. Tree 3 heat flux gauge and plate thermometer comparison. 110
Figure D 4. Tree 4 heat flux gauge and plate thermometer comparison. 110
Figure D 5. Tree 5 heat flux gauge and plate thermometer comparison. 110
Figure D 6. Tree 6 heat flux gauge and plate thermometer comparison. 111
Figure D 7. Tree 7 heat flux gauge and plate thermometer comparison. 111
Figure D 8. Tree 8 heat flux gauge and plate thermometer comparison. 111
Figure D 9. Tree 9 heat flux gauge and plate thermometer comparison. 112
Figure D 10. Tree 10 heat flux gauge and plate thermometer comparison. 112
Figure D 11. Tree 11 heat flux gauge and plate thermometer comparison. 112
Figure D 12. Tree 12 heat flux gauge and plate thermometer comparison. 113
Figure D 13. Tree 13 heat flux gauge and plate thermometer comparison. 113
Figure D 14. Tree 14 heat flux gauge and plate thermometer comparison. 113
Figure D 15. Tree 15 heat flux gauge and plate thermometer comparison. 114
Figure D 16. Tree 16 heat flux gauge and plate thermometer comparison. 114

Figure D 17. Tree 17 heat flux gauge and plate thermometer comparison. 114
Figure D 18. Tree 18 heat flux gauge and plate thermometer comparison. 115
Figure D 19. Tree 1 east and west PT comparisons. 115
Figure D 20. Tree 2 east and west PT comparisons. 115
Figure D 21. Tree 3 east and west PT comparisons. 116
Figure D 22. Tree 4 east and west PT comparisons. 116
Figure D 23. Tree 5 east and west PT comparisons. 116
Figure D 24. Tree 6 east and west PT comparisons. 117
Figure D 25. Tree 7 east and west PT comparisons 117
Figure D 26. Tree 8 east and west PT comparisons 117
Figure D 27. Tree 9 east and west PT comparisons 118
Figure D 28. Tree 10 east and west PT comparisons 118
Figure D 29. Tree 11 east and west PT comparisons 118
Figure D 30. Tree 12 east and west PT comparisons 119
Figure D 31. Tree 13 east and west PT comparisons 119
Figure D 32. Tree 14 east and west PT comparisons 119
Figure D 33. Tree 15 east and west PT comparisons 120
Figure D 34. Tree 16 east and west PT comparisons 120
Figure D 35. Tree 17 east and west PT comparisons 120
Figure D 36. Tree 18 east and west PT comparisons 121
Figure D 37. Tree 1 far-field heat fluxes. 121
Figure D 38. Tree 2 far-field heat fluxes. 122
Figure D 39. Tree 3 far-field heat fluxes. 122
Figure D 40. Tree 4 far-field heat fluxes. 123
Figure D 41. Tree 5 far-field heat fluxes. 123
Figure D 42. Tree 6 far-field heat fluxes. 124
Figure D 43. Tree 7 far-field heat fluxes 124
Figure D 44. Tree 8 far-field heat fluxes 125
Figure D 45. Tree 9 far-field heat fluxes 125
Figure D 46. Tree 10 far-field heat fluxes. 126

Figure D 47. Tree 11 far-field heat fluxes. 126

Figure D 48. Tree 12 far-field heat fluxes 127

Figure D 49. Tree 13 far-field heat fluxes 127

Figure D 50. Tree 14 far-field heat fluxes 128

Figure D 51. Tree 15 far-field heat fluxes 128

Figure D 52. Tree 16 far-field heat fluxes 129

Figure D 53. Tree 17 far-field heat fluxes 129

Figure D 54. Tree 18 far-field heat fluxes 130

Figure E 1. Photogrammetric model of reference object (east column in Figure 2). 131

Figure E 2. Raw point cloud from photogrammetric model in previous figure. The points corresponding to the reference measurements are highlighted in orange (reference length 1) and green (reference length 2). The calculated model distances are shown as dashed lines. 132

Figure F 1. The PAH yields for Tests 8 and 10. 136

Figure G 1. The measured transient heat release rate (HRR), the calculated HRR based on the measured transient mass loss rate, and the corrected HRR profiles for Tree 1 based on the measured transient heat flux and mass loss rate profiles using Eqs. G1 and G2. 145

Figure G 2. The measured transient heat release rate (HRR), the calculated HRR based on the measured transient mass loss rate, and the corrected HRR profiles for Tree 2 based on the measured transient heat flux and mass loss rate profiles using Eqs. G1 and G2. 145

Figure G 3. The measured transient heat release rate (HRR), the calculated HRR based on the measured transient mass loss rate, and the corrected HRR profiles for Tree 3 based on the measured transient heat flux and mass loss rate profiles using Eqs. G1 and G2. 146

Figure G 4. The measured transient heat release rate (HRR), the calculated HRR based on the measured transient mass loss rate, and the corrected HRR profiles for Tree 4 based on the measured transient heat flux and mass loss rate profiles using Eqs. G1 and G2. 146

Figure G 5. The measured transient heat release rate (HRR), the calculated HRR based on the measured transient mass loss rate, and the corrected HRR profiles for Tree 5 based on the measured transient heat flux and mass loss rate profiles using Eqs. G1 and G2. 147

Figure G 6. The measured transient heat release rate (HRR), the calculated HRR based on the measured transient mass loss rate, and the corrected HRR profiles for Tree 6 based on the measured transient heat flux and mass loss rate profiles using Eqs. G1 and G2. 147

Figure G 7. The measured transient heat release rate (HRR), the calculated HRR based on the measured transient mass loss rate, and the corrected HRR profiles for Tree 7 based on the measured transient heat flux and mass loss rate profiles using Eqs. G1 and G2. 148

Figure G 8. The measured transient heat release rate (HRR) and the corrected HRR profiles for Tree 8 based on the measured transient heat flux rate profile using Eq. G1. 148

Figure G 9. The measured transient heat release rate (HRR) and the corrected HRR profiles for Tree 9 based on the measured transient heat flux rate profile using Eq. G1. 149

Figure G 10. The measured transient heat release rate (HRR) and the corrected HRR profiles for Tree 10 based on the measured transient heat flux rate profile using Eq. G1. 149

Figure G 11. The measured transient heat release rate (HRR) and the corrected HRR profiles for Tree 11 based on the measured transient heat flux rate profile using Eq. G1. 150

Figure G 12. The measured transient heat release rate (HRR) and the corrected HRR profiles for Tree 12 based on the measured transient heat flux rate profile using Eq. G1. 150

Figure G 13. The measured transient heat release rate (HRR), the calculated HRR based on the measured transient mass loss rate, and the corrected HRR profiles for Tree 13 based on the measured transient heat flux and mass loss rate profiles using Eqs. G1 and G2. 151

Figure G 14. The measured transient heat release rate (HRR), the calculated HRR based on the measured transient mass loss rate, and the corrected HRR profiles for Tree 14 based on the measured transient heat flux and mass loss rate profiles using Eqs. G1 and G2. 151

Figure G 15. The measured transient heat release rate (HRR), the calculated HRR based on the measured transient mass loss rate, and the corrected HRR profiles for Tree 15 based on the measured transient heat flux and mass loss rate profiles using Eqs. G1 and G2. 152

Figure G 16. The measured transient heat release rate (HRR), the calculated HRR based on the measured transient mass loss rate, and the corrected HRR profiles for Tree 16 based on the measured transient heat flux and mass loss rate profiles using Eqs. G1 and G2. 152

Figure G 17. The measured transient heat release rate (HRR), the calculated HRR based on the measured transient mass loss rate, and the corrected HRR profiles for Tree 17 based on the measured transient heat flux and mass loss rate profiles using Eqs. G1 and G2. 153

Figure G 18. The measured transient heat release rate (HRR), the calculated HRR based on the measured transient mass loss rate, and the corrected HRR profiles for Tree 18 based on the measured transient heat flux and mass loss rate profiles using Eqs. G1 and G2. 153

List of Tables

Table 1. List of tree height and maximum width determined using photography, the initial tree mass corrected for moisture content (MC), and the measured dry basis MC percentage. 7

Table 2. Water-cooled heat flux gauge locations and descriptions. 11

Table 3. Plate thermometer locations. 13

Table 4. Video camera positions and typical settings. 15

Table 5. Tree dimensions determined from photogrammetry using a 5 cm voxel size. Uncertainties are reported as the combined expanded (k = 2) uncertainty, representing a 95 % confidence interval. ...18

Table 6. The nominal igniter (gas burner) duration, the total burner heat released, and the total heat released as a percentage of the fire THR. Uncertainties are reported as the combined expanded (k = 2) uncertainty, representing a 95 % confidence interval. 23

Table 7. Summary of experimental observations, including ignition and fire spread. 25

Table 8. Summary of test results including the fuel mass loss corrected for water content (Δm) and post-fire residual mass percentage. The peak HRR, time to peak HRR, total heat release (THR) measured by oxygen consumption calorimetry, and effective heat of combustion ($H_{c,net}$) are also listed. Uncertainties are reported as the combined expanded (k = 2) uncertainty, representing a 95 % confidence interval.....28

Table 9. The total radiated energy determined from the far-field NW and SE heat flux gauges and the radiative fraction, χ_{rad}. The average combined expanded (k = 2) uncertainty of TRE and χ_{rad} is 19 % and 23 %, respectively.....39

Table 10. The measured particulate matter (PM), carbon monoxide (CO), and carbon dioxide (CO_2) yields, the CO to PM ratio, and their combined expanded (k = 2) uncertainties. 42

Table E 1 Type A uncertainty in point cloud location based on measurement of reference distances. 132

Table E 2. Tree dimensions determined using a 10 cm voxel size, including the combined expanded (k=2) uncertainties, representing a 95 % confidence interval. 133

Table E 3. Tree dimensions determined using a 15 cm voxel size, including the combined expanded (k=2) uncertainties, representing a 95 % confidence interval. 134

Table F 1. Gravimetric and optical measurements of particulate matter yield and their ratio for Tests 7, 8, and 10. The MC from Table 1 is also listed. 135

Table G 1 The peak HRR, the time to the peak HRR, the rescaled values using Equations G1 and G2 (also see Eq. 6 from Di Cristina et al. [2025]). The THR from Table 8 is reproduced here. The expanded (k=2) uncertainties are also listed. 138

Table G 2. Summary of $ucMLR(tpeak)$ for Tests 1-7 and Tests 13-18. 142

Acknowledgements

The authors are grateful to Phillip Deardorff and Justin Mills of NIST for outstanding technical support during the test series and to Rodney Bryant for offering helpful suggestions and overseeing experimental safety for a number of the tests.

1. Introduction

A series of fire experiments is reported that investigates the burning characteristics of large trees under quasi-quiescent conditions. The objective of this study is to expand the NIST Fire Calorimetry Database (FCD) through measurements of the burning character of the fires with an emphasis on the transient heat release rate. The FCD contains hundreds of measurement results of fire experiments conducted since 2017 at NIST's National Fire Research Laboratory (NFRL). The FCD is used by fire protection engineers to support engineering analysis including performance-based design, as well as by fire safety science researchers interested in information about the burning of specific types of items. The specimens contained in the database include single burning items, fully furnished rooms, controlled burners, well-characterized fuels, and composite fuels typically of unknown composition. The focus of the FCD is the accuracy of the transient heat release rate (HRR) measurement and its uncertainty. A description of the calorimetry measurements and instrumentation is provided in Bryant and Bundy [2019]. The FCD includes a summary of the measurement results, their uncertainty, and the experimental conditions. In addition to the calorimetric results, the FCD provides measurement results on the yields of "soot," CO, and CO_2. For this series of tests, the FCD provides the initial dry specimen mass and its change during the experiment, with a correction applied to account for the water content of the fuel mass. The FCD also provides a list of input parameters and conditions characterizing the experiments.

The specimens selected for characterization in this study were Douglas-fir trees. Douglas-fir is an evergreen conifer species (*Pseudotsuga menziesii*) and a member of the pine family that contains soft, flat needles roughly 1 cm to 4 cm in length. It was selected for study as it is a common tree species in the Western United States and easily obtainable throughout the year.

The burning rate of a tree fire is influenced by many physical, geometric, and ignition scenario attributes. These include a specimen's dryness, dimensions, configuration, the environmental conditions (humidity, temperature, wind, etc.), and the strength and location of the ignition source, among other parameters. It is impossible to provide test results for every conceivable permutation of these parameters. Nevertheless, the heat release rates reported in this study can be useful in guiding engineering analysis and for providing a reference for validation and application of fire models.

The main body of this report is broken into five sections. The remainder of this introduction presents a brief review of previous studies on tree fires. Section 2 describes the experimental methods including the ignition scenarios and describes the test specimens. Section 3 presents an overview of the experimental results including an estimate of the radiative fraction. Section 4

summarizes the results and findings. Section 5 presents the references cited in this report. Six appendices accompany this report. Appendix A contains photos with overlaid dimensions and a description of each of the specimens. Appendix B presents the transient calorimetry data. Appendix C shows plots of the transient mass loss. Appendix D presents the near-and far-field transient heat flux measurements. Appendix E discusses the uncertainty of the photogrammetry method. Appendix F describes the PAH in the fire plume. Appendix G presents the results of an analysis correcting the measured HRR results for the calorimetry measurement system's time response.

As described in the next subsection, there have been many previous studies on the burning of vegetation and some studies on the burning of Douglas-fir trees. The experiments conducted in this study complement previous research, providing comprehensive calorimetric information with reported uncertainty as well as a full video record of large tree fires burning under fully ventilated quasi-quiescent conditions.

1.1. Previous Work

A significant amount of work has been conducted on tree burning. Mell et al. [2009] measured the mass loss and local heat flux to targets 2 m and 3 m away from the center of 2 m and 5 m tall Douglas-fir trees. The study investigated how various factors, such as moisture content and tree size, affect the burning rate and heat flux. Completeness of the burning of Douglas-fir differed according to three ranges of moisture content (MC) on a dry basis: MC < 30 %, 30 % < MC < 70 %, and MC > 70 %, with the lowest moisture content trees burning well and the high moisture content trees not burning at all. The results revealed that higher moisture levels significantly reduced the fire heat release rate, underscoring the importance of moisture content in wildfire management.

The importance of moisture content is considered in many studies. Schneider et al. [2021] tested the possibility of fire spread by radiation from adjacent burning trees. Three trees spaced 20 cm to 30 cm apart from the nearest branches of the target tree and positioned around the target tree were simultaneously ignited using gas burners. Only about half of the experiments led to ignition of the target tree. Measurements of the mass loss rates and local heat fluxes found that the target tree's moisture content affected the propensity for its ignition.

Moisture content has also been the focus of experiments investigating the heat release rate of dry "Christmas" trees, showing that keeping a tree watered reduces fire risk [Bigda 2021; Hoehler 2020]. Accary et al. [2024] conducted five experiments measuring the mass burning rate of very dry (6 % ≤ MC ≤ 9 %), 2 m tall, (individual) Douglas-fir trees burning in the open under fully-ventilated conditions. The trees were ignited using a 0.8 m hexagonal-shaped methane gas

burner placed 30 cm below the tree base. The near-field heat flux and centerline temperature measurements were compared to simulations using four commonly used computational fluid dynamics fire models. The experiments and simulations showed that the HRR profile is very sensitive to the ignition protocol. Accary [2024] concludes that the ignition event must be well-controlled to ensure experimental repeatability.

Babrauskas [2001] conducted an extensive number of fire experiments investigating the HRR of single 2 m tall Douglas-fir trees that were placed in a watering stand. Various watering programs were used such that the tree moisture content on a dry basis varied from about 3 % to 160 %. The trees were positioned in a room corner configuration for fire testing. The ratio of the measured peak HRRs to the dry mass of the trees was found to be roughly proportional to the reciprocal of the foliar moisture content. This same correlation held for various species of burning shrubs burning under well-ventilated conditions. Babrauskas [2016] concludes that the main variables affecting the HRR of “Christmas” trees are the moisture content of the needles, the mass of the tree, the species type, and the ignition source used.

Modarres et al. [2024] burned a series of single, small, Eucalyptus trees of different ages, varying between 6 months and 5 years. The moisture content ranged between 74 % and 152 % and varied with age and tree component (e.g. foliage versus branches). The trees were burned by igniting trays of alcohol at their base. Measurements included the mass loss rate, the centerline plume temperatures, and heat flux to a nearby target. Older trees were found to burn for a shorter duration with a higher peak mass loss rate and higher peak heat flux, which was attributed to their lower relative moisture content.

Sung et al. [2026] recently conducted a series of experiments on a number of vegetative fuels including individual, 0.9 m to 1.8 m tall, Douglas-fir trees. The measurements mirror many of the measurements conducted in this study and the results for smaller trees complement the results presented here. Few other studies have measured the particulate matter and carbon monoxide (CO) yields from burning trees and none found in a literature review have reported on the far-field heat flux[1] and the radiative fraction of the fire. In addition, except for Mell et al. [2009], all previous studies were limited to a tree height of nominally 2 m or less.

[1] Far-field refers to distances sufficiently far from the source such that a single location radiative flux measurement allows estimation of the radiative fraction of a fire.

2. Experimental Apparatus and Procedure

The experiments described here investigated 18 large (approximately 3 m to 7 m tall) Douglas-fir trees under well-ventilated, quasi-quiescent conditions (without an applied wind field). The experiments were conducted under the 20 MW exhaust hood calorimeter at NIST's National Fire Research Laboratory (NFRL). A schematic of the hood and laboratory space is shown in Fig. 1. The subsections below elaborate on the hood and describe the setup, instrumentation, and details of the experimental series.

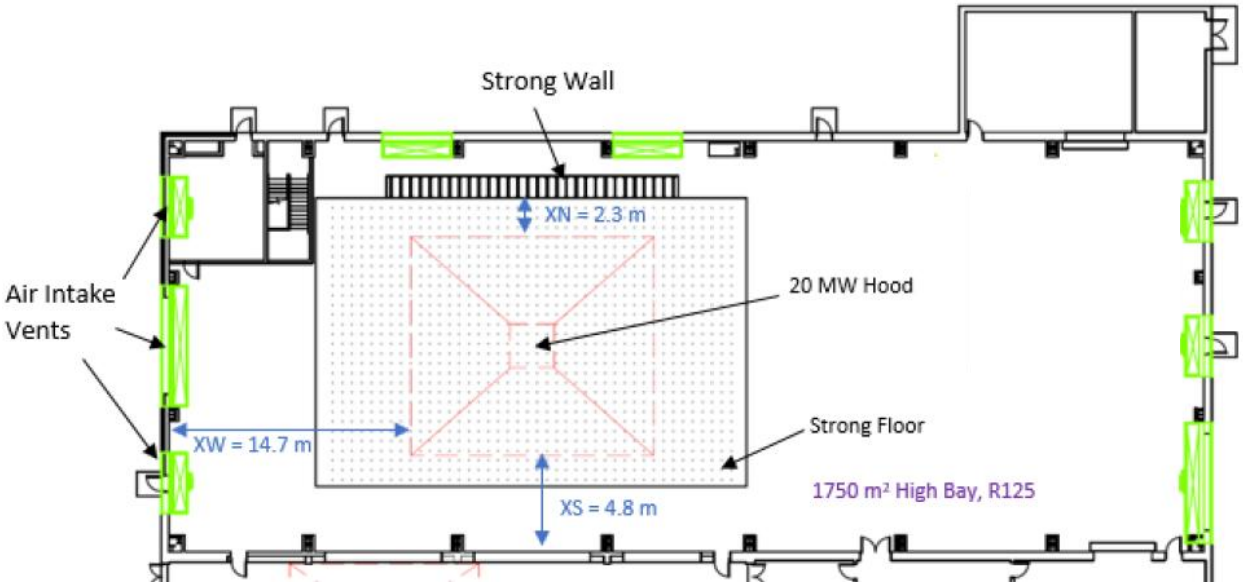

Figure 1. Floor plan of the National Fire Research Laboratory's Room 125, housing the 20 MW exhaust hood.

2.1. Experimental Setup

The trees were burned one at a time under a large capacity calorimeter that can handle 20 MW of continuous heat release rate. A 13.8 m × 15.4 m canopy hood captures the products of combustion for quantification of the heat release as a function of time. A large round exhaust duct (2.4 m diameter) is located 15.3 m above the floor.

Figure 2 shows a plan view of the experimental setup under the 13.8 m × 15.4 m canopy hood. The instrumentation and attachment I-beam columns are shown in their relative positions. The test specimen was placed directly below the center of the exhaust duct. The exhaust flow used during the experiments was typically 70 kg/s and is listed among the test results posted to the NIST Fire Calorimetry Database (FCD) website. Side skirts located 6.1 m above the floor were suspended from and surrounded the exhaust hood. Multiple heat flux gauges and plate

thermometers were arranged vertically at designated locations as described in detail in Section 2.3.4.

The trees were ignited using a hexagonal-shaped, natural gas burner at the base of the tree (see Section 2.5.1). The trees were allowed to burn until the flames and smoldering self-extinguished.

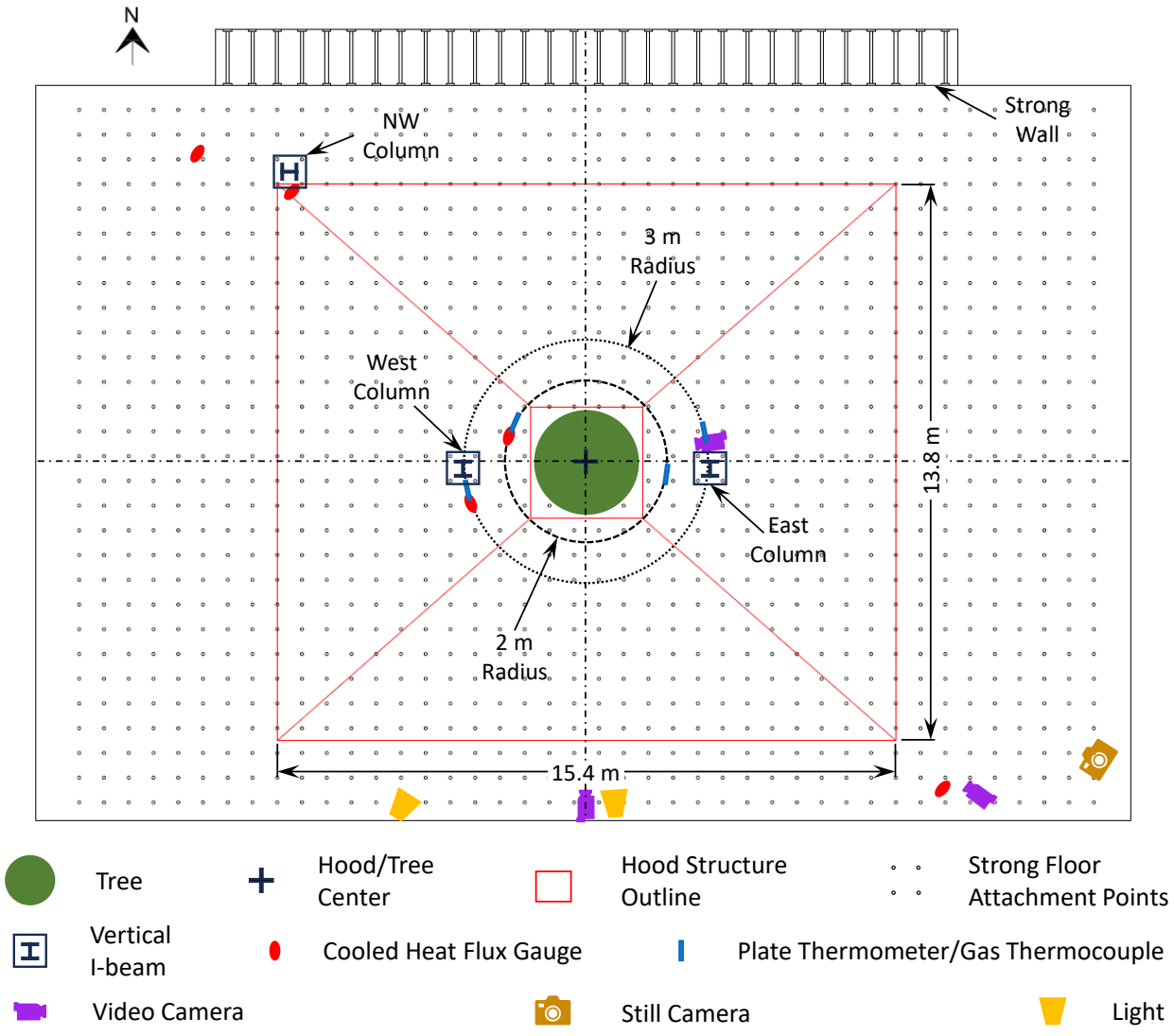

Figure 2. A scale plan view drawing of the area under the 13.8 m × 15.4 m canopy hood showing instrumentation locations.

2.2. Specimens

Table 1 characterizes the gross features of the trees used in this study, including its dimensions, mass, and dry basis moisture content (MC). The experiments were divided into three series focused on the effect of the following on the burning character of the trees:

(1) the effect of tree height for dry trees,

(2) the effect of moisture content for tall trees, and

(3) the reproducibility of the results for dry, tall trees.

For the first series of experiments, three pairs of trees were selected for study based on their height, which was roughly 4 m (Trees 1 and 2), 4.5 m (Trees 3 and 4), and 6 m (Trees 5 and 6). Although there was natural variation among each pair, Table 1 shows each pair also had similar widths and masses. The trees were kept until they were extremely dry and until all had a similar dry-basis moisture content of 8 % to 13 %.

The second experimental series consisted of six trees obtained at the same time but tested in a staggered schedule over 4 weeks when each tree's moisture content reached a target level of 30 % to 55 %. Table 1 shows the similar heights but varying moisture contents for these trees. The third series consisted of six more trees which were allowed to dry to relatively low moisture levels (7 % to 22 %). Table 1 lists their heights and moisture content on the test day.

The trees' heights and widths were measured using two methods: (1) photographic analysis using comparison to the known height and separation distance of the vertical instrumentation columns adjacent to the trees and (2) photogrammetry which is photographs to create three-dimensional (3D) models. Photos of each of the specimens overlaid with their dimensions are listed by test number in Appendix A. The trees were stored indoors under ambient conditions for about 2 months at an average temperature of 25.0 °C ± 1.4 °C and relative humidity between 41 % to 83 % with an average value of 62 % ± 10 %. The moisture content of the trees was monitored daily as described in Section 2.3.2, and the final dry basis moisture content is reported in Table 1.

The tree trunks were secured to the base of the stands, which were positioned about 0.35 m above the floor. The widths listed are the maximum extent rather than an average and were measured only from the south side. The combined expanded uncertainty of the initial (dry) tree masses (corrected for water content) with a 95 % confidence level are listed in Table 1 based on measurement resolution, repeat measurements, calibration with standard weights, and manufacturer information about the weighing system.

Table 1. List of tree height and maximum width determined using photography, the initial tree mass corrected for moisture content (MC), and the measured dry basis MC percentage.

Test	Tree [a]	Height (m)	Width (m)	Initial Dry Mass (kg)	MC (%)
1	1	3.37 ± 0.02	2.35 ± 0.02	14.38± 0.57	7.8 ± 1.9
2	2	3.66 ± 0.02	2.15 ± 0.02	18.47 ± 0.57	8.5 ± 1.9
3	3	4.23 ± 0.03	2.71 ± 0.02	27.67± 0.57	8.6 ± 2.0
4	4	4.08 ± 0.03	2.55 ± 0.02	24.46 ± 0.57	8.4 ± 2.0
5	5	5.77 ± 0.05	2.79 ± 0.02	54.93 ± 0.57	11.0 ± 2.6
6	6	5.81 ± 0.05	3.13 ± 0.02	49.48 ± 0.57	13.0 ± 3.1
7	7	6.28 ± 0.12	2.98 ± 0.02	55.74± 0.57	35.0 ± 2.2
8	8	5.93 ± 0.02	2.78 ± 0.02	43.63± 0.57	42.1 ± 15.6
9	9	5.87 ± 0.03	2.93 ± 0.02	55.22± 0.57	55.1 ± 8.1
10	10	7.44 ± 0.15	3.57 ± 0.02	68.41± 0.57	49.1 ± 25.8
11	11	6.15 ± 0.04	2.84 ± 0.02	41.87± 0.57	29.7 ± 2.4
12	12	6.06 ± 0.02	3.24 ± 0.02	64.57± 0.57	44.5 ± 9.9
13	13	5.94 ± 0.07	3.05 ± 0.02	58.85± 0.57	7.4 ± 3.4
14	14	6.63 ± 0.06	2.63 ± 0.02	65.49± 0.57	14.9 ± 2.1
15	15	5.84 ± 0.02	3.70 ± 0.02	79.99± 0.57	17.2 ± 1.6
16	16	5.60 ± 0.02	2.64 ± 0.02	51.15± 0.57	17.0 ± 3.5
17	17	6.50 ± 0.02	3.32 ± 0.02	87.09± 0.57	21.6 ± 7.8
18	18	6.64 ± 0.02	3.08 ± 0.02	80.49± 0.57	21.2 ± 2.2

a. In this report, the test number and the tree number are taken to be identical.

2.3. Instrumentation

Several measurements were made in this study in addition to calorimetry and items normally reported as part of the FCD (see Section 1), including:

- Moisture content of the trees using a moisture analyzer
- Transient mass loss using a load cell system
- Transient radiative heat flux to targets using cooled heat flux gauges and plate thermometers
- Video camera recordings from several perspectives

The data was sampled at 200 Hz with the averages recorded at 1 Hz for Tests 1 – 10. For Tests 11–18, the data recording frequency was increased to 10 Hz to improve the fidelity of the transient measurements and reduce discretization errors. A description of each of the measurements is given below.

2.3.1. Calorimetry

Information about the calorimeters, including a detailed discussion of the NIST oxygen consumption calorimetry measurement method, measurement uncertainty, and measurement validation has been documented [Bryant and Bundy, 2019]. A fuel consumption calorimetry system (natural gas burners and flow control) used to generate precise amounts of heat release was used to provide a rigorous evaluation of the oxygen consumption calorimetry system and its uncertainty. The expanded (k = 2) combined uncertainty of the calorimetry system was found to range between 5.6 % and 11.3 %, depending on the experimental conditions [Bryant and Bundy, 2019]. In this study, the heat of combustion of Douglas-fir and its uncertainty are taken from the literature as described in Section 3.3 below. The time response of the 20 MW calorimetry system has a time constant of approximately 8 s based on analysis of imposed square-wave changes to the HRR determined from calibration experiments using pulses of a natural gas fire imposed in a near square wave shape for various durations. These results suggest that it can accurately resolve fire events lasting more than 20 s to better than 92 % of the actual peak value [Bryant and Bundy, 2019]. Considering the first six trees, Johnsson et al. [2025] developed a method to correct the time response of the transient heat release rate measurements. Di Cristina et al. [2025] describes further advances in time response correction methodology.

2.3.2. Moisture Content

The moisture content (MC) of the trees was measured just before each test as well as during the drying process to estimate when a tree was near its target MC. It was observed that the needles were not uniform in appearance nor moisture content, with needles towards the branch tips featuring higher moisture content, greener appearance, and more pliability than needles closer to the tree trunk. Some detailed MC measurements of inner and outer needles and stems of Tree 4 near the end of its drying process found that the differences could be very large with outer stems and needles having 20 % and 50 % higher MC, respectively, than inner stems and needles. The details of the distribution appeared to differ from branch to branch. For this reason, the moisture content of the tree was characterized by taking spatially distributed samples and combining them to achieve an average measurement. Nevertheless, because of the large moisture gradients within a tree, the “average” MC of each tree had a relatively large standard deviation. On the day of the experiment, 1 g to 3 g samples of needles and stems were collected from various locations in the tree. The samples, of approximately the same mass, were collected from three or four sides of the tree. They were then combined and saved in a sealed plastic bag until testing. A moisture analyzer was used to measure the wet-basis moisture content. Several

core samples low on the trunk were also taken to compare the moisture content before and after the experiments.

The moisture analyzer was programmed to run at a temperature of 110°C with the criteria to end the analysis defined as a sample mass rate of change of less than 0.02 %/minute. The temperature condition was selected to remove all water while preventing the removal of volatile compounds. The termination criterion was conservative, and tests with a smaller rate of change termination criteria showed no discernable difference for tests using the same sample batch.

The calibration of the moisture analyzer was evaluated and found to be better than 2 % based on comparison experiments using an oven (at the same oven temperatures of 110°C) and a precision scale (Sartorius Balance Model #GW6202) for the same sample foliage batch. Measurements using the analyzer showed a high level of repeatability (better than 2 %) for the same sample batch. The standard deviation increased to 12 % when different sample batches were tested from the same tree using the same collection method, presumably due to natural variation.

The analyzer outputs the moisture content on a wet basis percentage (MC_{wet}). Measurements were then converted to a dry basis percentage using the following equation:

$$MC = 100\, MC_{wet}/(100 - MC_{wet}) \quad (1)$$

Where MC is the mean dry basis moisture content value (MC). Table 1 lists MC for each of the trees along with its combined expanded uncertainty.

2.3.3. Mass Loss

The transient mass loss was determined using an Intercomp (model CW250) system of four load cells. The capacity of each module was 200 kg with a resolution of 0.2 kg. The four load cells were placed under the corners of the rectangular load cell platform upon which the tree stand and the tree itself were placed. Before and after each experiment, the mass of the load cell platform, tree stand and supports, and any other objects on the platform were measured so they could be subtracted from the total mass to obtain the initial and final tree masses.

2.3.4. Heat Flux to Targets

The transient heat flux to targets was measured using water-cooled heat flux gauges and plate thermometers in the near- and far-field. The near-field measurements were designed to follow the measurement locations of Mell et al. [2009].

2.3.4.1. Heat Flux Gauges

Table 2 lists the ten water-cooled, wide view angle (180°), thermopile-type, total heat flux sensors that were directed towards the central axis of each tree. Three cooled gauges were located at a 2 m radial distance from the tree axis on the western side of the tree at 3 heights from the mounting surface of the tree stand (i.e., the base of the tree trunk): 0.2 m, 2.3 m, and 4.5 m. The same arrangement of an additional three cooled gauges was located at a 3 m radial distance, also on the western side of the tree, but arranged so their view of the tree was not blocked by the 2 m radius array. Two more cooled gauges were located at a 10 m radius northwest of the tree at 2.3 m and 6.0 m heights. Finally, two additional cooled gauges were positioned 2.3 m high at 12 m radii, one northwest of the tree (arranged to avoid blockage of the line of sight to the fire by the 10 m gauges) and the other southwest of the tree. The locations of the gauges relative to the tree are shown in Figure 2. The gauges positioned at 12 m could not be much further from the trees to avoid shadowing of flames by the exhaust hood skirts.

Huskeflux model SBG01 and Medtherm 64 Series water-cooled heat flux gauges were used to measure the incident heat flux. The gauges were calibrated using a secondary standard gauge in a well-characterized facility [Pitts, 2006]. The uncertainty of the heat flux gauge calibration procedure is estimated as 4.5 % [Pitts, 2006]. The heat flux background signal, which increased during the burning period as the fire heated the surroundings, was subtracted from the signal. Its uncertainty was estimated as 3 %. The combined (k = 2, expanded) uncertainty for the heat flux measurement is estimated as 11 %.

The locations and heat flux gauge types are listed in Table 2. The heights, Z, listed in the table are relative to the tree stand. The distance from the base of the tree stand to the floor was 35.4 cm. The radius, R, was measured relative to the load cell platform or tree center, and the angle, theta, was measured relative to north which was a line passing through the center and perpendicular to the strong wall shown at the top of Figure 2. The last column in Table 2 provides the data label for each sensor.

Table 2. Water-cooled heat flux gauge locations and descriptions.

Direction Relative to Tree	Distance, R (m)	Height, Z (m)	Theta (°)	Gauge Type	Gauge Range (kW/m²)	Data Label
West	1.99	0.2	272.2	Medtherm	200	W2HF02
West	1.99	2.3	272.2	Medtherm	200	W2HF23
West	1.99	4.5	272.2	Medtherm	200	W2HF45
West	2.99	0.2	253.9	Huskeflux	100	W3HF02
West	2.99	2.3	253.9	Huskeflux	100	W3HF23
West	2.99	4.5	253.9	Huskeflux	100	W3HF45
Northwest	9.98	2.3	312.4	Huskeflux	5	NWHF23
Northwest	9.98	6.0	312.4	Huskeflux	5	NWHF60
Northwest	12.12	2.3	308.4	Huskeflux	5	HFNW
Southeast	11.96	2.3	132.5	Huskeflux	5	HFSE

An estimate of the total radiative energy (TRE_i) was determined from the measurements at the two far-field heat flux gauges by integrating the measured radiative heat flux over the burning period (from ignition to the end of the experiment, t_e) at each of the measurement locations:

$$TRE_i = \int_0^{t_e} 4\pi\, R_i^2\, \dot{q}_i^{"}\; dt \tag{2}$$

where ($\dot{q}_i^{"}$) is the radiative heat flux measured at a distance (R_i) from the fire at the i^{th} gauge. The far-field gauge results may differ due to shadowing created by unburnt portions of the trees, which may be particularly evident early in the experiments for the non-symmetric ignitions. Nevertheless, the average of the measured fluxes can be considered representative of the radiative emission from the fire. For suitably far distances from the fire, the radiative fraction (χ_{rad}) is defined as the ratio of the average total radiated energy emitted to the surroundings ($\overline{TRE_i}$) to the total heat release rate over the entire duration of the fire:

$$\chi_{rad} = \frac{\overline{TRE_i}}{\Delta m\, H_c} \tag{3}$$

where Δm is the total mass loss, that is, the difference between the initial and final dry fuel mass, H_c is the net heat of combustion per unit mass of fuel assuming water as a gaseous product. The value of χ_{rad} represents the radiative fraction over the entire burning period, not just the flaming period.

2.3.4.2. Plate Thermometers

Plate thermometers (PT) are robust sensors that can survive in hostile environments, and they were chosen for this series as additional heat flux measurements primarily due to their low cost

and lack of need for cooling water. The PT design was taken from the literature [Wickstrom, 1994] and then modified for faster response and simpler manufacture as described in detail in Putorti [2015]. The PTs consisted of 0.51 mm diameter (24 AWG) Type-K thermocouple wires welded to the back side of a 100 mm by 100 mm Inconel® 600 plate (the front side faces the heat source). The plate was backed by a 25.4 mm thick insulation (ceramic fiber blanket) layer. Metal strips on the back side of the insulation were used to hold it together with the front plate using screws and washers. A photo of one of the modified PTs is shown in Figure 3. The incident heat flux on a PT can be calculated from a heat balance using the following relation [Putorti, 2015]:

$$q''_{inc} = \sigma \cdot T_{PT}^4 + \frac{(h_{PT} + K_{cond})(T_{PT} - T_\infty)}{\varepsilon_{PT}} + \frac{\rho_{ST} \cdot C_{ST} \cdot \delta \cdot \left(\frac{\Delta T_{PT}}{\Delta t}\right)}{\varepsilon_{PT}} \quad (4)$$

where q_{inc}'' is the incident heat flux, σ is the Stefan-Boltzmann Constant, 5.670×10^{-8} W/(m^2·K^4), T_{PT} is the temperature of the plate (K), h_{PT} is the convective heat transfer coefficient, 10 W/(m^2·K), K_{cond} is the conduction correction factor determined from NIST cone calorimeter data, 4 W/(m^2·K), T_∞ is the ambient temperature (K) as measured by a bare bead thermocouple near the plate thermometer shielded from the radiation, δ is the alloy plate thickness (0.79 mm), and Δt is the data acquisition time step (nominally 1 s). Values specified by the alloy manufacturer were used for the plate emissivity (ε_{PT} = 0.85 at 480°C), the alloy plate density (ρ_{ST} = 8470 kg/m^3), and the plate heat capacity (C_{ST} = 502 J/kg·K at 300°C).

Figure 3. A photo of the front of the 10 cm x 10 cm modified plate thermometer.

At each PT location, the nearby gas temperature was also measured, as required by Equation 4. The gas temperatures were measured with K-type thermocouples fabricated from 0.51 mm diameter (24 AWG) wire. Table 3 lists the locations of the PTs relative to the center of each tree. The trees were positioned under the center of the 13.8 m × 15.4 m canopy hood. The same Z, R, and Theta definitions used for Table 2 pertain to Table 3. Data labels representing the instrumentation are also included.

Table 3. Plate thermometer locations.

Direction Relative to Tree	Radius, R (m)	Height, Z (m)	Theta (°)	Data Label
West	2.00	0.2	276.2	W2PTC02
West	2.00	2.3	276.2	W2PTC23
West	2.00	4.5	276.2	W2PTC45
West	2.95	0.2	256.5	W3PTC02
West	2.95	2.3	256.5	W3PTC23
West	2.95	4.5	256.5	W3PTC45
East	2.04	0.2	100.5	E2PTC02
East	2.04	2.3	100.5	E2PTC23
East	2.04	4.5	100.5	E2PTC45
East	2.99	0.2	80.3	E3PTC02
East	2.99	2.3	80.3	E3PTC23
East	2.99	4.5	80.3	E3PTC45

2.3.5. Yield of Exhaust Products

Bryant and Bundy [2019] describe the gas analysis which is part of the calorimetry system. Gas was extracted from the exhaust stream and the concentration of carbon monoxide (CO) and carbon dioxide (CO_2) were measured using non-dispersive infrared analyzers [Bryant and Bundy 2019].

The particulate matter yield was determined using a laser extinction measurement across the exhaust duct following the methodology of Mulholland et al. [2000]. The smoke mass fraction in the exhaust duct was measured with a Si photodiode detector via laser light extinction at 632 nm. The time dependent light extinction coefficient, *K(t)*, is defined as:

$$K(t) = \frac{1}{D}\ln\left(\frac{I_o}{I(t)}\right) = \sigma_s(t) \cdot M_s(t) \quad (5)$$

where D is the exhaust duct diameter, I_0 is the laser reference intensity (determined over a 60 s period before ignition), and $I(t)$ is the transient attenuated laser intensity during the fire [Mulholland and Croarkin, 2000; Bundy, 2020]. The light extinction coefficient, $K(t)$, is equal to the product of the mass-specific extinction coefficient, σ_s, and the mass concentration of smoke, $M_s(t)$. The total mass of smoke (TS) generated by a fire from ignition ($t=0$) to the end of the experiment (t_f) is calculated as:

$$TS = A \cdot \int_{t=0}^{t_f} \frac{K(t)\, V(t) dt}{\sigma_s(t)} \tag{6}$$

where $V(t)$ is the average exhaust stream speed at the duct measurement location and A is the duct cross-sectional area. Although K does not account for the presence of all species in the aerosol (e.g., gases such as carbon monoxide, low molecular weight hydrocarbons, etc.) [Weise et al., 2024], it is representative of the particulate matter emitted by the fire.

Mulholland and Croarkin [2000] posited that the value of σ_s at 632 nm is nearly universal for post-flame smoke and is equal to 8.7 m^2/g ± 1.1 m^2/g, where the error bounds represent the expanded (k=2) uncertainty (confidence interval of 95 %). Their dataset included wood cribs, oak, and Douglas-fir samples as well as plastics and hydrocarbon pool fires.

Seader and Einhorn [1977] show that σ_s of a smoldering aerosol for a variety of polymeric and cellulosic materials is approximately a factor of 0.58 smaller than their flaming analog. Considering Mulholland's result, this yields σ_s = 5 m^2/g for smoldering materials. The practical measurement challenge is that σ_s for a burning solid changes as a fire transitions from pyrolyzing to flaming and then to smoldering, and possibly reigniting back to flaming. A method to address this complexity is described by Sung et al. [2026]. However, in this report and in the NIST Fire Calorimetry Database (FCD), σ_s is assumed to equal 8.7 m^2/g.

To measure PAH, particulate phase smoke was sampled from a well-mixed position in the calorimeter's exhaust duct following Davis et al. [2025A]. A sampling pump pulled smoke through a 47.0 mm quartz filter at 5 SLPM along with another bypass pump to meet isokinetic sampling conditions. The quartz filters were weighed before and after sampling the effluent in each experiment. They were then conditioned in a desiccant for over 24 hours. Next, the mass of particulate matter (PM) collected on the filter was weighed. PM collected on the quartz filters was further analyzed for targeted Polycyclic Aromatic Hydrocarbons (PAHs). For the PAH analysis, a fourth of the quartz filter was extracted with an accelerated solvent extractor (Thermo Scientific, Dionex ASE 350) using dichloromethane (DCM) [Davis, 2025B]. The cut filters were heated to 150°C, rinsed, then purged, repeating the cycle six times. The extracts were then spiked with NIST SRM 2269 and SRM 2270 and concentrated using a TurboVap LV evaporator (Zymark).

Background filters were similarly analyzed. The concentrated extracts were injected (2 µL) directly into a gas chromatography-mass spectrometer (GC-MS), which was used to analyze 36 PAHs ranging from naphthalene to coronene following the methods described in Davis et al. [2024]. For total PAH mass fraction and yields, the individual PAH molar fractions and yields were normalized to the molecular weight of anthracene and reported as anthracene mass equivalent. The results of this analysis are presented in Appendix F.

2.3.6. Visual Record

Three video cameras (Canon models XA40 and XA60) recorded the fire at 30 frames/s at a 1920 x 1080 pixel resolution. An XA40 and an XA60 both faced north toward the center of the tree with the XA40 recording the tree and the XA60 angled about 45° above the horizontal to record the fire plume and the exhaust duct. The two north-facing cameras were located 8.7 m due south of the center of the tree. Another XA60 camera was aimed from the southeast of the tree positioned about 17.5 m southeast of the tree. This video camera was mounted 3.1 m above the tree stand. A webcam was positioned 0.4 m above the tree stand and 2.9 m from the tree near the west column to allow close observation of the burner to determine ignition quality. The location of the video cameras as well as typical values of their orientation (relative to horizontal) and settings are listed in Table 4 (also see Figure 2).

Table 4. Video camera positions and typical settings.

Model	Location	Angle (deg)	f Stop	Shutter Speed (1/s)
XA30	8.7 m south	0	2.8	1/1200
XA60	8.7 m south	45	4.0	1/1200
XA60	12.5 m southeast	0	2.6 to 4.0	1/1600 to 1/1200

A digital still camera (Canon model 80D) was used to capture views of the experimental setup and trees before, during, and after each test. The camera exposure settings were set for automatic. During the ignition and intense burning period, the camera operator photographed the tree from the southeast direction about 20 m from the tree.

LED lights were positioned at (Z, R) equal to (0.6 m, -8.7 m) and (-4.6 m, -8.7 m), where Z is the distance from the floor and R is the distance from the duct/tree central axis (see Figure 2). The cameras and data acquisition results were synchronized to better than 2 s. The locations of the lights and cameras relative to the tree and other instrumentation are shown in Figure 2.

2.3.7. Photogrammetric Characterization

The tree geometry was characterized using photogrammetry, which enabled 3-dimensional (3D) reconstruction of the tree crown [Linder, 2003]. This is particularly relevant for detailed fire modeling efforts where individual linear measurements (e.g. height, width) may not be sufficient to characterize the spatial distribution of biomass. The measurements were conducted using a tablet computer equipped with a 12 MP camera and the Scaniverse [2024] photogrammetry software (app). At least three orbits of each tree were completed, orienting the camera at different heights and angles to capture sufficient perspectives for photogrammetric reconstruction. For the tallest trees, a scissor lift was used to include an orbit at sufficient elevation to adequately view the treetop.

The output of the photogrammetric scan was in the form of a 3D point cloud which was manually cropped to contain only the tree as shown in Figure 4. These points represent only a subset of individual branch and needle locations, and the density was not sufficient to create a detailed wireframe mesh. Instead, they were used to create a voxelized representation where voxels on a predefined rectilinear mesh are filled in locations that contain points of the cloud (Figure 4). A 5 cm voxel size was selected to be commensurate with possible mesh size for a fire model while also considering the uncertainty associated with the point cloud. Further exploration of the effect of voxel size is provided in Appendix E. Similar voxelization methods based on lidar-derived point clouds have been employed to provide vegetation geometry for fire modeling [Marcozzi et al., 2023].

Because the photogrammetry cannot penetrate the dense crown, there are few points registered in the internal crown space. To obtain a total crown volume, an ellipse is fit to the point cloud contained in each horizontal slice of voxels using total least squares [Halir and Flusser, 1998]. Values within the ellipse are filled, as well as any remaining voxels which are completely surrounded by vegetation containing voxels. An example of this process is shown in Figure 4.

In addition to computing volume, this method was used to determine tree height (difference between maximum and minimum voxel locations in the z-direction). An ellipse with the same normalized second central moment as the projection of the voxelized crown geometry in the z-direction was also used to determine a major and minor crown radius. An example is shown in Figure 4. Results of the tree geometry characterization are given in Table 5 and Appendix E.

Figure 5 compares the maximum widths and heights determined by photogrammetry versus photography, which shows fairly good agreement among the photogrammetry and photo-based methods.

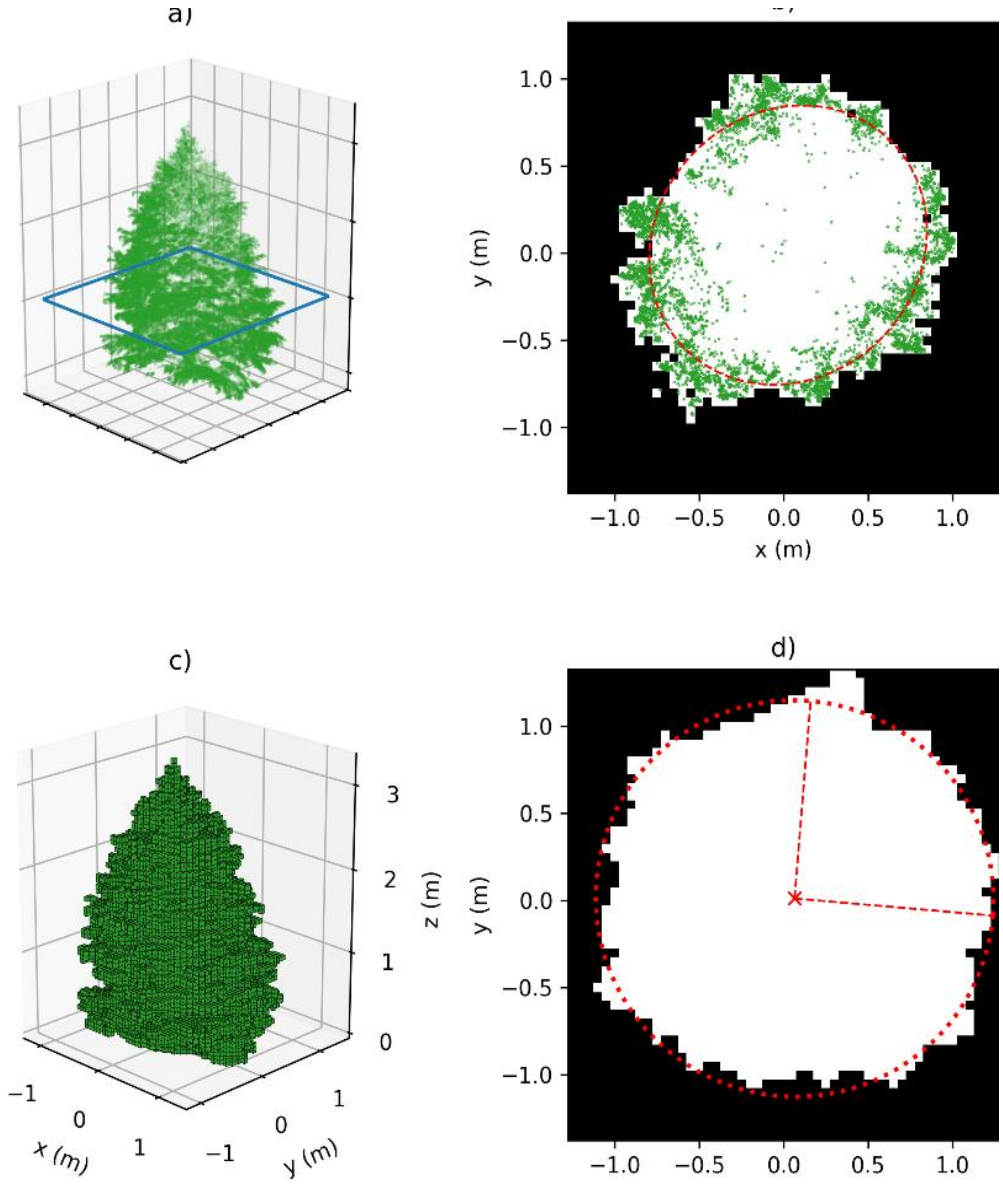

Figure 4. Example of process for photogrammetric characterization of Tree 1. (a) Raw scan data in the form of a 3-dimensional point cloud. (b) A horizontal slice (blue plane in (a)) of voxels containing points. Voxels inside an ellipse fit to the point cloud, using total least squares, are also filled. (c) Voxelized representation of the whole crown volume. (d) Major and minor crown radius were determined by fitting an ellipse with the same normalized second central moment as the projection of the voxelized crown geometry in the z-direction.

Table 5. Tree dimensions determined from photogrammetry using a 5 cm voxel size. Uncertainties are reported as the combined expanded (k = 2) uncertainty, representing a 95 % confidence interval.

Tree	Height (m)	Major Crown Diameter (m)	Minor Crown Diameter (m)	Crown Volume (m^3)	Dry Fine Fuel Bulk Density (kg/m^3) [a]
1	3.30 ± 0.11	2.36 ± 0.11	2.27 ± 0.11	5.36 ± 0.62	1.21 ± 0.19
2	3.60 ± 0.11	2.16 ± 0.11	2.06 ± 0.11	4.65 ± 0.60	1.79 ± 0.30
3	4.20 ± 0.11	2.83 ± 0.11	2.56 ± 0.11	8.08 ± 0.88	1.54 ± 0.23
4	3.95 ± 0.11	2.37 ± 0.11	2.11 ± 0.11	5.69 ± 0.68	1.93 ± 0.30
5	5.85 ± 0.11	3.03 ± 0.11	2.78 ± 0.11	14.73 ± 1.32	1.68 ± 0.23
6	5.70 ± 0.11	2.88 ± 0.11	2.77 ± 0.11	12.90 ± 1.28	1.73 ± 0.24
7	6.20 ± 0.11	3.03 ± 0.11	2.78 ± 0.11	14.91 ± 1.40	1.68 ± 0.23
8	5.95 ± 0.11	2.59 ± 0.11	2.57 ± 0.11	11.07 ± 1.24	1.77 ± 0.27
9	5.85 ± 0.11	3.03 ± 0.11	2.90 ± 0.11	15.84 ± 1.38	1.57 ± 0.21
10	7.45 ± 0.11	3.26 ± 0.11	3.07 ± 0.11	19.54 ± 1.84	1.58 ± 0.22
11	6.00 ± 0.11	2.60 ± 0.11	2.56 ± 0.11	10.98 ± 1.24	1.72 ± 0.26
12	5.30 ± 0.11	2.67 ± 0.11	2.50 ± 0.11	11.56 ± 1.08	2.51 ± 0.34
13	5.60 ± 0.11	2.85 ± 0.11	2.67 ± 0.11	11.11 ± 1.21	2.38 ± 0.35
14	6.70 ± 0.11	2.83 ± 0.11	2.60 ± 0.11	11.99 ± 1.40	2.46 ± 0.38
15	5.80 ± 0.11	3.43 ± 0.11	3.30 ± 0.11	19.11 ± 1.56	1.88 ± 0.24
16	5.65 ± 0.11	2.60 ± 0.11	2.53 ± 0.11	11.32 ± 1.15	2.03 ± 0.29
17	5.95 ± 0.11	3.01 ± 0.11	2.91 ± 0.11	15.49 ± 1.40	2.53 ± 0.34
18	6.40 ± 0.11	2.90 ± 0.11	2.76 ± 0.11	16.62 ± 1.43	2.18 ± 0.29

a. Dry fine fuel mass is an approximation. Using data from Mell et al. [2009], it's estimated that 45 % of the dry initial tree mass was fine fuel, that is, foliage and branches with diameters of 10 mm or less.

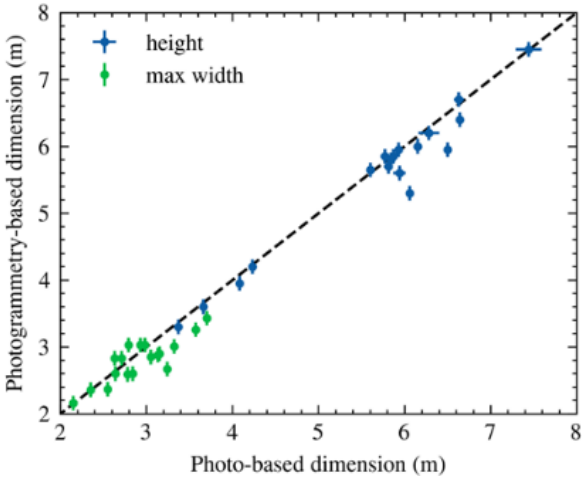

Figure 5. Comparison of the maximum widths and heights determined by photogrammetry versus photography.

2.4. Early Test Preparation

The Douglas-fir trees were delivered bound in twine. Before unwrapping each tree, they were lifted upright and mounted on a plywood stand (described in Section 2.4.1). The trunk of the tree was lowered into the trunk box on the center of the stand and the twine removed. Four wooden supports were attached from the stand to the tree to provide bracing.

Before testing, a method of ignition was devised. A hexagonal (roughly circular), non-premixed natural gas line burner was assembled and tested with various igniter methods. Burner testing was performed before the first tree experiment and in between subsequent experiments to improve its performance.

Prior to each experiment, photographs of the tree were taken from various directions and photogrammetry was conducted (see Section 2.3.7). Just before the experiments, samples of branch tips were collected for moisture content measurement.

2.4.1. Tree Stands

The trees were mounted on tree stands which in turn were placed on the load cell platform. The load cell platform consisted of a 1.83 m by 1.22 m cement board (1.3 cm thickness) on top of a plywood sheet of the same area (1.83 cm thickness). The two layered boards rested on wooden support beams (8.9 cm square cross-section) which spanned each pair of load cell modules on the north and south sides of the setup.

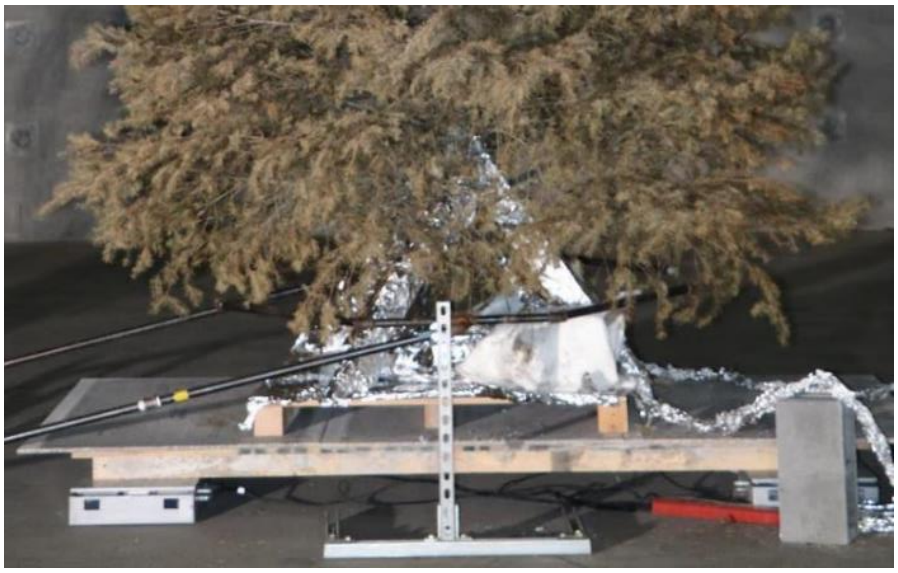

Figure 6. A photograph of the tree stand on the load cell platform.

Each tree stand consisted of two (nominal) 4 in × 4 in (8.9 cm) square cross section boards and a (nominal) 2 in × 4 in (3.8 cm × 8.9 cm) cross section board supporting a sheet of (nominal) ¾ in (1.83 cm) plywood. A box to hold the tree trunk was fabricated from 2 × 4 boards attached to the center of the plywood sheet base (see Figure 7). Four 2 × 4 boards were used to support the tree vertically and were attached at angles to the stand base and the tree. The lengths and angles of the support boards were adjusted for different tree heights. Aluminum foil was used to cover accessible portions of the wood 2 × 4s and base prior to each burn.

Figure 7. A photograph of the plywood tree platform prior to mounting the tree.

2.5. Ignition Method

The trees were ignited with a hexagonally shaped natural-gas burner. The burner was ignited with a remote spark ignition system, the design of which evolved during the course of the experimental series. The burner and spark igniters are described in the following sections.

2.5.1. Burner Description

The ignition burner stages consisted of two three-sectioned halves made of a series of 33 mm (1.32 in) OD pipe sections leading from the natural gas supply line to two main 27 mm (1.05 in) OD pipe sections. Holes 0.32 mm (1/8 in) in diameter were drilled every 2.5 cm in the upper surfaces of the pipe sections and elbow connectors to allow fuel gas to exit upwards and create numerous small flames along its length. The two burner halves and their supply pipes were connected at the center sections and separately supported by metal stands. The burner was disassembled to place the tree on the load cell and then reassembled with the two halves forming an irregular hexagon.

The burner was positioned below the bottom tree branches, such that it did not touch any of them, while at the same time, the 10 cm to 20 cm burner flames would impinge on most of the lowest branches. The burner design was changed as needed for the larger trees to ensure that the igniter flames were positioned under the lowest branches. A photograph of the smallest version of the burner is shown in Figure 8. Figure 9 shows the same early version of the burner with the flames ignited. For larger tree heights and widths, the burner had to be widened with sections of pipe added to the supply "T" at the left of Figure 8. The two halves then had gaps between them. For the largest trees, when the gaps became too wide and burner flames were not present to ignite the branches above the gaps, additional pipe sections with holes were added to the burner. Photos of the burner arrangement under each of the trees is shown in Appendix A.

Figure 8. The first version of the burner used for the shortest trees.

Figure 9. An early version of the burner with flames.

2.5.2. Ignition Description

A set of four spark igniters was used to ignite the natural gas burner. The igniter system consisted of an activation switch, a power supply, low-voltage extension wire, coil packs, and high-voltage extension wire. The power supply provided 5 V with a 10 A capacity. The low voltage extension wire carried the current from the power supply and switch about 12 m to the burner. At the burner, the low voltage wires were connected to the four 2 A coils located near the centers of four burner sections. At each coil, high voltage wires were connected with the ends placed above the burner holes with a gap space on the order of 5 mm. The coil packs and high- and low-voltage wires were protected from flame radiation by a ceramic fiber blanket and aluminum foil where appropriate.

2.6. Test Procedure

Shortly before each tree experiment, the burner igniters were tested. For the initial tests, the igniters were tested without the tree in place. It was found that the process of putting the tree in place and repositioning the burner and spark igniters diminished their performance. Thus, in later experiments, the spark igniters were tested with the tree in place, but without any gas flow and with the igniters shielded to prevent inadvertent ignition of the tree branches by the sparks. Natural gas was run through the burner lines for several seconds to charge the lines and mitigate non-symmetric ignition. The gas flow was opened 1 s prior to turning on the spark igniters. The gas flow was maintained for a specified time before the manual valve was shut. The gas flow was non-uniform due to a pressure pulse when the manual gas valve was opened to the atmosphere.[2] The measurement of the volume flow of natural gas was made upstream of the manual shutoff valve by a positive displacement flow meter (Instromet IRM-A 15M-125) equipped with a frequency pulse counter (Pepper & Fuchs KD2- UFC-Ex1.D), 2 thermistor temperature probes, and 2 pressure transducers [Bryant and Bundy, 2019]. The natural gas composition of the igniter flames was measured by a micro gas chromatograph (Inficon Fusion) to determine its energy content [Bryant and Bundy, 2019]. Table 6 provides a summary of the natural gas burner igniter energy. The table lists the manual natural gas valve opening duration, the total heat supplied by the gas burner, and the igniter's total heat release (Gas Burner THR) as a percentage of the total heat release of the fire (THR). The total energy released by the gas burner was 2.5 MJ on- average

2. The transient HRR estimate of the igniter gas flow is seen in the plot overlay of the test videos available on the FCD.

for Tests 1 to 6 and 7.1 MJ for Tests 7 to 18, representing about 1.3 % of the total fire heat release (see additional discussion in Section 3.1 below).

Table 6. The nominal igniter (gas burner) duration, the total burner heat released, and the total heat released as a percentage of the fire THR. Uncertainties are reported as the combined expanded (k = 2) uncertainty, representing a 95 % confidence interval.

Test	Gas Flow Duration (s)	Gas Burner THR (MJ)	Gas Burner THR/THR (%)
1	15	2.62 ± 0.04	1.1 ± 0.1
2	11	2.18 ± 0.03	1.4 ± 0.1
3	15	2.62 ± 0.04	1.7 ± 0.1
4	11	2.18 ± 0.03	1.0 ± 0.1
5	12	2.61 ± 0.04	0.5 ± 0.1
6	11	2.50 ± 0.04	0.4 ± 0.1
7	30	5.70 ± 0.08	1.3 ± 0.03
8	32	6.74 ± 0.10	2.1 ± 0.03
9	35	6.99 ± 0.10	1.4 ± 0.2
10	39	6.82 ± 0.10	1.3 ± 0.1
11	36	7.30 ± 0.11	1.8 ± 0.2
12	38	7.25 ± 0.11	1.2 ± 0.1
13	37	6.99 ± 0.10	1.5 ± 0.1
14	41	7.70 ± 0.11	1.4 ± 0.1
15	36	7.45 ± 0.11	0.8 ± 0.1
16	38	7.62 ± 0.11	1.7 ± 0.1
17	38	7.53 ± 0.11	1.1 ± 0.1
18	36	7.25 ± 0.11	1.0 ± 0.1

2.7. Post-Test Procedure

At the end of each experiment, several measurements were made prior to removing the burned tree. Photographs of the tree were taken from several sides. A photogrammetry record was created of the burned tree, which was used to render a three-dimensional model. Any branches or debris that was separated from the tree during burning were placed on the stand to obtain a final mass of the tree that was not consumed in the fire.

The trunk diameter as a function of height above the tree base was determined for Tests 1 to 6 and is presented in Johnsson et al. [2025]. For a number of trees, the diameters of the burned and unburned branch tips and their height above the tree base were measured using calipers and are reported in Section 3.6 below.

3. Results and Discussion

3.1. Summary of Experiments

The trees burned remarkably fast. The period between ignition and peak fire size was on the order of 7 s to 11 s (except Tree 8, which experienced a completely asymmetric ignition event). After the peak HRR, the fire size diminished over about the next 10 s. Once the flames self-extinguished, the tree was mostly in a glowing mode with typically just a few lower branches flaming for less than a minute. Relatively little mass loss occurred during this glowing-smoldering last phase of burning.

Figure 10 shows the evolution of flame spread from ignition (t = 0 s) to 60 s after ignition during the burning of Tree 6. The time from ignition to peak fire heat release rate for Tree 6 was about 8 s. The tree fire then diminished over the next 30 s to 40 s. After another 30 s to 60 s, most of the flames self-extinguished and the tree was mostly in a glowing mode with only a few lower branches flaming for about a minute. Portions of the tree remnants smoldered for about another minute until they completely self-extinguished. Video recordings of the tree fire experiments are available at the NIST Fire Calorimetry Database (FCD).

The time it took for flames to spread and travel from the base of the tree to its top, near the top of the canopy hood during Test 6 was on the order of 8 s. This represents a flame spread rate on the order of 2 m/s, which is similar to the laminar flame speed of a stoichiometric premixed hydrogen-air flame at ambient conditions [Glassman et al., 2014]. This unusually fast flame spread during the experiments is attributed to the vertical tree structure and to its needles which were widely distributed and thermally-thin fuel elements. Flame spread for the very dry trees (MC<10 %), such as Tree 6, was noticeably faster than trees with larger moisture content.

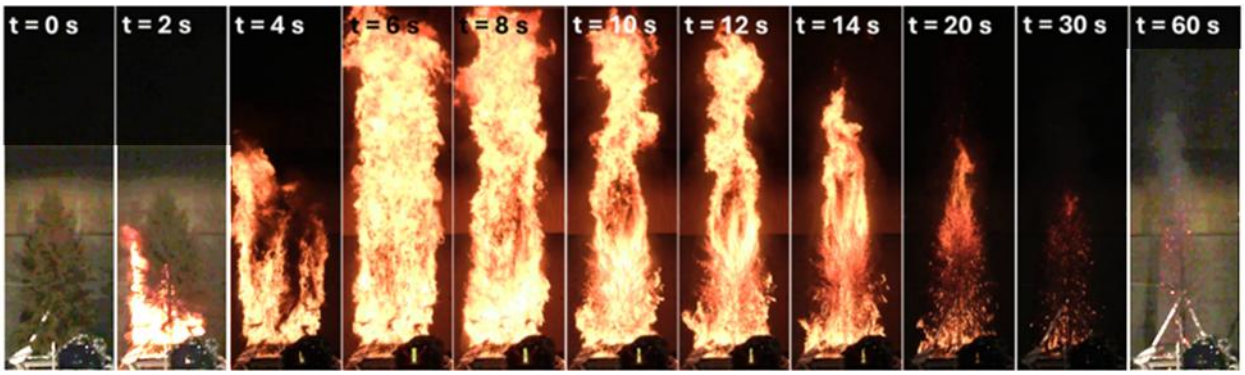

Figure 10. Flame spread evolution during testing of Tree 6 from ignition (t = 0 s) to 60 s after ignition. The images at 0 s, 2 s, and 60 s have been brightened to enhance perception of the tree. The camera was positioned 8.7 m from the tree and angled upwards approximately 45° to capture the entire flame plume.

The character of the burner ignition (symmetric versus non-symmetric) and the degree of the igniter flames' interaction with the lowest and outer branches strongly influenced the fire spread behavior. Brief descriptions of the ignition character, burning times, and symmetry of the fires are provided in Table 7.

Table 7. Summary of experimental observations, including ignition and fire spread.

Test	Ignition Character	Fire Spread Description
1	Non-symmetric.	Burner failed to ignite several lower branches on the east side and a few on the northwest and southwest. Significant amount of protracted burning and a significant amount of unburned mass.
2	Nearly symmetric, but south half of burner ignited 2 s late.	Despite uneven ignition, most of tree still ignited. A few lower branches on southwest and west sides did not burn.
3	Non-symmetric; burner too far inward to ignite outer branches.	Bottom third of outer branches on the east side did not burn. Bottom 2/3 of outer branches on the west side did not burn.
4	Nearly symmetric.	A few low branches on the west and very low branches on the north and east sides didn't ignite. Most of tree burned.
5	Non-symmetric. South half of burner did not ignite.	Fire spread more slowly and downward on the south side. Eventually, most of tree burned except a few lower, outer branches on the south, east, and north sides.
6	Nearly symmetric, but south half of burner ignited 2 s late.	Nearly all branches consumed. Only one small lower outer branch on the south side remained.
7	Non-symmetric. North half of burner did not ignite.	Most of south branches consumed. Lower north outer branches were not ignited by the burner, and downward fire spread did not consume them.
8	Non-symmetric. Ignition started at the east end of the north half of the burner and spread counterclockwise. North half of burner was fully ignited within 2 s, but south half of burner needed another 6 s.	Fire spread counterclockwise around the tree following the burner ignition. Last area of the tree consumed was the southeast corner, but fire gradually spread over the whole tree and most branches were burned.
9	Nearly-symmetric burner ignition – complete within 1 s.	Lower level of tree ignited nearly simultaneously, and the tree burned uniformly. Only a few outer ends of lower branches were not consumed.
10	Nearly-symmetric burner ignition – complete within 1 s.	Lower level of tree ignited nearly simultaneously with the southeast corner igniting last, and the tree burned uniformly. Many outer ends of lower branches around the periphery were not consumed with the most unburned foliage remaining on the east side.
11	Nearly-symmetric burner ignition – fire spread from east to west both ways around burner within 2 s.	Following the burner ignition, east end of the tree's lower level ignited just before the west end. The burning halves converged, and the tree burned uniformly. Only a few outer ends of lower branches were not consumed.

Test	Ignition Character	Fire Spread Description
12	Non-symmetric. Ignition started at southeast section of south burner half and spread both ways to cover south burner half within 1 s. North half ignited at west end from south burner flames and spread east within ~3 s more. South half of burner was fully ignited within 1 s, but north half of burner needed another 3 s.	The north half of the tree lagged the south in becoming involved, but eventually most outer branches were consumed by downward fire spread. Only a few outer ends of the lower branches were not consumed. The extent of burning was fairly symmetric by the end of test.
13	Whole burner ignited within 1 s for a nearly symmetric ignition.	The lower level of tree ignited nearly simultaneously, and the tree burned uniformly. Only a few outer ends of lower branches, mainly on the south side, were not consumed.
14	Whole burner ignited within 1.5 s for a nearly symmetric ignition.	The tree burned symmetrically – even very low branches below the level of the burner ignited via downward fire spread and radiation to consume all.
15	Whole burner ignited within 1 s for a nearly symmetric ignition.	Because of the width of the tree, areas of south and west lower outer branches were not initially involved but were eventually ignited by downward fire spread and mostly consumed.
16	Whole burner ignited within 1 s for a nearly symmetric ignition.	Generally, a symmetric burn, but some lower outer branches on the southwest side that protruded far out from the burner were not initially involved and remained unburned.
17	Somewhat-symmetric burner ignition – spread from starting points south and northwest and went around the burner within 2 s.	Generally, a symmetric burn, but some lower outer branches on the south and east sides that protruded far out from the burner were not initially involved and remained unburned.
18	Nearly-symmetric burner ignition – fire spread from northwest both ways around burner within 1.5 s.	The tree burned symmetrically with even very low branches below the level of the burner ignited via downward fire spread and radiation to consume all.

3.2. Mass Loss

The post-fire residual tree mass was mainly the tree trunk along with sections of unburned branches. A number of tree trunks were sampled just before and just after the fire tests near the base of the trunk using a 3/8” (9.5 mm) diameter hole saw. The samples were then measured using the moisture analyzer. On average, the moisture content of the charred trunks was measured as 21.4 % ± 2.9 % after the tests, which is about a factor of 1.03 lower than before the tests. This represents an insignificant difference when the uncertainty of the measurements is considered. For this reason, the moisture content of the residual mass is assumed to be unchanged from its pre-test value.

The dry basis fuel mass loss (Δm) was estimated by subtracting the specimen’s water mass from the total mass loss measured using the load cell ($\Delta m_{measured}$), assuming the initial water remains

in the residual mass of the post-fire tree:

$$\Delta m = \Delta m_{measured} \times \left(1 - \frac{MC}{1+MC}\right) \quad (7)$$

where MC is the dry-based fractional moisture content of the trees' needles and stems measured just before the fire test as listed in Table 1. The value of $\Delta m_{measured}$ was calculated as (m_e - m_i), where m_e and m_i are the final and initial load cell masses during the fire test, respectively. Measurements of the trunk moisture content after the experiment are consistent with the assumption that MC is unchanged by the fire.

3.3. Calorimetry

The heat of combustion on a per-oxygen basis of 13.23 kJ/g ± 0.66 kJ/g has been suggested as applicable for cellulosic materials with a range of stoichiometric oxygen-to-fuel mass ratios, ranging from pure cellulose to various chars [Dietenberger, 2002; Dietenberger, 2021].

The value of the net heat of combustion per unit fuel mass (H_c) was calculated from literature values for the gross heat of combustion (which is typically provided by a bomb calorimeter following, for example, [ASTM D5865, 2019]). The gross heat of combustion is then converted to a net value using the formula:

$$H_c = H_{c,gross} - 21.96\, h \quad (8)$$

where h is the mass fraction of hydrogen in the dry fuel, and the correction assumes that water formed by combustion remains as a vapor. The composition of 35 different vegetation samples from four references was evaluated with the average hydrogen mass fraction found to be 6.1 % with a relative standard deviation of 12 % [Simeoni et al., 2011; Safdari et al., 2018; Leroy et al., 2009; Susott et al., 1975]. The net heat of combustion for Douglas-fir was then determined to be 21 kJ/g [Susott et al. 1982]. Although the gross heat of combustion is often not reported with an uncertainty, the standard deviation of 6 values reported for Douglas-fir fires yielded 3 %, which is a relatively narrow value [Hurley, 2016; Parker and Levan, 1989; Susott, 1982].

Table 8 presents a summary of the experimental results organized by test number, including the total fuel mass loss corrected for water (Δm), the residual mass percentage, the test duration, peak HRR, time to peak HRR, the total heat released (THR), and the net heat of combustion ($H_{c,net}$) where $H_{c,net}$ = THR/ Δm. THR is the total heat release rate measured via oxygen consumption calorimetry integrated over the entire test duration. The residual mass ratio (m_e / m_i) is the mass of the burnt specimen at the end of the test divided by the specimen's initial mass.

The results for the three groups of trees (Tests 1 – 6, 7 – 12, and 13 – 18) can be examined by considering the magnitude of the total heat released by the fires (THR), the peak HRRs, and the calculated net heats of combustion, which are listed in Table 8. The first parameter quantifies the total enthalpy released by the fire. The second parameter is an indicator of fire hazard as the peak HRR of a single item burning strongly influences the rate of fire spread and growth [Babrauskas 1992]. The third parameter, $H_{c,net}$, is a measure of the amount of energy release per unit mass burned and is a useful way to compare the burning character of different specimen types. See Di Cristina et al. [2025] for a discussion on methods to correct the peak HRR for the time response of the calorimetry system.

Table 8. Summary of test results including the fuel mass loss corrected for water content (Δm) and post-fire residual mass percentage. The peak HRR, time to peak HRR, total heat release (THR) measured by oxygen consumption calorimetry, and effective heat of combustion ($H_{c,net}$) are also listed. Uncertainties are reported as the combined expanded (k = 2) uncertainty, representing a 95 % confidence interval.

Test	Δm [kg]	Residual Mass [%]	Peak HRR [MW]	Time to Peak HRR [s]	THR [MJ]	$H_{c,net}$ [MJ/kg]
1	9.4 ± 0.5	35	7.5 ± 0.8	8 ± 4	169 ± 19	18.0 ± 2.3
2	7.8 ± 0.4	58	12.5 ± 1.3	7 ± 4	160 ± 18	20.6 ± 2.6
3	8.2 ± 0.5	71	9.0 ± 1.0	9 ± 4	154 ± 17	18.8 ± 2.4
4	11.3 ± 0.5	54	13.7 ± 1.4	7 ± 4	218 ± 25	19.3 ± 2.4
5	28.3 ± 1.4	49	36.6 ± 3.9	10 ± 4	594 ± 66	21.0 ± 2.5
6	24.4 ± 1.4	51	42.1 ± 4.5	8 ± 4	622 ± 67	25.5 ± 3.1
7	21.4 ± 0.8	62	26.2 ± 2.8	9 ± 4	455 ± 50	21.2 ± 2.5
8	16.5 ± 3.6	62	14.5 ± 1.6	18 ± 4	324 ± 36	19.7 ± 4.9
9	21.2 ± 2.2	62	27.2 ± 2.9	11 ± 4	495 ± 55	23.3 ± 3.6
10	21.4 ± 7.4	69	35.0 ± 3.8	10 ± 4	513 ± 57	23.9 ± 8.7
11	18.0 ± 0.7	57	26.3 ± 2.8	9 ± 4	406 ± 45	22.6 ± 2.7
12	25.8 ± 3.6	60	35.5 ± 3.7	10 ± 4	616 ± 68	23.9 ± 4.2
13	23.4 ± 1.5	60	29.0 ± 3.1	9 ± 4	481 ± 54	20.6 ± 2.7
14	28.2 ± 1.1	57	30.1 ± 3.2	10 ± 4	550 ± 61	19.5 ± 2.3
15	46.2 ± 1.3	42	39.9 ± 4.3	10 ± 4	885 ± 99	19.2 ± 2.2
16	21.4 ± 1.3	58	28.4 ± 3.0	10 ± 4	445 ± 50	20.8 ± 2.7
17	34.7 ± 4.5	60	38.5 ± 4.1	10 ± 4	701 ± 79	20.2 ± 3.5
18	35.3 ± 1.3	56	40.7 ± 4.3	9 ± 4	753 ± 84	21.4 ± 2.5

The first group of trees is extensively discussed in Johnsson et al. [2025]. The trees were all very dry. They were paired roughly by their height: the shortest were Trees 1 and 2, followed by Trees 3 and 4, and the largest were Trees 5 and 6. The THR roughly followed these trends as might be expected, although the peaks did not, which is attributed to asymmetric ignitions of Trees 1, 3, and 5. Asymmetric ignition could be expected during an actual wildfire.

The second group of trees (Trees 7 – 12) were selected to help evaluate moisture content effects. These trees had moisture content varying from 30 % to 55 %, which significantly increased the range of this parameter.

The third group of trees (Trees 13 – 18) were selected to evaluate experimental repeatability for trees with low (but not bone dry) moisture content. The trees had roughly similar moisture content (15 % to 22 %) with the exception of Tree 13 which had a MC of 7 %. The overall dimensions of the trees were roughly similar (5.8 m to 6.6 m tall). Although the trees were dried to similar MC values and were of similar height, their pre-test masses were significantly different, varying from 59 kg to 106 kg and unsurprisingly, there were large differences in the THR as seen in Table 8. Yet there was little variance in the $H_{c,net}$ which was on-average equal to 20.3 MJ/kg ± 0.4 MJ/kg (or ± 2 %). This narrow variance suggests that the energy release for this group of trees was similar and that there was little difference in the overall combustion character of the fires. A narrow variance of $H_{c,net}$ was also true for the first set of trees (Trees 1 – 6) for which $H_{c,net}$ was equal to 20.6 MJ/kg ± 0.3 MJ/kg (or ± 2 %). This was not true of the second set of tree (with their large variance in MC) for which $H_{c,net}$ was equal to 22.5 MJ/kg ± 2.3 MJ/kg (or ± 10 %). The larger energy release per mass of fuel and its significantly larger variance suggests that understanding the fires burning these moist trees is more complex than the first and third tree groups. The relatively larger variance in $H_{c,net}$ may be due to uncertainty associated with MC, which was proportionately larger for the moist trees. Larger uncertainty in MC, can lead to larger uncertainty in the mass burned, which impacts the estimate of the amount of fuel mass burned and thereby $H_{c,net}$.

Figures showing the transient heat release rate (HRR) for each test are compiled in Appendix B. Additionally, the HRR was determined using the measured mass loss rate (MLR) such that:

$$HRR_{MLR} = \dot{m}\, H_c \tag{9}$$

where $\dot{m}$ is the dry fuel mass loss rate (corrected for moisture content as listed in Table 1), and H_c is the net heat of combustion of Douglas-fir taken as 21 kJ/g following Susott [1982] (discussed in Section 3.3 above). Figure 11 shows general agreement between the total heat released (THR) determined by integrating the HRR_{MLR} in Equation 9 over the duration of the fire as compared to

the THR determined by calorimetry and listed in Table 8.[3] Details of the calorimetry system and characterization of its time response are found in Bryant and Bundy [2019]. A method to correct the HRR profile for the time response of the calorimetry system using the load cell and heat flux measurements is discussed in **Error! Reference source not found.** of this report, based on the method described by Johnsson et al. [2025] and Di Cristina et al. [2025].

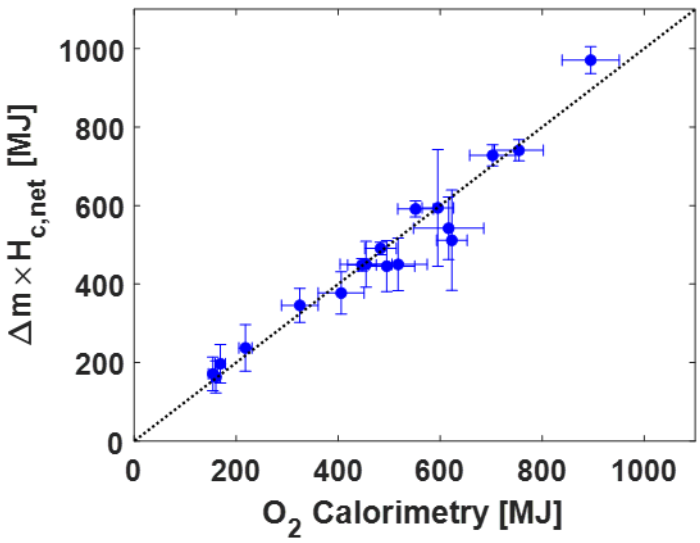

Figure 11. The ideal heat release determined from the total mass loss (corrected for water) versus the total heat released (THR) determined using O2 consumption calorimetry. The dotted line represents parity, and the error bars represent the expanded combined uncertainties representing a 95 % confidence interval.

Figure 12 shows the net heat of combustion (see Table 8) as a function of the tree moisture content (Table 1). The average value of $H_{c,net}$ is equal to 21.1 MJ/kg ± 2.0 MJ/kg, which is consistent with Susott's [1982] value of 21 MJ/kg for Douglas fir, which has an estimated relative standard uncertainty of 3 % or 0.6 MJ/kg. The measured values of $H_{c,net}$ show a slight increase with MC, albeit small and within the uncertainty bounds.

3. Due to electrical signal interference from the spark igniters, the voltage signal from the load cell was unreliable for a portion of the trees. When the sparkers were turned on, a non-physical increase in the mass was observed, as the tree burned, the signal exhibited large fluctuations and instabilities. For reasons of data quality, the results of the time-resolved heat release rates derived from the mass loss rates and the transient mass profiles for Trees 8 to 12 are omitted from Appendices B and C, respectively.

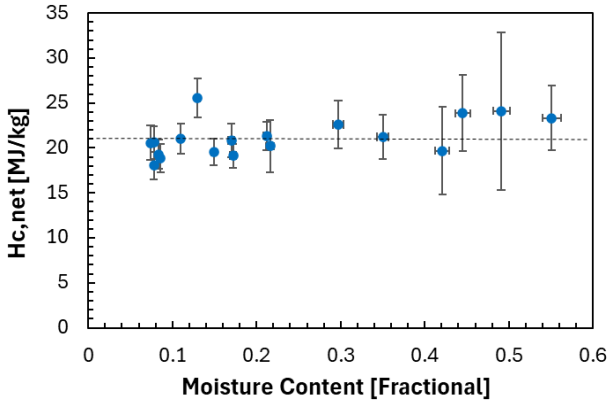

Figure 12. The measured net heat of combustion as a function of the (fractional) dry moisture content. The error bars represent the combined expanded (k=2) uncertainty. The dotted line represents the average Hc,net for all the data in the plot, which agrees with the value determined by Susott [1982].

A multiple linear regression was conducted to determine the influence of MC, the initial tree mass, tree height, crown volume, and χ_{rad} on the measured THR and peak HRR. For both of these dependent parameters, the calculated *Significance F* value was less than 10^{-8} with extremely strong statistical significance associated with the crown volume (*P-value* < 10^{-4}), highly strong statistical significance associated with MC (*P-value < 0.003*), and a statistically significant relationship associated with the tree height (*P-value < 0.03*).

Figure 13 shows the peak HRR and the THR a function of tree crown volume. As the crown volume increased, the peak HRR and the THR increased. The results show that the more voluminous the tree, the larger the fire, which is not surprising. For the range of Douglas-fir trees tested in this study, tree volume appears to be a good predictor of the total energy release by a fire. Investigating cypress tree crown fires, Guo [2025] concluded that flame height and mass loss rate increased with increasing crown height. It would be useful to test this relationship on various types of trees and shrubs.

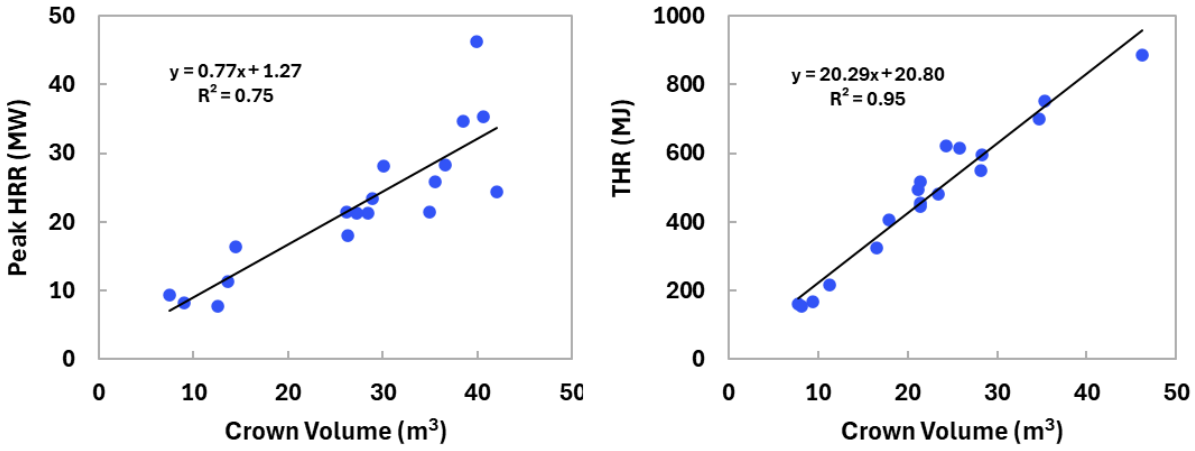

Figure 13. The peak HRR and the THR as a function of tree height. Best fits to a power function are also shown. The average combined expanded uncertainties (k=2) of the peak and total HRRs are 8 %.

Unsurprisingly, a regression analysis showed that the peak HRR had an extremely strong statistical relationship with the THR (and vice-versa) with *P-values* < 10^{-6}. Figure 14 shows the peak HRR as a function of the THR. The larger the total fire heat release rate, the larger the peak HRR for these Douglas-fir trees of similar size.

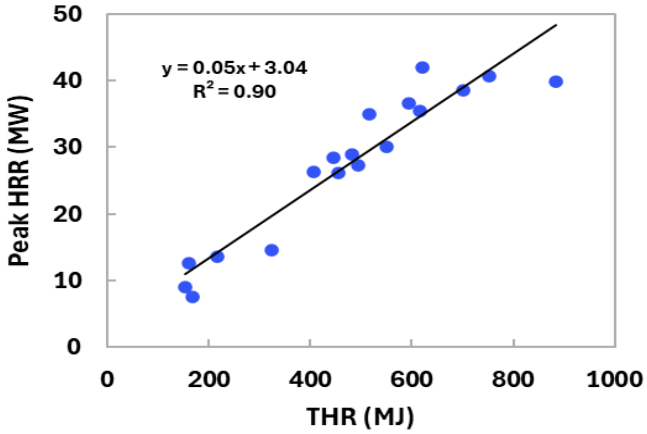

Figure 14. The peak HRR as a function of the THR. A best fit line is also shown. The average combined expanded uncertainties (k=2) of the peak and total HRRs are 8 %.

Figure 15 shows the peak HRR and the THR a function of tree height. As the tree height increased, there was a tendency for the peak HRR and THR to increase albeit with a significant amount of data scatter. A best fit power law function to the data is also shown in the plots. These results

might be expected as taller trees tended to have larger initial mass, larger mass burning rates, and larger fires.

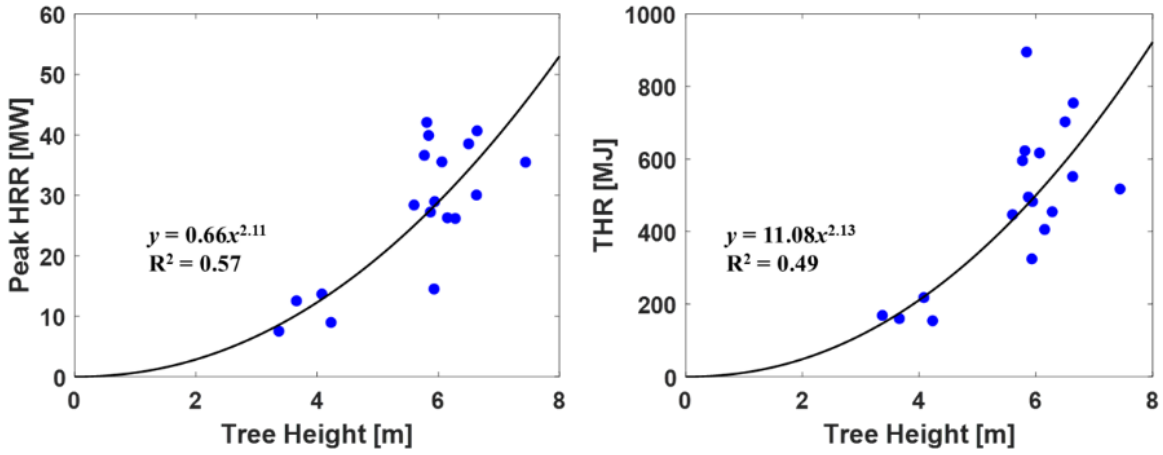

Figure 15. The peak HRR and the THR as a function of tree height. Best fits to a power function are also shown. The average combined expanded uncertainties (k=2) of the peak and total HRRs are 8 %.

Figure 16 shows the peak HRR and the THR as a function of tree moisture content (MC). There are no discernable trends in the data and the scatter is large. If, however, the data is replotted as the ratio of the peak HRR to the initial tree mass following Babrauskas [2016], then the relationship shown in Figure 17 results.

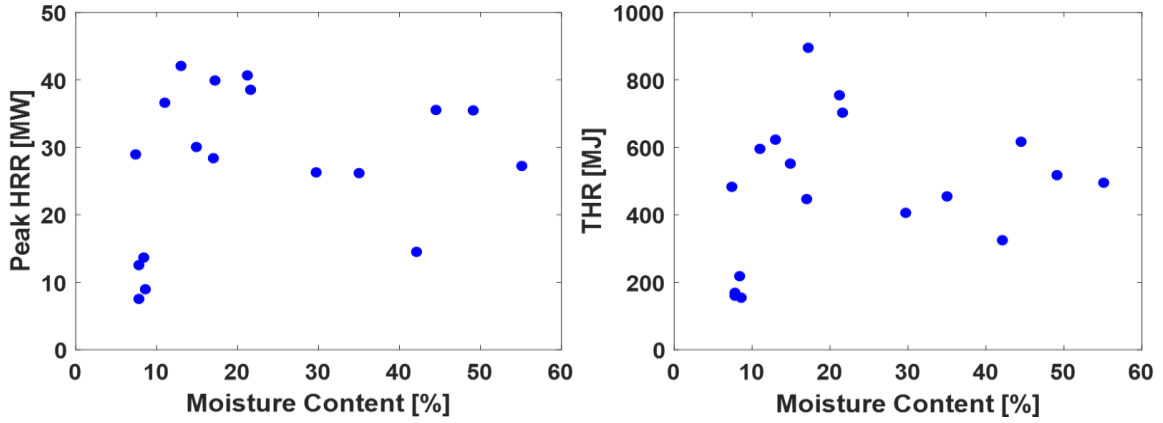

Figure 16. The peak HRR and the THR as a function of moisture content (MC). The average combined expanded uncertainties (k=2) of the peak and total HRRs are both 8 %.

Figure 17 also compares the results from the present study with the data compilation of Babrauskas [2016] for all types of trees, and to the results by Sung et al. [2026] for small Douglas-fir trees (< 2 m tall). Following the analysis of Babrauskas [2016], the best fit to all the data in Figure 17 uses a power law function. There is a noteworthy amount of data scatter, but the power law provides a rough estimate of the peak HRR from the two input parameters, namely the moisture content and initial tree mass. The results of the regression analysis described earlier confirmed that the Peak HRR is dependent on the initial tree mass in an extremely strong statistically significant manner (*P-value* < 0.005). Information on these types of relationships may be useful in the development of wildland fire spread models.

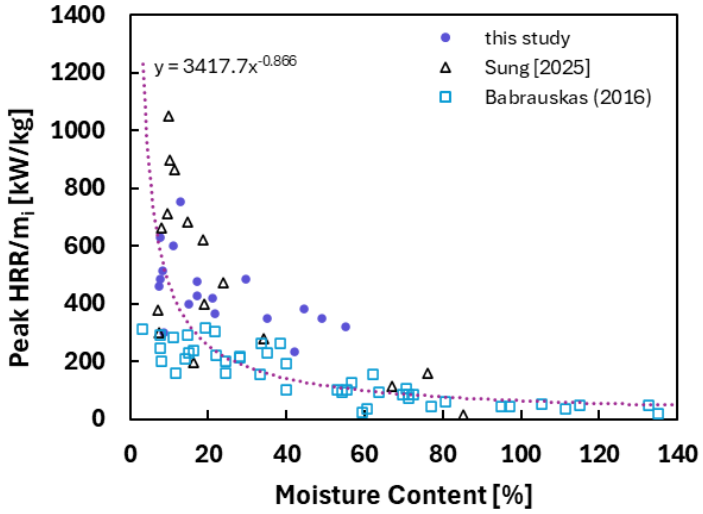

Figure 17. The ratio of the peak HRR to initial mass as a function of moisture content measured in this study and compared to the results from Sung et al. [2026] and Babrauskas [2016]. A best fit power law function to all the data in the plot is also shown.

3.3.1. Near-field Heat Flux

By design, the near-field heat flux measurement locations used in this study matched those of Mell et al. [2009]. The transient heat flux results measured using radiometers and PTs are plotted in Appendix D. Figure 18 shows the peak near-field heat fluxes as a function of tree height. The heat flux closer to the trees (r =2 m) was generally larger than the more distant sensors (r =3 m).

The heat flux tended to be larger for the larger trees. For the taller trees, larger peak values were generally observed at the 2.3 m measurement height location than at the 4.5 m height. This trend is likely due to the view factor effect of the heat flux gauges with the mid-height (z = 2.3 m) heat flux gauges viewing the bulk of the fire, whereas the highest gauges (z = 4.5 m) mainly viewed

the plume above the fire. Similarly, for the shorter trees, the z = 2.3 m and 4.5 m gauges measured similar heat fluxes, likely since the bulk of the tree itself was burning between the 0.2 m and the 2.3 m positions. At the 3 m radial distance, the peak heat flux values were generally higher at the z = 4.5 m sensor measurement location for all tree heights.

The present results are generally consistent with those of Mell et al. [2009]. The 2 m tall trees from Mell et al. [2009] had similar peak heat flux values comparable to the shortest trees in this study (Trees 1 and 2), particularly at the z = 2.3 m and 4.5 m measurement locations (within 4.5 % to 13.5 %). Furthermore, Mell's 5 m tall trees had a higher peak heat flux at the z = 2.3 m than at z = 4.5 m, in agreement with this study. Thus, the trends presented here match reasonably well with the trends observed by Mell et al. [2009]. It is important to note that the values from Mell et al. [2009] represent the average of several tree burns for each of the two tree sizes. While tree height and ignition symmetry influenced the measured heat flux, natural variation and the amount of mass burned were also important.

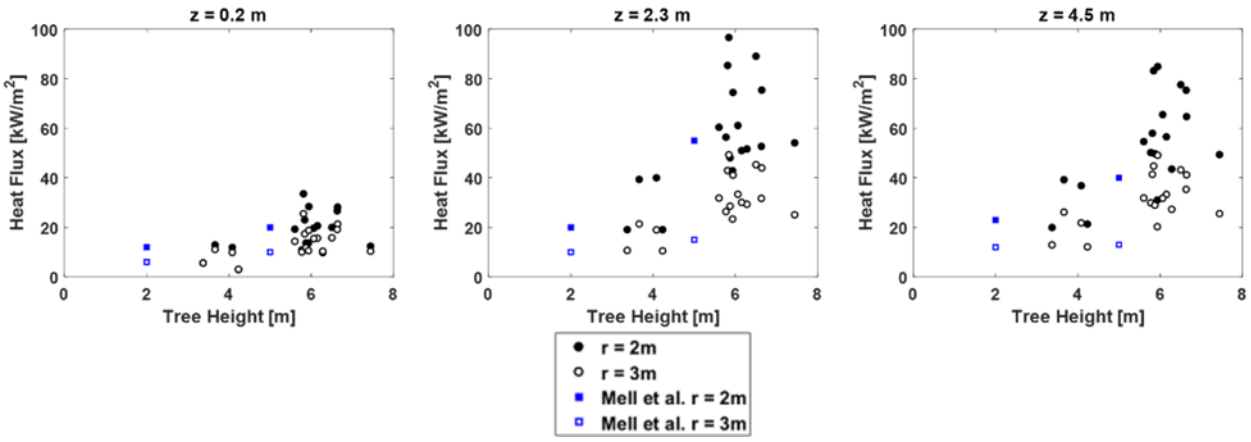

Figure 18. The near-field peak heat fluxes as a function of tree height for gauges located at three z positions. The average combined expanded (k=2) heat flux uncertainties were approximately 10 %. The results of Mell et al. [2009] are also shown.

Figure 19 shows the near-field peak heat flux measurements as a function of the tree moisture content. The data scatter is large and there is no observable trend in the data.

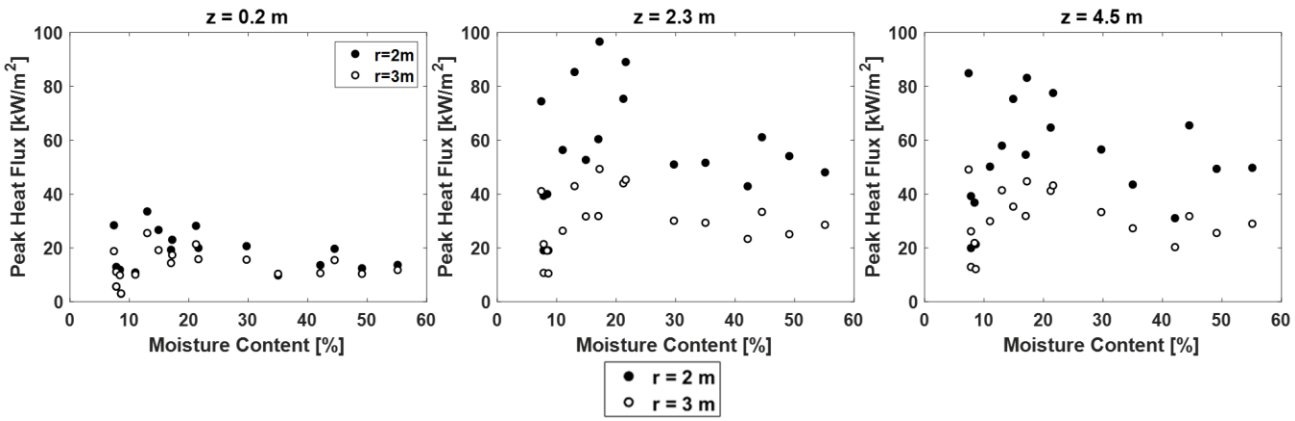

Figure 19. The near-field heat flux as a function of moisture content. The average combined expanded heat flux uncertainties were approximately 10 %.

3.3.2. Far-field Heat Flux

Figure D 37 to Figure D 54 in Appendix D show the transient far-field heat fluxes measured at radial distances of 10 m and 12 m from the trees. The peak heat fluxes monitored by the far-field gauges at a radial distance of r = 12 m are plotted in Figure 20 as a function of the peak HRR. As expected, the value of the peak heat fluxes measured at a distance of 10 m was significantly larger than the peak values at 12 m, with the ratio of the peak values approximately proportional to the inverse of the ratio of the square of the distance from the trees.

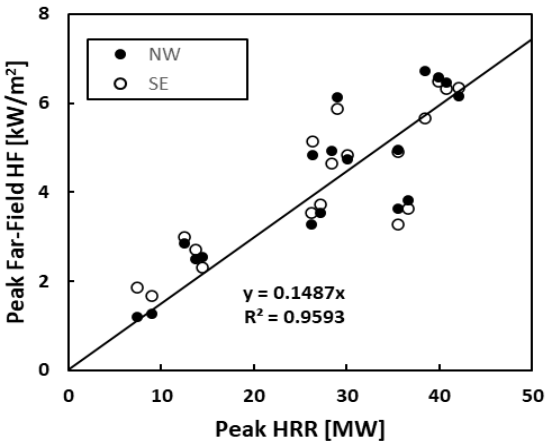

Figure 20. The peak far-field heat flux at r = 12 m measured by the northwest (NW) and southeast (SE) gauges as a function of the peak heat release rate. A best fit line forced through zero is also shown. The expanded (k=2) combined uncertainties are 8 % and 10 % for the peak HRR and peak far-field HF measurements, respectively.

For the cases of fires with asymmetric ignition (Trees 1, 3, and 5), the lower peak heat fluxes at both the near and far-fields are due to the entire tree not simultaneously burning. For these asymmetric ignitions, about half the tree first ignited and only then did the fire propagate to the unlit portions of the tree. This process caused instantaneous values (such as peak HRR and peak heat flux) to be lower, whereas the integrated HRR was similar to the trees that had symmetrical ignition.

Figure 21 shows the far-field (r=12 m) peak heat flux as a function of tree height. The figure shows that the pairs of far field heat flux gauges approximately track each other. As seen in Figure 15 for the peak HRR, Figure 21 shows a tendency for the peak HRR to increase with tree height albeit with a large amount of data scatter. These results might be expected as taller trees tended to have larger mass burning rates and larger fires.

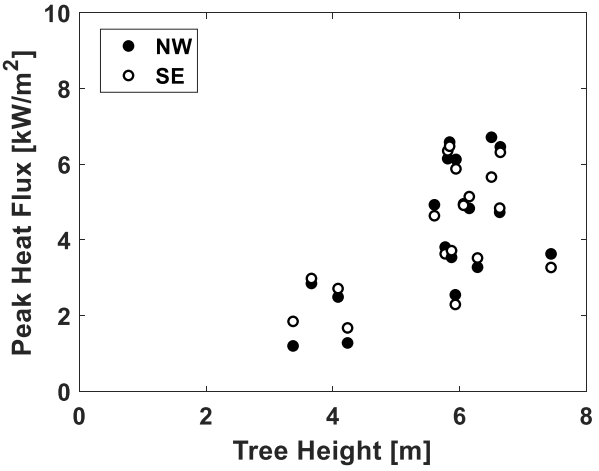

Figure 21. The far-field (r=12 m) peak heat fluxes as a function of tree height. The average expanded (k=2) combined uncertainty of the peak heat flux was about 10 %.

Figure 22 shows the far-field (r=12 m; see Figure 2) peak heat flux measurements as a function of the initial moisture content of the trees. The results were clustered in pairs as the NW far-field peak heat flux measurements were similar to those measured in the SE. There is no observable trend in the data.

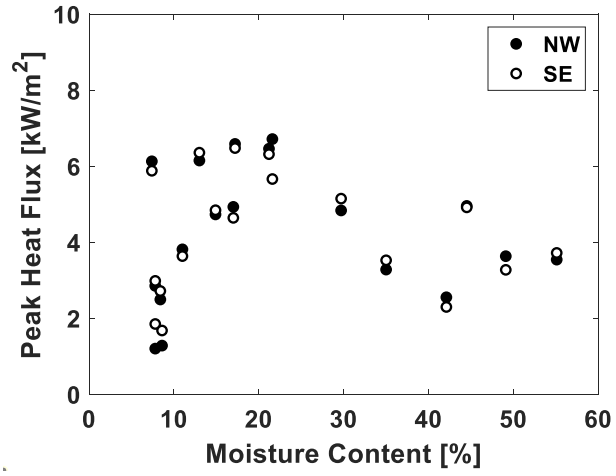

Figure 22. The far-field (r=12 m) peak heat flux as a function of tree moisture content. The expanded (k=2) combined uncertainty of the peak heat flux was about 10 %.

3.4. Total Radiated Energy and Radiative Fraction

The total radiated energy and radiative fraction (Eqs. 2 and 3) were estimated by integrating the transient radiative heat flux measured at the far-field locations (R = 12 m) over the experimental duration, invoking the assumption of spatial isotropy. To validate this approach, a numerical check was performed using the Fire Dynamics Simulator (FDS 6.11.0) [McGrattan et al., 2026] configured with 2000 radiation rays to model the Tree 4 fire (Test 4). The simulation demonstrated that the predicted radiative heat fluxes at R = 10 m and R = 12 m were within 12 % of each other, and both deviated by an average of 11 % from the theoretical value expected under a perfectly isotropic radiation field. Any geometric or spatial biases introduced by the simplifying assumption of isotropy is explicitly treated here as part of the overall uncertainty.

Figure 23 shows the calculated total radiated energy (TRE; see Eq. 2) as a function of the total heat release (THR) determined by calorimetry. As expected, the figure shows a strong linear trend between the total heat released and the total radiated energy. These results support the idea of a nearly constant value for the radiative fraction over the range of fire sizes considered in this study.

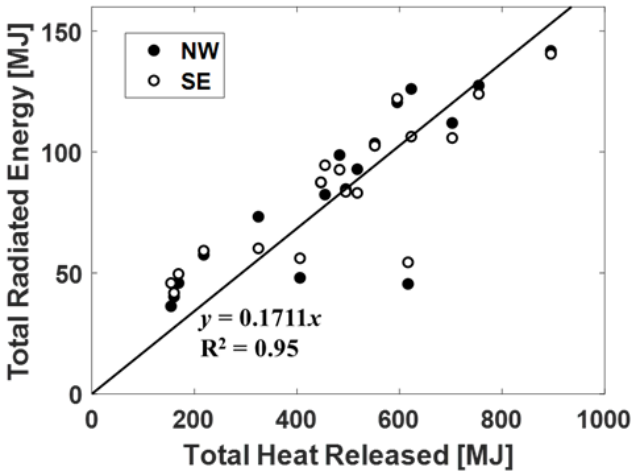

Figure 23. The total radiated energy (TRE) as a function of the total heat released (THR) by the fire (from calorimetry). A best fit line forced through zero is also shown. The average combined expanded (k=2) uncertainties of the TRE and THR are 16 % and 8 %.

Table 9 lists the measured total radiated energy (TRE) over the duration of the tests as defined in Equation 2 for each of the far-field radiometers (NW and SE positions) at r = 12 m. The values of the NW and SE results showed a significant difference for Trees 1, 3, 5, 7, 8, and 12 which had non-symmetric ignition, so differences in the transient far-field radiative flux measurements might be expected. Table 9 also lists the radiative fraction (χ_{rad}), which was estimated using the TRE data and Equation 3 (see Section 2.3.4). The χ_{rad} does not represent all the energy radiated by the specimen as some of the emitted radiative heat flux is absorbed by the specimen itself, obstructing that radiation from being emitted to the surroundings. There is fair agreement in Table 9 between the two far-field heat flux gauge locations (NW and SE) with the difference ranging from about 1 % to 10 % with a 4 % difference on-average.

Table 9. The total radiated energy determined from the far-field NW and SE heat flux gauges and the radiative fraction, χ_{rad}. The average combined expanded (k = 2) uncertainty of TRE and χ_{rad} is 19 % and 23 %, respectively.

Tree	TRE_{NW} [MJ]	TRE_{SE} [MJ]	χ_{rad}
1	57.4	55.6	0.29
2	46.9	46.6	0.29
3	44.4	49.6	0.27
4	69.6	67.6	0.29
5	153.7	129.0	0.24
6	152.4	170.3	0.32
7	82.4	94.6	0.20

Tree	TRE_{NW} [MJ]	TRE_{SE} [MJ]	χ_{rad}
8	73.3	60.2	0.19
9	84.7	83.6	0.19
10	92.9	83.1	0.20
11	48.0	56.1	0.14
12	45.5	54.4	0.09
13	98.7	92.7	0.20
14	103.6	102.6	0.17
15	141.8	140.6	0.15
16	87.4	87.5	0.19
17	105.8	108.9	0.15
18	124.0	125.7	0.17

Figure 24 shows the TRE at the NW and SE far-field heat flux gauges as a function of the moisture content of the trees. This figure shows a clear resemblance to Figure 21 with a tendency for the total radiated energy to increase with tree height. And like the peak HRR in Figure 21, the data scatter in Figure 24 appears to be large, which might be expected as taller trees tended to have larger mass burning rates and larger fires.

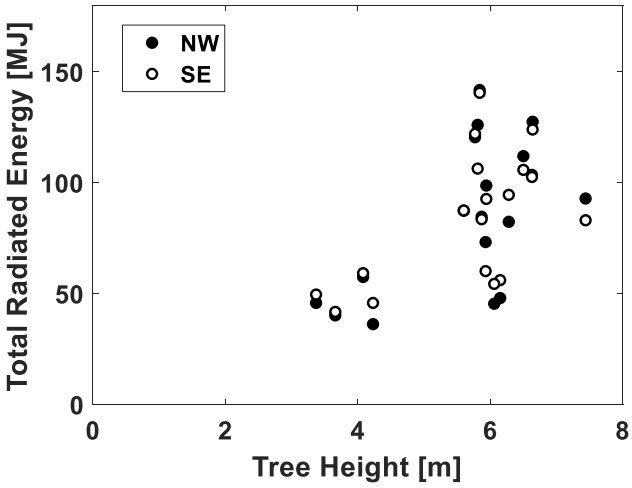

Figure 24. The total radiated energy at the NW and SE far-field heat flux gauges as a function of tree height. The average combined expanded (k=2) TRE uncertainty is 16 %.

Figure 25 shows the total radiated energy at the NW and SE far-field heat flux gauges as a function of the moisture content of the trees. No observable trends in the data are observed.

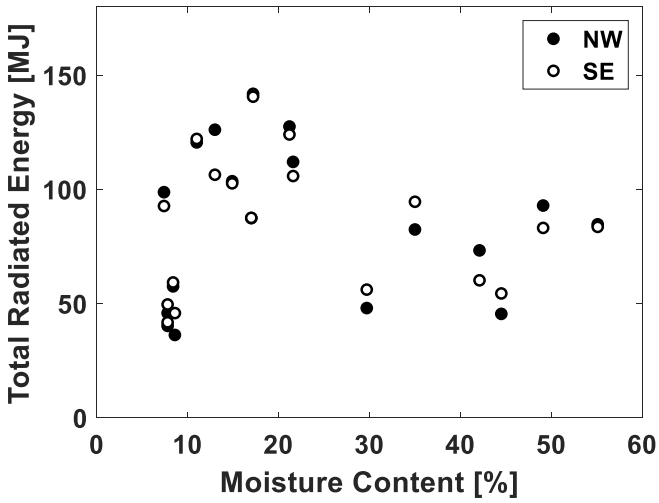

Figure 25. The total radiated energy at the NW and SE far-field heat flux gauges as a function of the dry moisture content of the trees (MC in Table 1). The average combined expanded (k=2) uncertainty of the TRE is 16 %.

Figure 26 shows χ_{rad} (defined in Eq. 3) as a function of the dry moisture content for all the experiments. The value of χ_{rad} appears to decrease with increased moisture content. Sung et al. [2026] also observed a decrease in χ_{rad} with moisture content for fires involving 1 m to 2 m tall Douglas-fir trees. For small (<2 m) Douglas fir trees with moisture content less than 15 %, Sung et al. [2025] found that χ_{rad} was equal to 0.28 ± 0.04, consistent with the results seen in Figure 26. This may be due to the fact that the moisture content of a tree can directly affect flame temperature, the rate of pyrolysis (and burning rate), as well as combustion efficiency. Water vapor released during burning of a moist tree dilutes the gas phase combustion processes, acting to cool the flame and slow the kinetics overall, including those associated with soot formation and growth. Tell-tale blue streaks were visually observed during some of the moist tree tests, indicating lower amounts of soot in the fires. This is consistent with flame studies that show that the addition of water to the fuel stream in non-premixed flames leads to lower flame temperatures and soot concentrations mainly due to reduced rates of PAH formation, soot growth, and higher rates of soot oxidation associated with dilution, thermal, and chemical effects [Escudero et al., 2023; Luo et al., 2025]. A multiple linear regression was conducted to determine the influence of MC, THR, the initial tree mass, the tree height, and crown volume on χ_{rad}. The results showed that only MC had a significant effect (P-value <0.02) on χ_{rad} with the P-value > 0.2 for the other parameters.

As discussed in the next section, smaller particulate matter yields were observed as the trees' moisture content increased, consistent with the finding that χ_{rad} decreased with increasing moisture content.

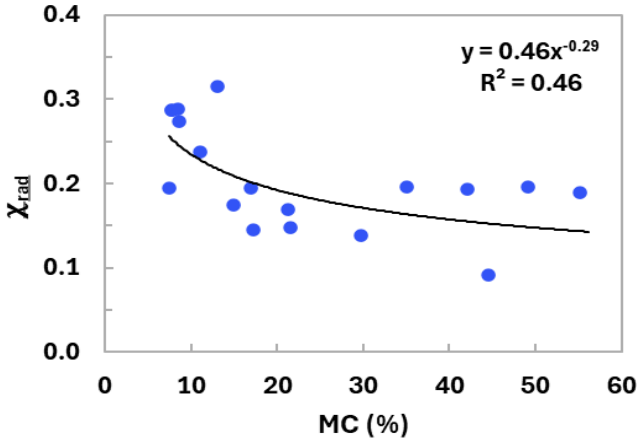

Figure 26. The radiative fraction as a function of dry moisture content of the trees. A best fit power law function to the data is also shown. The average combined expanded (k=2) uncertainty of χ_{rad} is 20 %.

3.5. Yield of Exhaust Products

Table 10 lists the total particulate matter (PM), CO, and CO_2 yields and the ratio of CO to PM on a mass basis. The measured PM and CO yields varied from about 0.002 to 0.006, and from 0.05 to 0.12, respectively. These are rather narrow ranges and the average values and standard deviations of the PM and CO yields for all the tests were 0.0036 ± 0.0006 and 0.091 ± 0.006, respectively. There were only small differences in the yields among the larger and smaller HRR fires, and there were no differences among the fires that had symmetric or non-symmetric ignitions (see Table 7). The largest values of the PM and CO yields were 0.0063 ± 0.0011 and 0.115 ± 0.009, respectively. In addition, the ratio of CO to CO_2 in the exhaust duct was 0.07 on-average, which is not unlike the exhaust from medium-scale hydrocarbon pool fires [Falkenstein-Smith, 2023].

Table 10. The measured particulate matter (PM), carbon monoxide (CO), and carbon dioxide (CO_2) yields, the CO to PM ratio, and their combined expanded (k = 2) uncertainties.

Test	PM Yield[a] [kg/kg]	CO Yield [kg/kg]	CO_2 yield [kg/kg]	Ratio of CO to PM (kg/kg)
1	0.0054 ± 0.0007	0.087 ± 0.005	1.7 ± 0.1	16.2 ± 2.2
2	0.0041 ± 0.0006	0.082 ± 0.005	1.9 ± 0.1	20.0 ± 2.8
3	0.0050 ± 0.0007	0.081 ± 0.005	1.8 ± 0.1	16.2 ± 2.2

Test	PM Yield[a] [kg/kg]	CO Yield [kg/kg]	CO_2 yield [kg/kg]	Ratio of CO to PM (kg/kg)
4	0.0034 ± 0.0005	0.086 ± 0.005	1.8 ± 0.1	25.1 ± 3.4
5	0.0054 ± 0.0007	0.101 ± 0.006	1.6 ± 0.1	18.6 ± 2.5
6	0.0039 ± 0.0005	0.047 ± 0.003	1.2 ± 0.1	12.0 ± 1.7
7	0.0029 ± 0.0004	0.102 ± 0.005	1.6 ± 0.1	35.0 ± 4.6
8	0.0024 ± 0.0006	0.109 ± 0.024	1.8 ± 0.4	45.0 ± 11.4
9	0.0023 ± 0.0004	0.097 ± 0.011	1.7 ± 0.2	41.6 ± 7.1
10	0.0021 ± 0.0008	0.096 ± 0.034	1.6 ± 0.6	46.1 ± 17.3
11	0.0042 ± 0.0006	0.104 ± 0.006	1.9 ± 0.1	25.1 ± 3.5
12	0.0031 ± 0.0007	0.109 ± 0.015	2.3 ± 0.3	35.6 ± 7.8
13	0.0063 ± 0.0011	0.115 ± 0.009	1.9 ± 0.1	18.4 ± 3.3
14	0.0030 ± 0.0005	0.103 ± 0.005	1.9 ± 0.1	34.7 ± 6.4
15	0.0039 ± 0.0005	0.113 ± 0.005	1.8 ± 0.1	28.6 ± 3.9
16	0.0034 ± 0.0005	0.113 ± 0.008	2.0 ± 0.1	33.0 ± 4.8
17	0.0031 ± 0.0006	0.111 ± 0.015	1.9 ± 0.3	35.7 ± 6.6
18	0.0039 ± 0.0006	0.111 ± 0.006	1.7 ± 0.1	28.4 ± 4.0

The PM and CO yields in these fires are similar to those measured during the burning of 1 m to 2 m Douglas-fir trees [Sung et al., 2025; 2026]. And the CO yield was not unlike the values measured in the exhaust of a lightly sooting 34 kW propane fire [Falkenstein-Smith, 2023]. Tewarson [2016] reports that the CO yield from solid wood small (10 cm) Douglas-fir samples burning in air in the Fire Propagation Apparatus (FPA) is 0.004, which is about a factor of two lower than the values in Table 10 for the large Douglas-fir trees tested here. This difference is not surprising as the solid wood FPA samples were likely thermally thick and relatively small when tested in the FPA [ASTM E2058, 2013].

A multiple linear regression was conducted to determine the influence of the peak HRR, THR, MC, initial tree mass, tree height, crown volume, bulk density, and χ_{rad} on the PM and CO yields and the CO yield to PM yield ratio. The results showed little statistical significance of the parameters on the PM and CO yields. There was clear statistical significance, however, with the CO/PM ratio. The calculated *Significance F* value was approximately equal to 10^{-4} with a highly strong statistical significance associated with MC (*P-value < 0.0002*) and a statistically significant relationship with THR (*P-value < 0.05*).

The CO and PM yields as a function of MC are presented in Figure 27. As the tree moisture content increased, the PM yield decreased whereas the CO was nearly flat with only an extremely small positive slope. The results in Figure 27 are consistent with those of Figure 24 in which the

radiative fraction tends to decrease with moisture content; hot soot emission is a key factor contributing to radiative emission. With less soot in the fire, less radiative emission is expected.

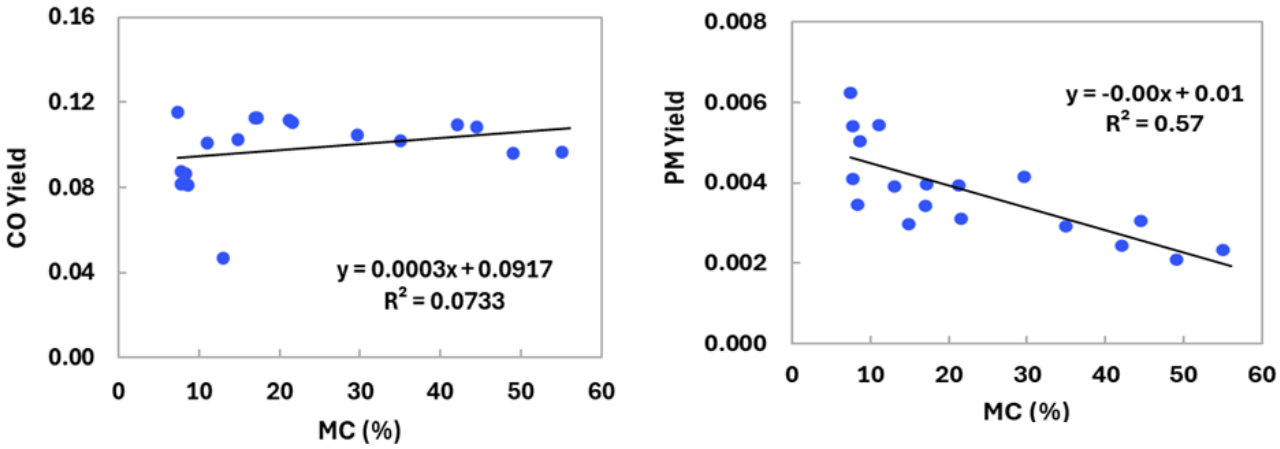

Figure 27. The yields of CO and particulate matter as a function of the moisture content (MC). Best-fit lines are also shown. The average combined expanded (k=2) uncertainty of the CO and PM yields was 10 % and 17 %, respectively.

These fires did not appear to be very smoky. Bluish streaks[4] were observed on the edge of some of the moist luminous fire plumes. This observation is consistent with the idea of relatively small particulate matter yields seen in Figure 27 for the trees characterized by relatively large values of MC. This relationship is consistent with fundamental diffusion flame studies (Dryer, 1977.

Figure 28 shows the relationship between the ratio of CO yield to PM yield as a function of MC. As MC increased, the ratio increased. This is consistent with the combustion literature. As mentioned in Section 3.4, the addition of water to the fuel stream in non-premixed flames leads to lower flame temperatures and soot concentrations mainly due to reduced rates of PAH formation, soot growth, and higher rates of soot oxidation associated with dilution, thermal, and chemical effects [Escudero et al., 2023; Luo et al., 2024]. Non-premixed flame studies prove that the relationship between fuel moisture and CO yield is highly complex. [Park et al., 2007] Adding small amounts of water to the fuel stream of a non-premixed flame decreases the CO yield by kinetically enhancing the production of oxidizing radicals that efficiently convert CO into CO_2. If moisture heavily dilutes the fuel, its heat capacity acts as a thermal sink to cool the flame and freeze the oxidation reactions, allowing CO to escape the flame. Dilution by water

[4] The bluish streaks that were observed are not visible in the over-exposed videos on the FCD. These features are generally challenging to record by video.

effectively interrupts the kinetic pathways required for soot growth. As a result, complete carbon conversion to CO_2 is kinetically constrained, leaving a greater fraction of fuel-bound carbon partially oxidized as CO rather than soot consistent with the results in Figure 28.

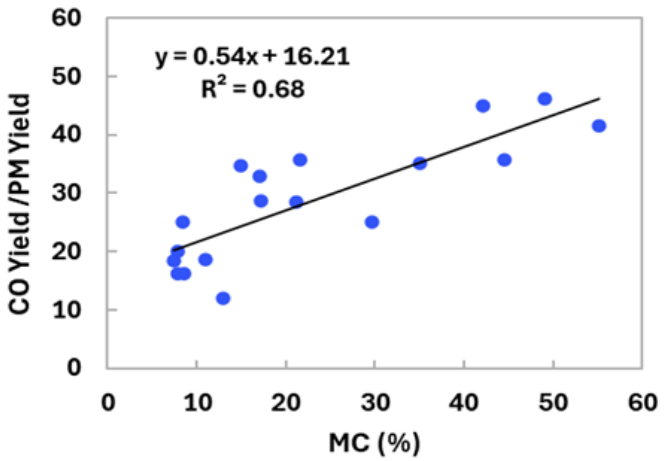

Figure 28. The ratio of the CO yield to the PM yield as a function of the moisture content. A best fit line to the data is also shown. The average combined expanded (k=2) uncertainty of the CO/PM ratio was 17 %.

Appendix F describes PAH measurements made in the fire exhaust plumes and compares the optical and the gravimetric PM measurements. Many types of PAHs were identified and quantified. The results show that the PAH yields in Test 10 (MC = 49 %) were generally smaller than those in Test 8 (MC = 42 %). This is consistent with the idea that water acts to suppress PAH and soot in flames (see discussion in Section 3.4,). Additional PAH data from tree fires is needed to confirm this trend.

3.6. Analysis of Branch Tips

After the fire tests, nearly all the needles were gone from the dry Douglas-fir trees, and the tree trunk and branches had a thin (~1 mm) carbonaceous layer. Many of the branch tips appeared to have burned. A survey of the branch tip diameters was conducted to determine how the tip diameters differed before and after a burn. Samples from two trees (Trees 17 and 18) were harvested at five heights (approximately 1 m, 2 m, 3 m, 4 m, and 5 m from the tree base) the day before the trees were burned. At each height, about 10 cm to 15 cm of each branch was cut for processing and measurement. A light table was used to enhance the photographic analysis. Figure 29 presents photos of some of the steps involved in processing each branch. Needles and buds were removed and the stems were cut into 2.5 cm sections. A MATLAB routine was written to analyze the stem images and produce the average and standard deviation of the stem

diameters using several hundred measurements per image. A photo of a drill bit with known diameter was used to calibrate the image analysis.

The results are plotted in Figure 30. Some branch tips that had been clearly pruned were removed from the data set. If error bars were plotted in the figure, they would be about the size of the symbols themselves. High in the trees, the branch tip diameters were as large as 4 mm and consistently larger than 1.5 mm. The figure shows a rough trend of increasing branch tip diameter with height above the tree stand base.

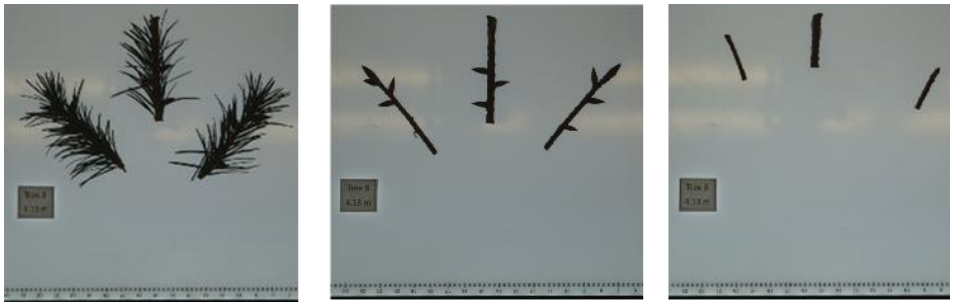

Figure 29. Photographs of the progression of processing steps, removing needles from a branch tip to measure the stem thickness, then placing them on a light table for analysis.

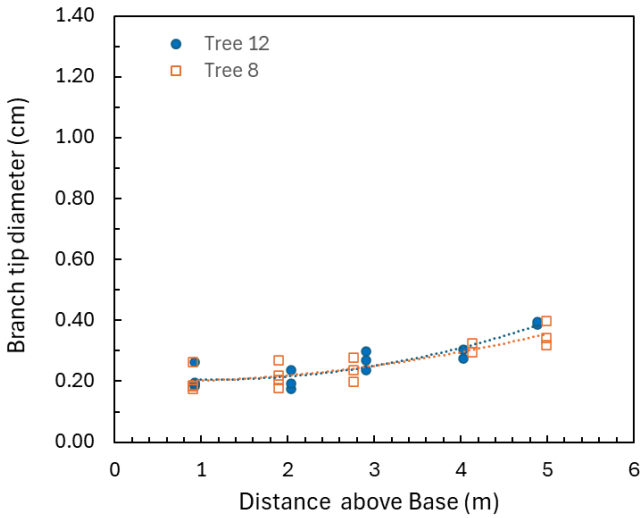

Figure 30. Branch tip diameter versus distance above the tree stand base for Trees 8 and 12 before burning.

Figure 31 and Figure 32 show the measured post-fire branch tip diameters as a function of distance above the stand base for Trees 4 and 6, respectively. The results show that the branch tip diameters varied from about 3 mm to as large as 12 mm. As expected, the post-fire tips were significantly larger than the unburned branch tips seen in Figure 30. For Tree 6, a best fit line of the branch tip diameters as a function of height yields a positive slope albeit with a relatively small R^2 value (= 0.37). Tree 6 was almost 6 m tall, significantly taller than the 4 m tall Tree 4. With its much larger fire plume, the top branches of Tree 6 would have experienced larger vertical plume velocities and higher heat fluxes, which would have led to more intense burning higher in the tree. Consequently, this would lead to larger branch tips as more of the smaller tips burned away. Figure 31 shows that the branch tip diameters of Tree 4 increased with distance above the base like Tree 6 (Figure 32), but the branch tips decreased in diameter near the burned tree tops. Further work is needed to better understand the relationship between burning behavior and branch diameter.

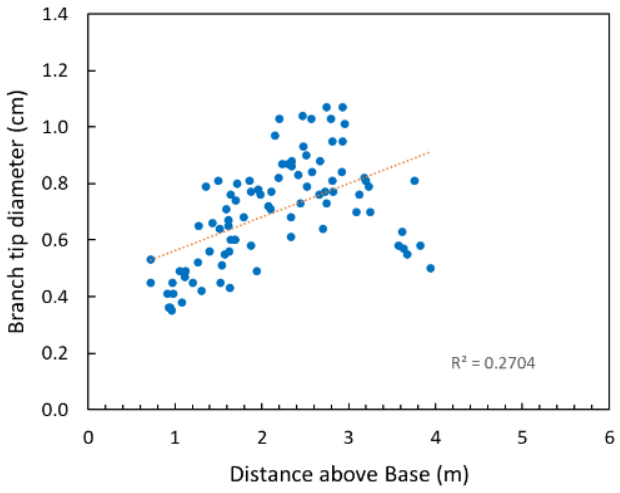

Figure 31. The branch tip diameter as a function of distance above the tree stand base for Tree 4 post-fire.

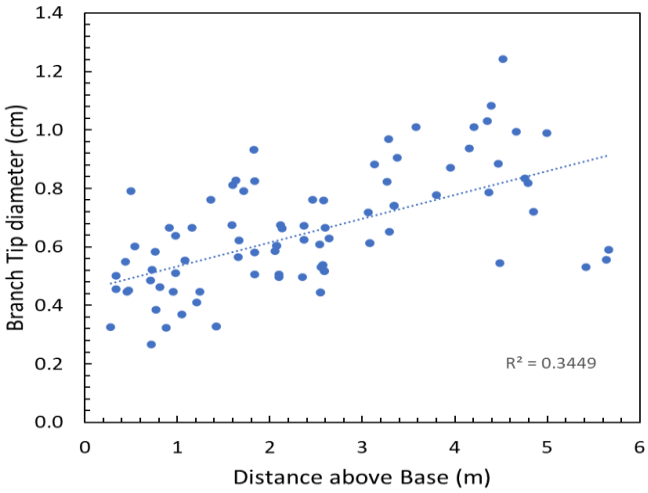

Figure 32. The branch tip diameter as a function of distance above the tree stand base for Tree 6 post-fire.

4. Summary and Conclusions

This study characterizes the fire behavior of 18 dry Douglas-fir trees with heights ranging from 3.3 m to 7.4 m, burning under well-ventilated quasi-quiescent conditions through the use of a well-characterized 20 MW calorimeter. Varying the dry basis moisture content (MC) from 7 % to 55 %, the study provides quantification of global combustion properties, including the peak and total heat release rates (HRR), the product yields, and the radiative fraction. The results have been integrated into the NIST Fire Calorimetry Database to support research and the development of realistic design fire scenarios. A number of key findings include the following:

- Achieving uniform ignition of the lower branches with the natural gas burner proved to be difficult.
- Uniform ignition of the tree was challenging. Poor contact between burner flames and foliage led to non-uniform ignition of some of the lower tree branches for several tests. Asymmetric ignition led to asymmetric burning of the tree such that lower peak HRRs occurred compared to the experiments with uniform burner ignition and symmetric burning. For both symmetric and asymmetric tree ignitions, similar total mass losses were observed for trees of similar size despite differences in their temporal HRR curves, peak values, and even apparent amounts of remaining unburned foliage.
- Photogrammetry is an effective method to characterize the gross details of the tree structure. The approach enabled a three-dimensional reconstruction of the tree crown, providing volume estimates used to calculate crown bulk density - a key parameter in quantifying and modeling vegetation burning dynamics.
- The total heat release measured by calorimetry and the ideal heat release calculated from the product of the integrated mass loss rate and the heat of combustion agreed within experimental uncertainty. The average difference for all the trees from parity was equal to about 9 %.
- The trends of the near-field heat flux measurements at 2 m and 3 m from the tree center are consistent with the results from similar experiments reported by Mell et al. [2009]. The radiative fraction of the Douglas-fir tree fires investigated here was estimated by integrating the transient radiative heat flux measured in the far-field. Its value significantly decreased with tree moisture content. The measured particulate matter yield also decreased with moisture content – consistent with the trends in the radiative fraction.
- The yield of particulate matter determined gravimetrically was a factor of 3 to 5 times larger than its value determined optically - the larger the moisture content, the larger the factor. This suggests that either the mass specific extinction coefficient used in the optical PM

calculation (= 8.7 m^2/g) may be significantly off for these large Douglas-fir tree fires or that water was not completely removed from the gravimetric soot samples. Further work on this topic is needed.

- Unsurprisingly, the branch tip diameters were generally found to increase after burning. As the trees burned, many of the branch tips burned away, leaving thicker stems - some as large as 1.2 cm. Higher in the tree, the branch tips tended to have larger diameters until a maxima was obtained at about 90 % of the tree height, where the branch tip diameters decreased. This type of information may be useful to computational fluid dynamics fire models of tree burning. Further research on this topic is needed.

Although a few previous studies have considered trees over 2 m tall, none have provided such a complete set of global burning properties. The results, available on the NIST Fire Calorimetry Database (FCD), provide unique calorimetric data that may be useful for development of design fire scenarios by fire protection engineers or by fire modelers interested in validation data. Further studies are needed to investigate whether the relationships identified here for 3 m to 7 m tall Douglas-fir trees hold true for a broad range of trees and shrubs.

5. References

Accary G, Darido J, Morvan D (2024) Experimental and Numerical Investigation of a Single-tree Fire, *Journal of Fire Sciences,* 42, 142-170. https://doi.org/10.1177/07349041231218967

ASTM International (2019) ASTM D5865/D5865M-19 -- Standard Test Method for Gross Calorific Value of Coal and Coke*, ASTM International*, West Conshoshocken, PA, USA. https://www.astm.org/d5865_d5865m-19.html

ASTM International (2013) ASTM E2058-13 -- Standard Test Method for Measurement of Material Flammability Using a Fire Propagation Apparatus (FPA), *ASTM International*, West Conshoshocken, PA, USA. https://www.astm.org/standards/e2058

ASTM International (2024) ASTM E2067-24 -- Standard Practice for Full-Scale Oxygen Consumption Calorimetry Fire Tests, *ASTM International*, West Conshoshocken, PA, USA. https://www.astm.org/standards/e2067

Babrauskas V (2016) Heat Release Rates in: *The SFPE Handbook of Fire Protection Engineering, 5th Ed.,* New York, NY, Springer, Hurley M (Editor), Vol. 1, Chapter 26, 799-904. https://www.sfpe.org/publications/handbooks/sfpehandbook.

Babrauskas V, Peacock RD (1992) Heat Release Rates: The Single Most Important Variable in Fire Hazard, *Fire Safety Journal,* 18, 255-272. https://doi.org/10.1016/0379-7112(92)90019-9

Babrauskas V, Chastagner G, Stauss E (2001) The Heat Release Rate Hazard of Christmas Trees, Chapter V in Flammability of Cut Christmas Trees, *International Association of Arson Investigators (IAAI) Annual General Meeting and Conference*, Atlantic City NJ (2001). https://doctorfire.com/pages/ChristmasTreeFires.pdf (accessed 23 Feb. 2026).

Bigda K (2021) Christmas Tree Fire Safety Requirements, *National Fire Protection Association (NFPA)* , Quincy, MA. https://www.nfpa.org/news-blogs-and-articles/blogs/2021/11/12/christmas-tree-fire-safety-requirements (accessed 23 Feb. 2026)

Bobroff N (1986) Position measurement with a resolution and noise-limited instrument. *Review of Scientific Instruments*, *57*(6), 1152–1157. https://doi.org/10.1063/1.1138619

Bryant R, Bundy M (2019) The NIST 20 MW Calorimetry Measurement System for Large-Fire Research, *NIST Technical Note 2077*, National Institute of Standards and Technology, Gaithersburg MD. https://doi.org/10.6028/NIST.TN.2077

Bryant R, Johnsson E, Ohlemiller T, Womeldorf C, Estimates of the Uncertainty of Radiative Heat Flux Calculated from Total Heat Flux Measurements, in *Proc. 9th Interflam Conference in Edinburgh, Interscience Communications London*, pp 605-616, (2001).

Davis AY, Cleary TG, Falkenstein-Smith RL, Bryant RA (2025A) Burning Characteristics and Smoke Emission from Mixed Fuel Cribs. *American Chemical Society Environmental Science & Technology Air,* 2(4), 540‑547. https://doi.org/10.1021/acsestair.4c00275

Davis A, Falkenstein-Smith R, Cleary T (2025B) Polycyclic aromatic hydrocarbons and select inorganics in smoke from various WUI fire fuels: Vehicles, trees, and construction materials, *NIST Technical Note (NIST TN) 2354*, National Institute of Standards and Technology, Gaithersburg, MD. https://doi.org/10.6028/NIST.TN.2354

Davis A, Falkenstein-Smith R, Cleary T (2024) Polycyclic Aromatic Hydrocarbon Analysis in Propene Smoke Using Thermal Desorption: Gas Chromatography – Mass Spectrometry. NIST *Technical Note (NIST TN) 2321,* National Institute of Standards and Technology, Gaithersburg, MD. https://nvlpubs.nist.gov/nistpubs/TechnicalNotes/NIST.TN.2321.pdf

Di Cristina G, Johnsson E, Mueller E, Bundy M, Hamins A (2025) Large-Scale Calorimetry Time Response Characterization and Correction, *Fire Safety J* , 158, 104531. https://doi.org/10.1016/j.firesaf.2025.104531

Dietenberger M, Hasburgh LE, Yedinak K (2021) Fire Safety of Wood Construction, Chapter 18 in Ross R and Anderson JR (Eds) Wood Handbook—Wood as an Engineering Material, *General Technical Report FPL-GTR-282*, Madison, WI: U.S. Department of Agriculture, Forest Service, Forest Products Laboratory. https://www.fs.usda.gov/research/treesearch/62200

Dietenberger M (2002) Update for Combustion Properties of Wood Components, *Fire and Materials,* 26, 25-267. https://doi.org/10.1002/fam.807.

Escudero F, Littin M, Demarco R, Liu F, Fuentes A (2023) Sooting Properties of Laminar Coflow Non-premixed Ethylene/Hydrogen Flames Influenced by Water Vapor Addition to the Oxidizer, *Fire Safety Journal,* 141, 103997. https://doi.org/10.1016/j.firesaf.2023.103997.

Falkenstein-Smith RL, Sung K, Hamins A (2023) Characterization of Medium-Scale Propane Pool Fires, *Fire Technology,* 59, 1865-1882. https://dx.doi.org/10.1007/s10694-023-01412-9.

Glassman I, Yetter RA, Glumac NG (2014) Combustion, 5th ed., *Academic Press (Elsevier)*, Waltham, MA.

Guo H, Gao Y, Ye Z, Yang Z, Zhang Y, Lei Z, Sun A (2025) Experimental investigation of fire behaviours and heat transfer in single cypress tree crown fires. *Int J Wildland Fire* 34, WF24030. https://doi.org/10.1071/WF24030

Halir R, Flusser J (1998) Numerically Stable Direct Least Squares Fitting of Ellipses, in *Proc. 6th International Conference in Central Europe on Computer Graphics and Visualization*, WSCG, 98, 125-132, Plzen-Bory: Citeseer. https://api.semanticscholar.org/CorpusID:15772208

Hamins A (1993) Soot in Environmental Implications of Combustion Processes, Chapter 3, *CRC Press,* Boca Raton, FL, 71-95. https://www.nist.gov/publications/soot

Hoehler MS, Bundy MF, DeLauter L, Materese R, Geršković L, García JR (2020) Fire Hazards of Dry Versus Watered Christmas Trees, *NIST Technical Note 2131*, National Institute of Standards and Technology, Gaithersburg, MD. https://doi.org/10.6028/NIST.TN.2131

Huskeflex Thermal Sensors (2024) SBG01 Water-Cooled Heat Flux Sensor Technical Information Sheet. https://www.hukseflux.com/uploads/product-documents/SBG01_v2313.pdf (accessed 23 Feb. 2026).

Johnsson E, Di Cristina G, Mueller E, Bundy M, Chakalis A, Fernandez, M, Hamins A (2025) The Burning Characteristics of 3 m to 6 m Dry Douglas-Fir Trees, *NIST Technical Note 2327r1*, National Institute of Standards and Technology, Gaithersburg, MD. https://doi.org/10.6028/NIST.TN.2327r1

Leroy V, Cancellieri D, Leoni E (2009) Relation between Forest Fuels Composition and Energy Emitted During Their Thermal Degradation, *Journal of Thermal Analysis and Calorimetry 96*, 293-300 https://doi.org/10.1007/s10973-008-9587-9

Linder W (2003) Digital Photogrammetry, Theory and Applications, *Springer-Verlag*, Berlin, Germany. https://doi.org/10.1007/978-3-662-06725-3

Luo G, Zhang Y, Liu B, Liu J, Xu, B, Takyi SA (2025) Effect of Adding N2/H2O to Ethylene Laminar Diffusion Flame on Soot Formation, *J. Energy Res. Technol. Part A* 1*,* 012301. https://doi.org/10.1115/1.4066283

Maddams WF (1980) The shape of structureless sub-bands in linear or non-linear curve fitting. *Applied Spectroscopy*, 34(3), 245–267. https://doi.org/10.1366/0003702804730312

Marcozzi AA, Johnson JV, Parsons RA, Flanary SJ, Seielstad CA, Downs JZ (2023) Application of LiDAR derived fuel cells to wildfire modeling at laboratory scale, *Fire, 6*(10), 394. https://doi.org/10.3390/fire6100394

McGrattan K, McDermott R, Vanella M, Mueller E, Hostikka S, Floyd J, Chandan P (2026) Fire Dynamics Simulator User's Guide, Version 6.11.0-0-g369a20b, NIST Special Publication 1019, Sixth Ed., National Institute of Standards and Technology, Gaithersburg, MD. http://dx.doi.org/10.6028/NIST.SP.1019

Mell W, Maranghides A, McDermott R (2009) Numerical Simulation and Experiments of Burning Douglas-fir Trees, *Combust Flame,* 156, 2023-2041. https://doi.org/10.1016/j.combustflame.2009.06.015

Michelsen HA (2017) Probing Soot Formation, Chemical and Physical Evolution, and Oxidation: A Review of in Situ Diagnostic Techniques and Needs, *Proc Combust Inst* 36, 717-735. https://doi.org/10.1016/j.proci.2016.08.027.

Modak A T, Thermal Radiation from Pool Fires, *Combustion and Flame*, ***29***, 177-192, (1977), https://doi.org/10.1016/0010-2180(77)90106-7.

Modarres M, Almeida M, Viegas DX (2024) Experimental and Numerical Fire Behaviour Analysis in Eucalyptus Globulus Trees, *International Journal of Wildland Fire*, 33(11). https://doi.org/10.1071/WF23131

Mulholland GW, Croarkin C (2000) Specific Extinction Coefficient of Flame Generated Smoke, *Fire and Materials* 24, 227–230, (2000). http://doi.org/10.1002/1099-1018(200009/10)24:5<227::aid-fam742>3.0.co;2-9

Mulholland GW, Johnsson EL, Fernandez MG, Shear DA (2000) Design and Testing of a New Smoke Concentration Meter, *Fire and Materials*, 24(5),231–243. https://doi.org/10.1002/1099-1018(200009/10)24:5%3C231::AID-FAM743%3E3.0.CO;2-N

National Instruments Inc., *SCXI-1600 User Manual and Specifications*, 2004.

Park J, Keel SI, Yun JH (2007) Addition Effects of H_2 and H_2O on Flame Structure and Pollutant Emissions in Methane–Air Diffusion Flame, *Energy & Fuels* 21 (6), 3216-3224. 10.1021/ef700211m

Parker W J, Levan SL (1989) Kinetic Properties of the Components of Douglas-Fir and the Heat of Combustion of Their Volatile Pyrolysis Products, *Wood and Fiber Science,* 21, 289-305. https://wfs.swst.org/index.php/wfs/article/view/1687

Pitts WM, Murthy AV, De Ris JL, Filtz JR, Nygård K, Smith D, Wetterlund I (2006) Round Robin Study of Total Heat Flux Gauge Calibration at Fire Laboratories, *Fire Safety Journal,* 41, 459-475. https://dx.doi.org/10.1016/j.firesaf.2006.04.004

Putorti A (2015) Characterizing the Thermal Effects of High Energy Arc Faults. *SMiRT 23 – 14th International Seminar on Fire Safety in Nuclear Power Plants and Installations (GRS-A-3845)*, Salford, UK. https://www.nist.gov/publications/characterizing-thermal-effects-high-energy-arc-faults

Safdari MS, Rahmati M, Amini E, Howarth J E, Berryhill J P, Dietenberger M, Weise D R, Fletcher TH (2018) Characterization of Pyrolysis Products from Fast Pyrolysis of Live and Dead Vegetation Native to the Southern United States, *Fuel,* 229, 151-166. https://doi.org/10.1016/j.fuel.2018.04.166

Scaniverse. Version 4, Niantic Inc., 2024, App Store.

Schneider L, Betting B, Patterson M, Skowronski N, Simeoni A (2021) Experimental Study of Fire Spread through Discontinuous Fuels Without Flame Contact, *Fire Safety Journal,* 120, 103066. https://doi.org/10.1016/j.firesaf.2020.103066

Seader JD, Einhorn IN (1977) Some Physical, Chemical, Toxicological, and Physiological Aspects of Fire Smokes, *Proc. Combustion Institute,* 16, 1423-1445. https://doi.org/10.1016/S0082-0784(77)80426-8

Seader JD, Einhorn IN (1977) Some Physical, Chemical, Toxicological, and Physiological Aspects of Fire Smokes, *Symp. (Int.) Combust 16*, 1423–1445. https://doi.org/10.1016/S0082-0784(77)80426-8.

Simeoni A, Salinesi P, Morandini F (2011) Physical Modelling of Forest Fire Spreading through Heterogeneous Fuel Beds, *International Journal of Wildland Fire,* 20, 625-632. https://doi.org/10.1071/WF09006

Sivathanu, Y. R., & Gore, J. P. (1993). Total radiative heat loss in jet flames from single point radiative flux measurements. *Combustion and Flame*, *94*(3), 265–270. https://doi.org/10.1016/0010-2180(93)90073-c

Sung K, Mueller E, Bundy M, Fernandez M, Hamins A (2025) Global Burning Properties of Little Bluestem, Excelsior and Douglas-fir, *NIST Technical Note (NIST TN) 2314*, National Institute of Standards and Technology, Gaithersburg MD. https://doi.org/10.6028/NIST.TN.2314

Sung K, Mueller E, Bundy M, Fernandez M, Hamins A (2026) Effects of Moisture, Bulk Density, Orientation, and Fuel Type on the Burning Characteristics of Three Vegetative Fuel Types, *Fire Safety J*, 162 , 104674. https://doi.org/10.1016/j.firesaf.2026.104674.

Susott RA (1982) Characterization of the Thermal Properties of Forest Fuels by Combustible Gas Analysis, *Forest Science,* 28, 404-420.

Susott RA, DeGroot WF, Shafizadeh F (1975) Heat Content of Natural Fuels, *Journal of Fire and Flammability,* 6, 311-325.

Taylor BN and Kuyatt CE, *Guidelines for Evaluating and Expressing the Uncertainty of NIST Measurement Results*, NIST Technical Note 1297, National Institute of Standards and Technology, Gaithersburg, MD, September 1994. https://www.nist.gov/pml/nist-technical-note-1297

Tewarson A (2016) Appendices in *The SFPE Handbook of Fire Protection Engineering* (ed: Hurley M), Vol. 1, Chapter 26, 5th Ed., New York, NY, Springer, pp 799-904. https://www.sfpe.org/publications/handbooks/sfpehandbook.

Weise DR, Fletcher TH, Johnson TJ, Hao WM, Dietenberger M, Princevac M, Butler BW, McAllister SS, O'Brien JJ, Loudermilk L, Ottmar RD, Hudak AT, Kato A, Shotorban B, Mahalingam S, Myers TL, Palarea-Albaladejo J, Baker SP (2022) Comparing Gas Composition from Fast Pyrolysis of Live Foliage Measured in Bench-Scale and Fire-Scale Experiments, *Int. J. Wildland Fire* 33. https://doi.org/10.1071/WF23200.

Wickstrom U (1994) The Plate Thermometer – A Simple instrument for reaching harmonized resistance tests, *Fire Technology,* 30(2), 209-231. https://doi.org/10.1007/BF01040002

Appendix A. Photos of Test Specimens Before, During, and After Testing

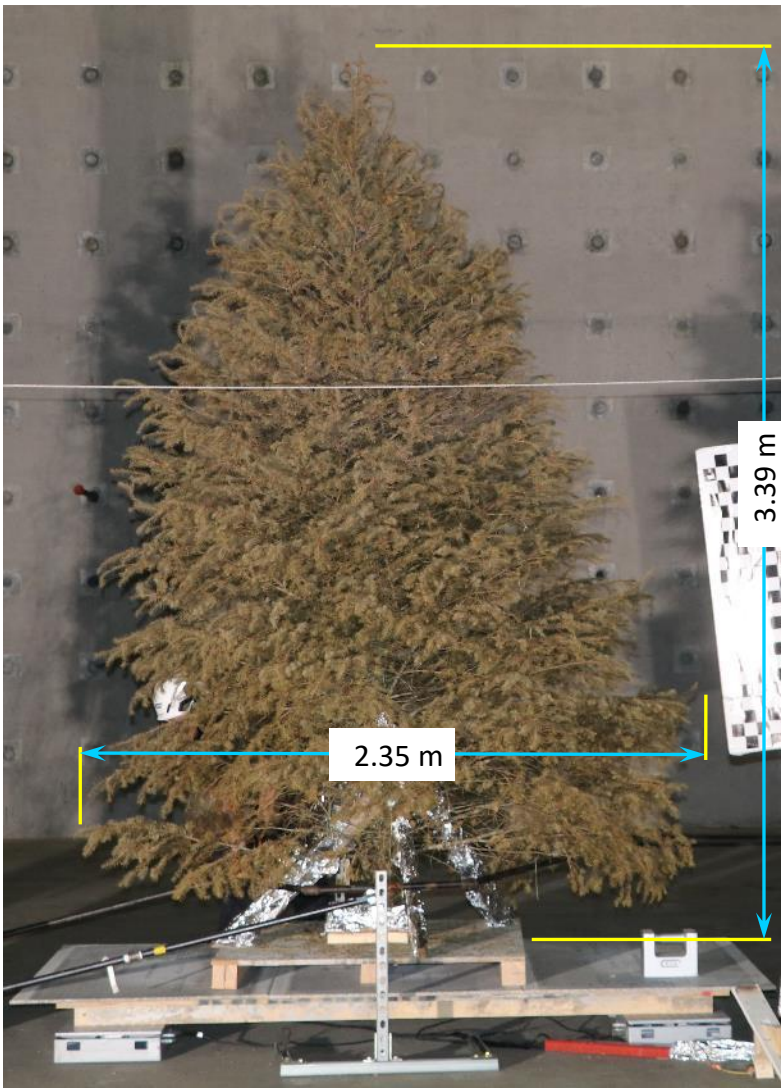

Figure A 1. Test 1 photo with dimensions of Tree 1.

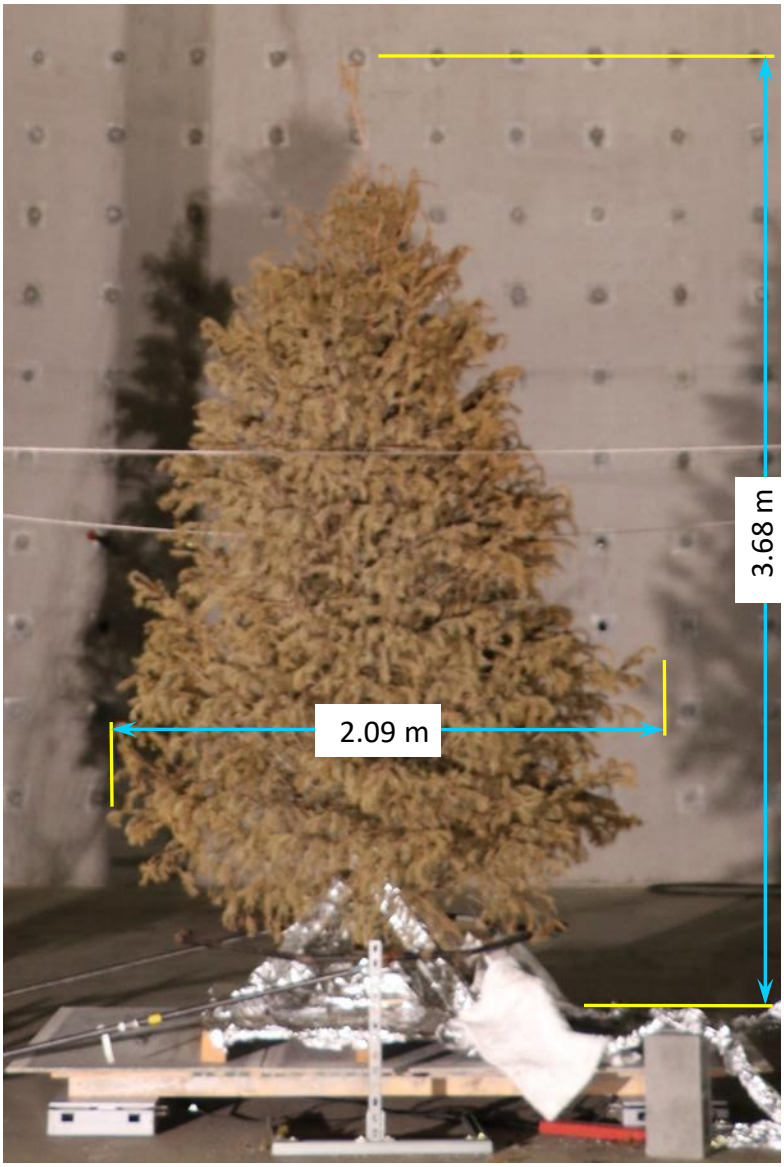

Figure A 2. Test 2 photo with dimensions of Tree 2.

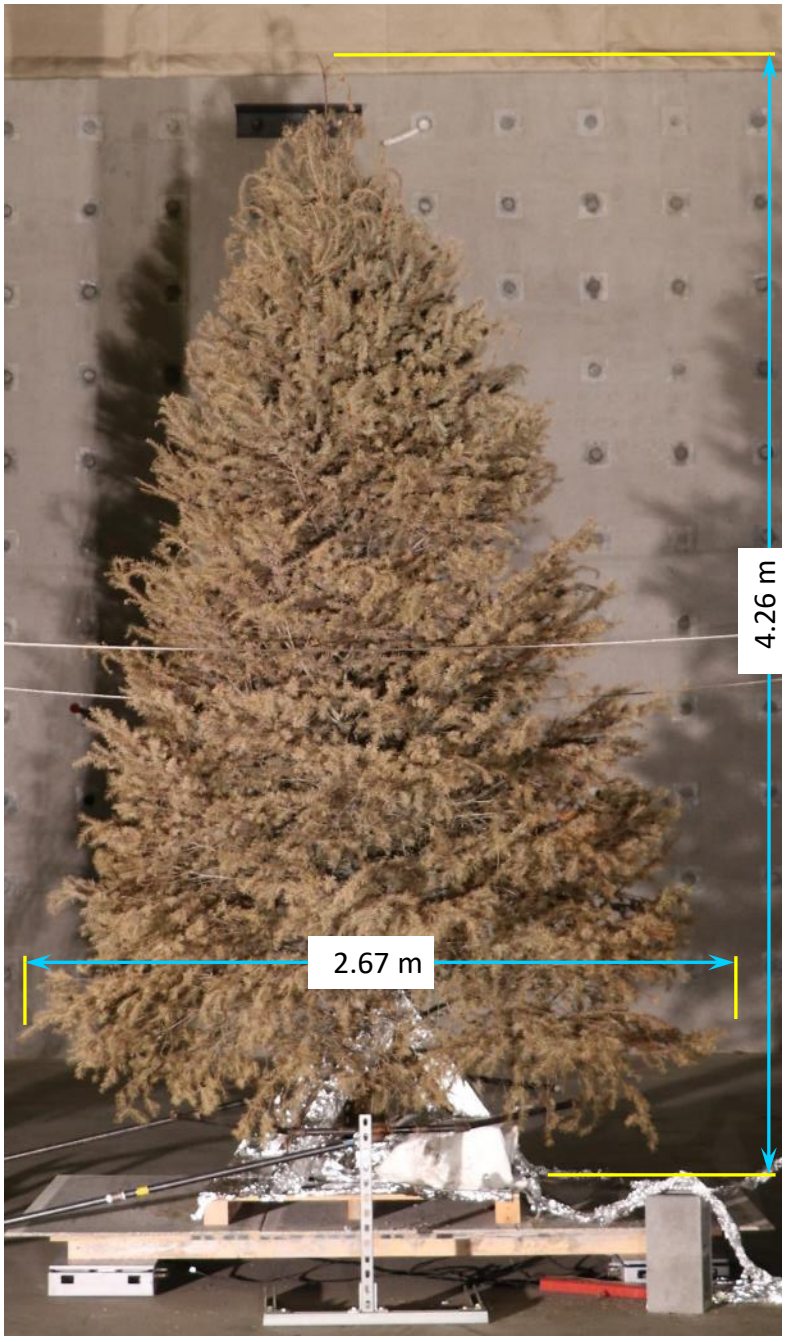

Figure A 3. Test 3 photo with dimensions of Tree 3.

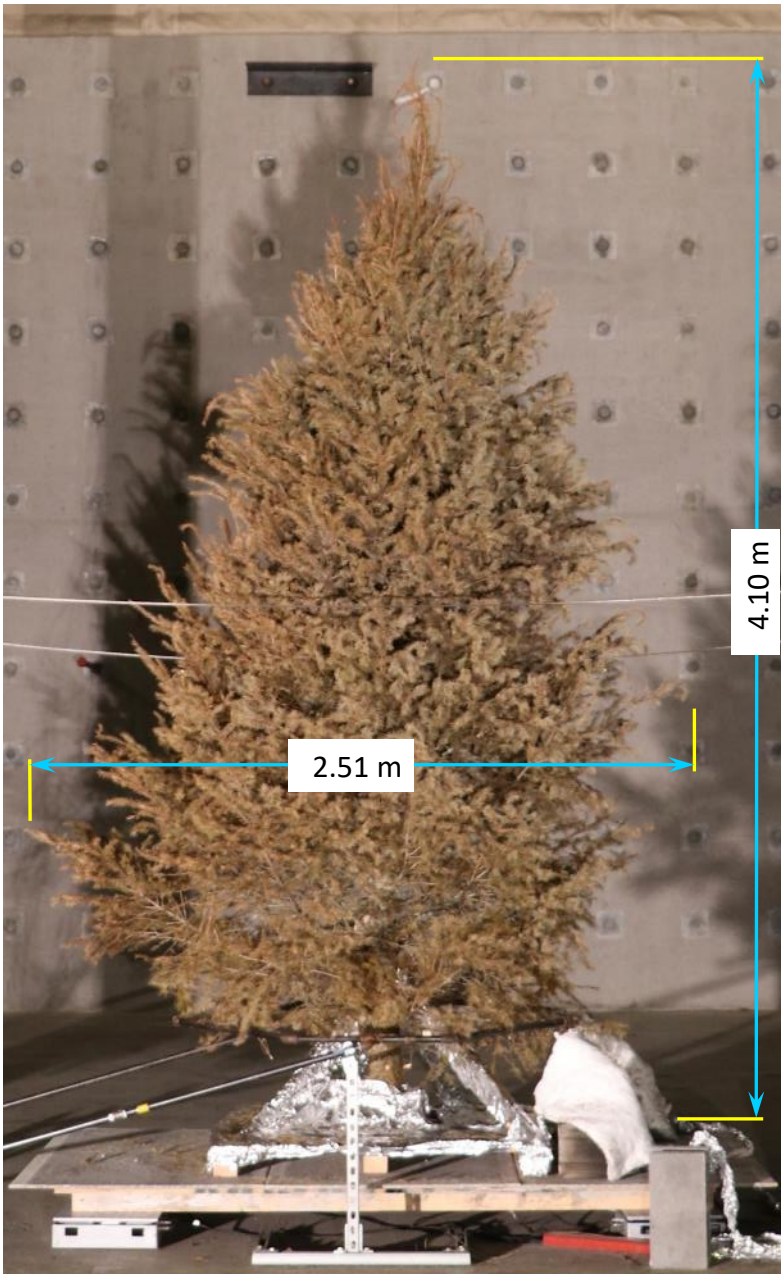

Figure A 4. Test 4 photo with dimensions of Tree 4.

Figure A 5. Test 5 photo with dimensions of Tree 5.

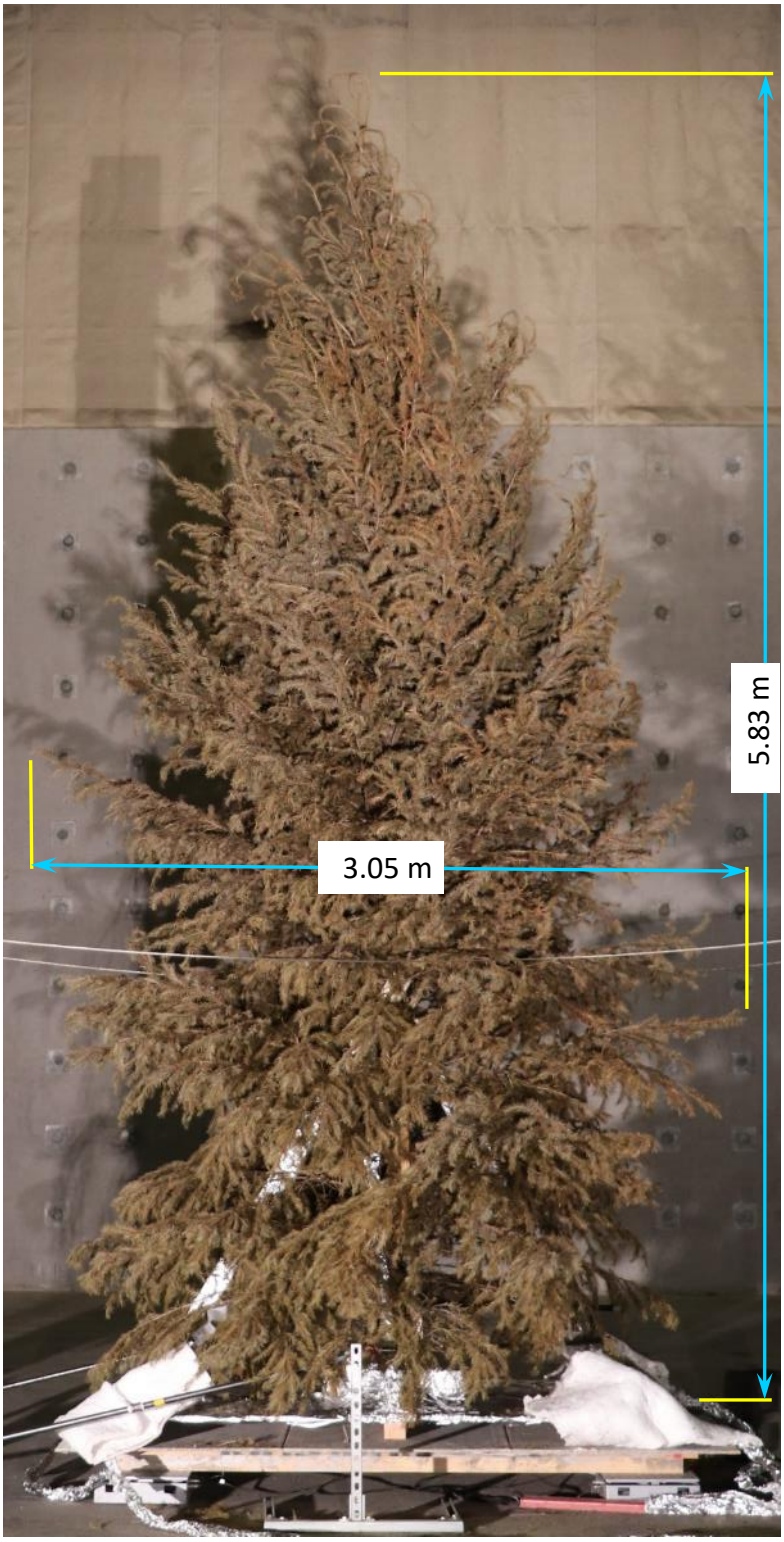

Figure A 6. Test 6 photo with dimensions of Tree 6.

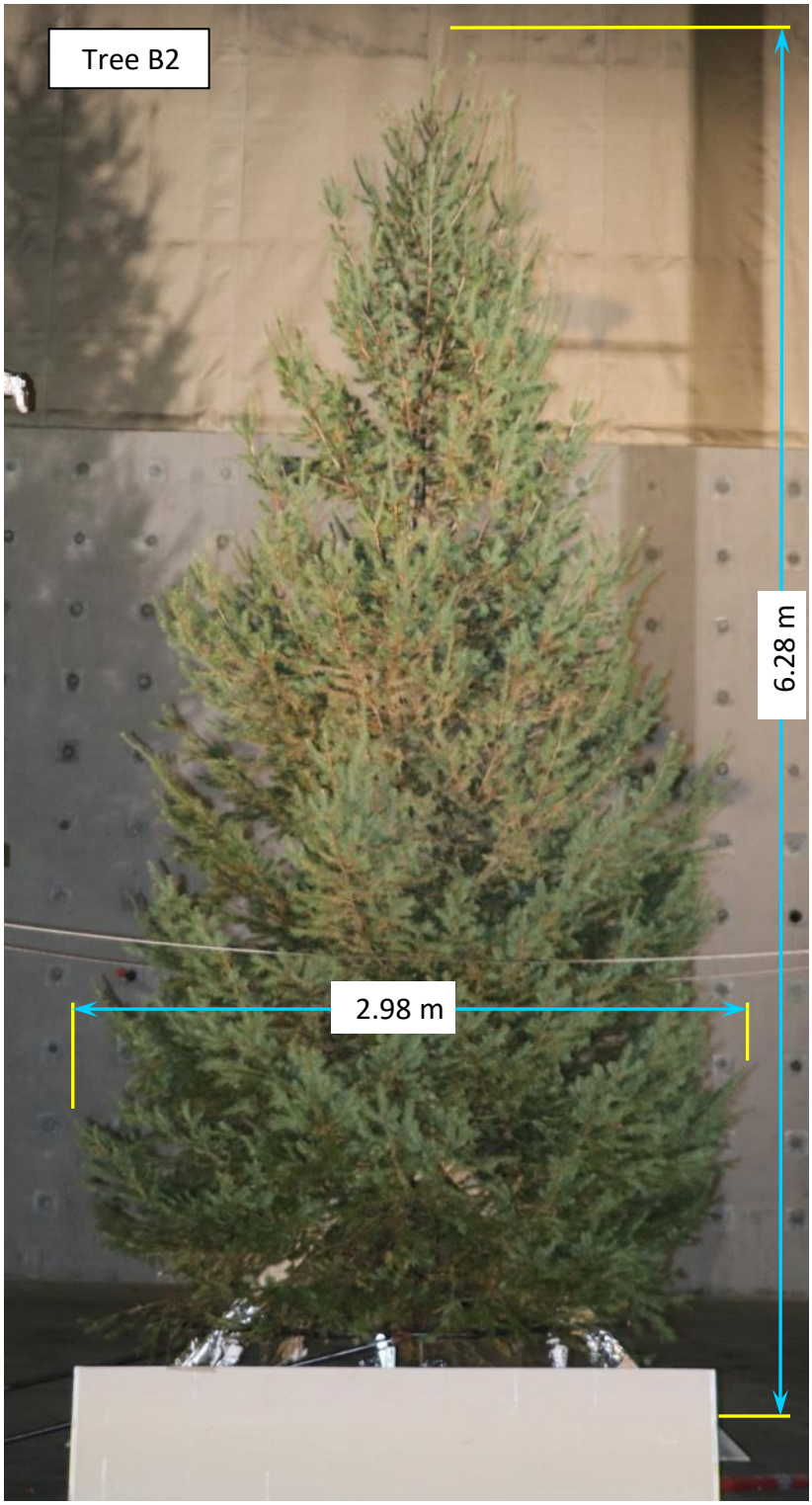

Figure A 7. Test 7 photo with dimensions of Tree 7.

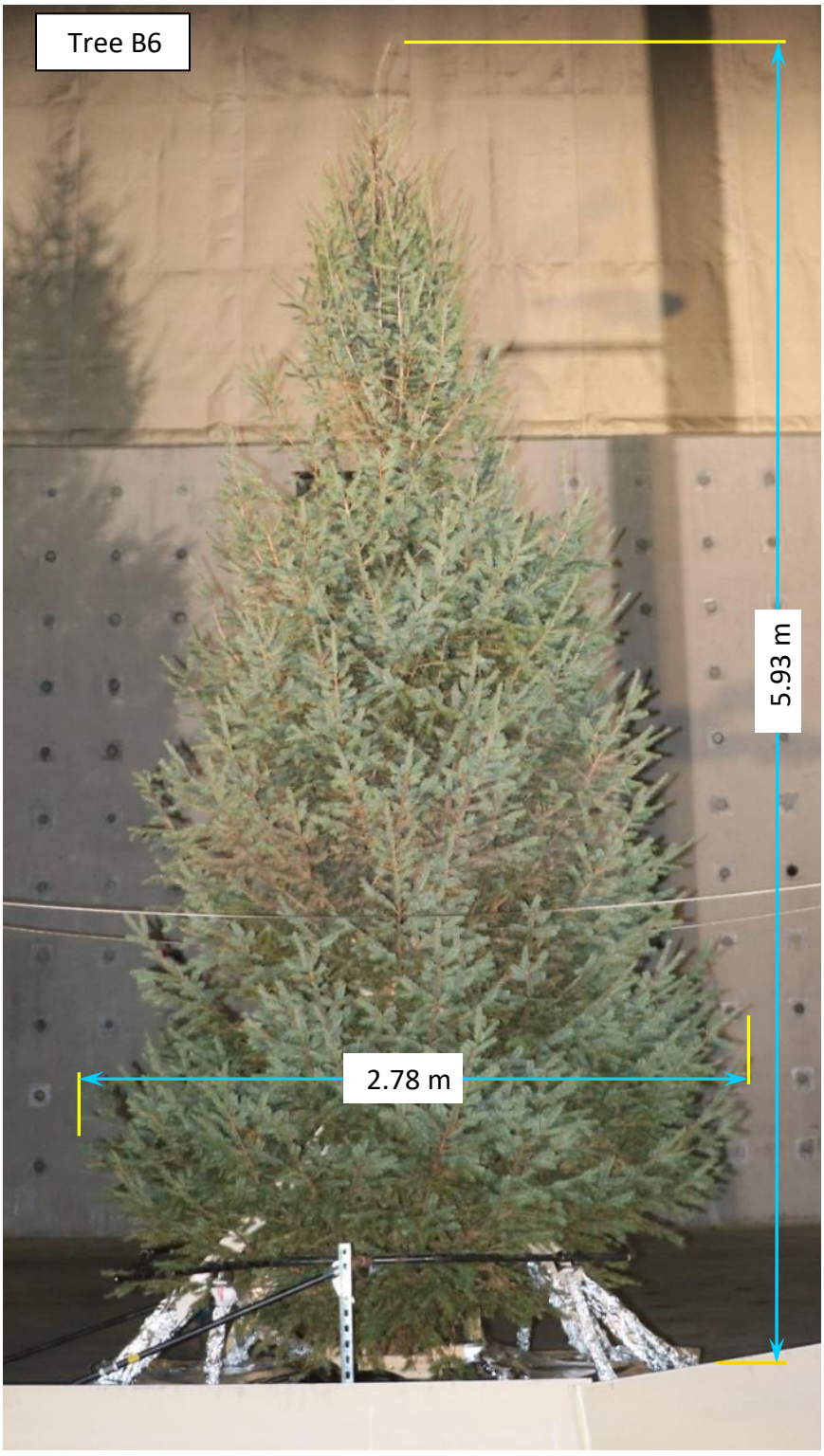

Figure A 8. Test 8 photo with dimensions of Tree 8.

Figure A 9. Test 9 photo with dimensions of Tree 9.

Figure A 10. Test 10 photo with dimensions of Tree 10.

Figure A 11. Test 11 photo with dimensions of Tree 11.

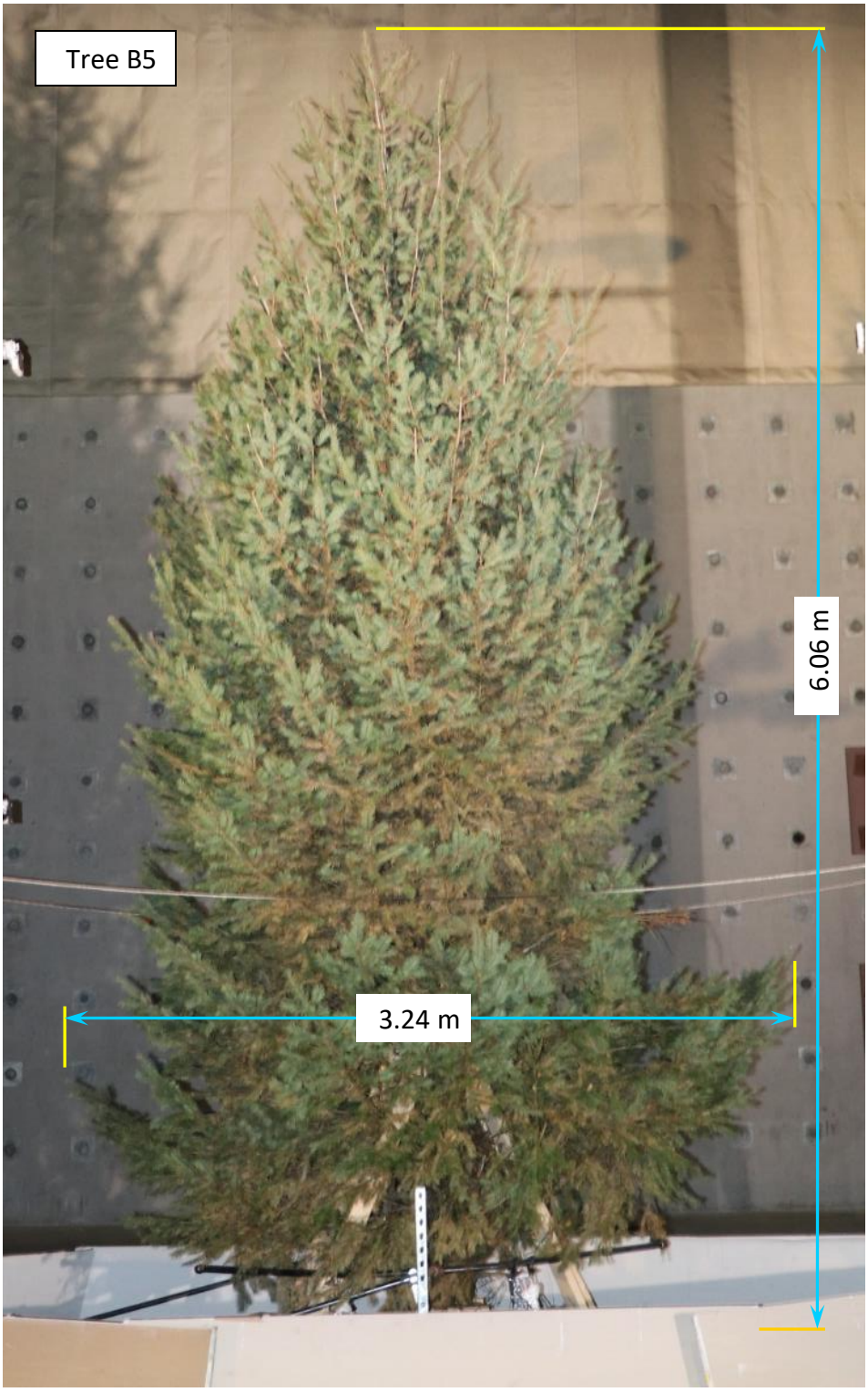

Figure A 12. Test 12 photo with dimensions of Tree 12.

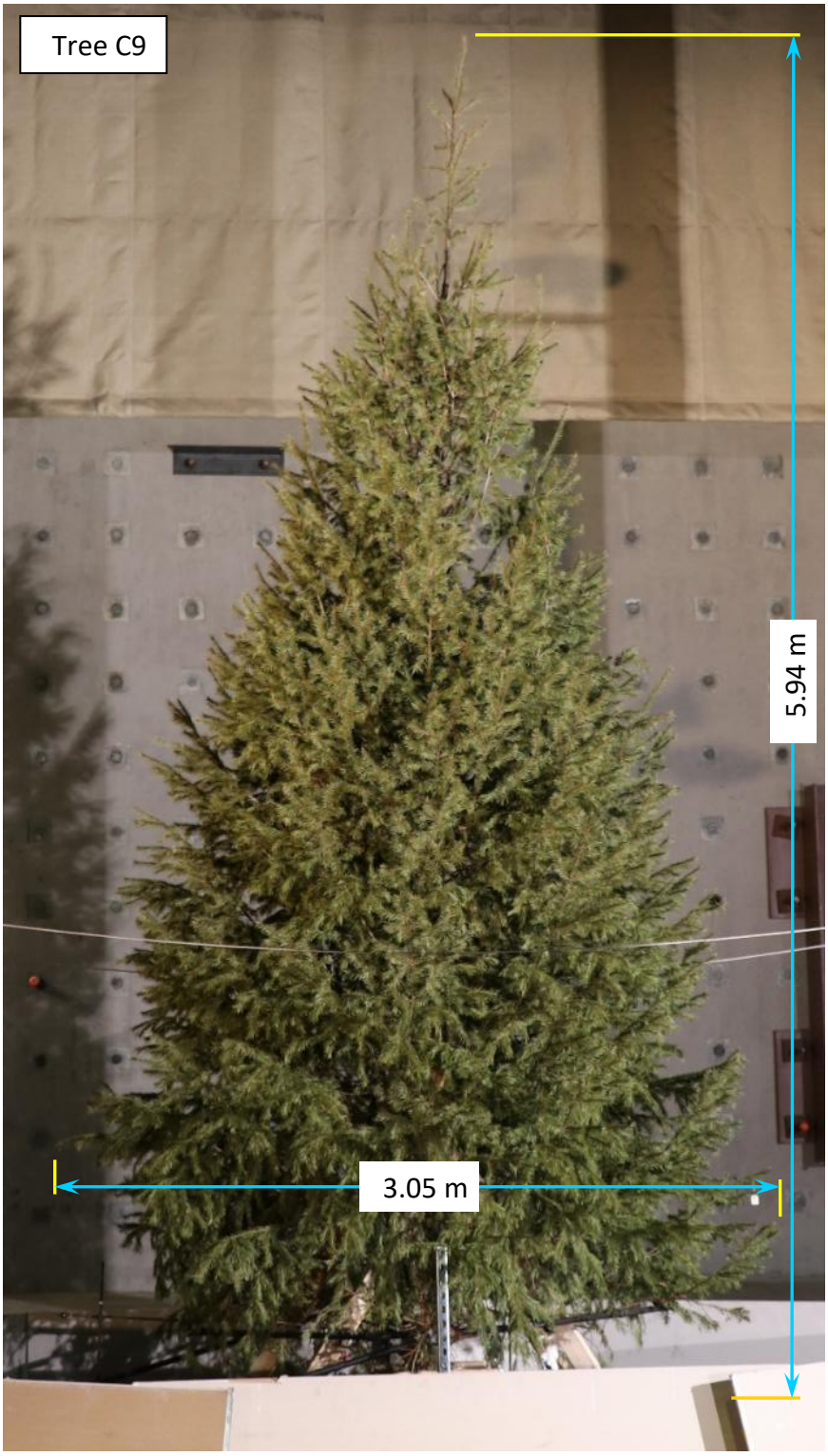

Figure A 13. Test 13 photo with dimensions of Tree 13.

Figure A 14. Test 14 photo with dimensions of Tree 14.

Figure A 15. Test 15 photo with dimensions of Tree 15.

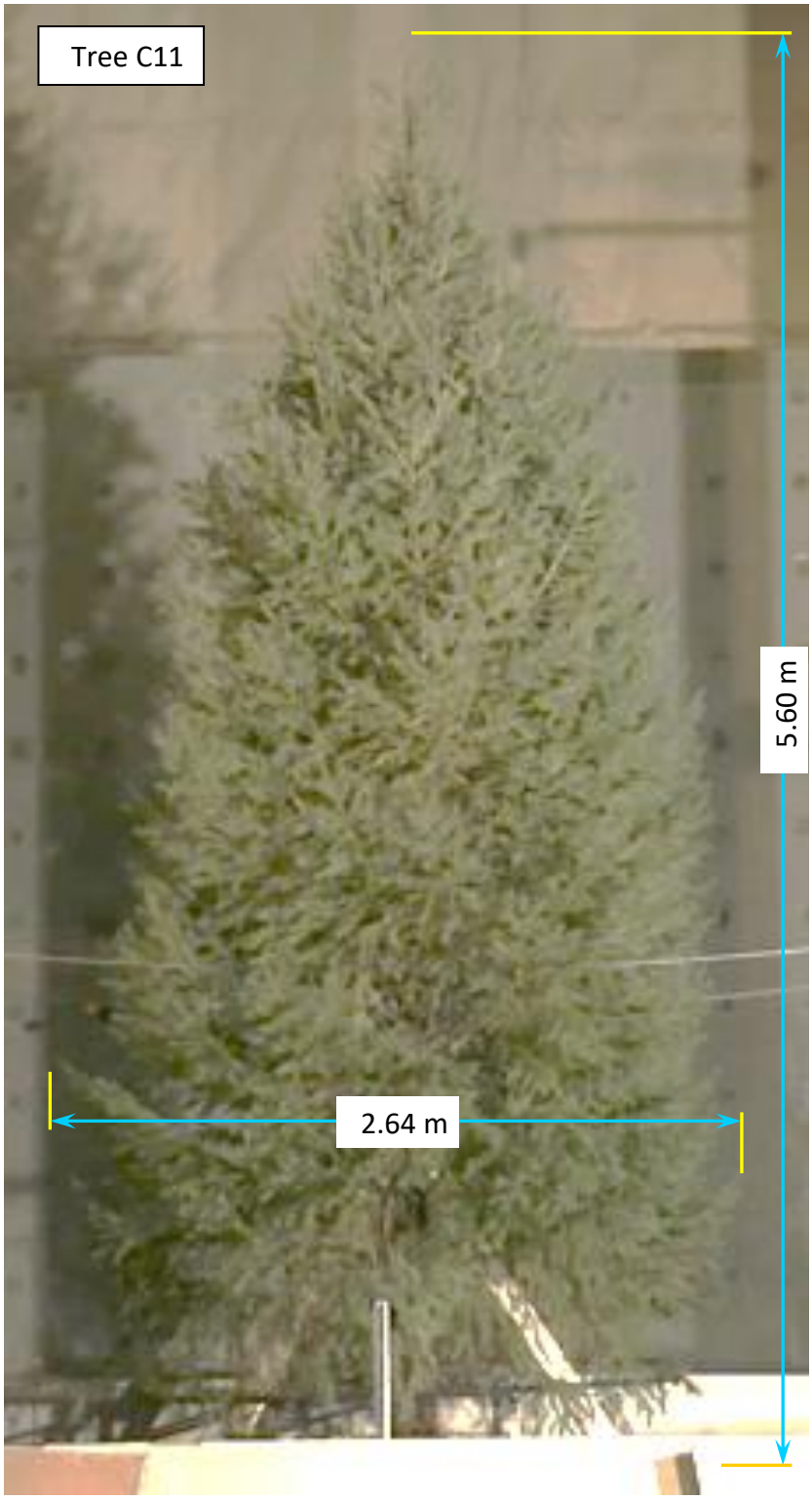

Figure A 16. Test 16 photo with dimensions of Tree 16.

Figure A 17. Test 17 photo with dimensions of Tree 17.

Figure A 18. Test 18 photo with dimensions of Tree 18.

Figure A 19. Tree 1 during and after the test.

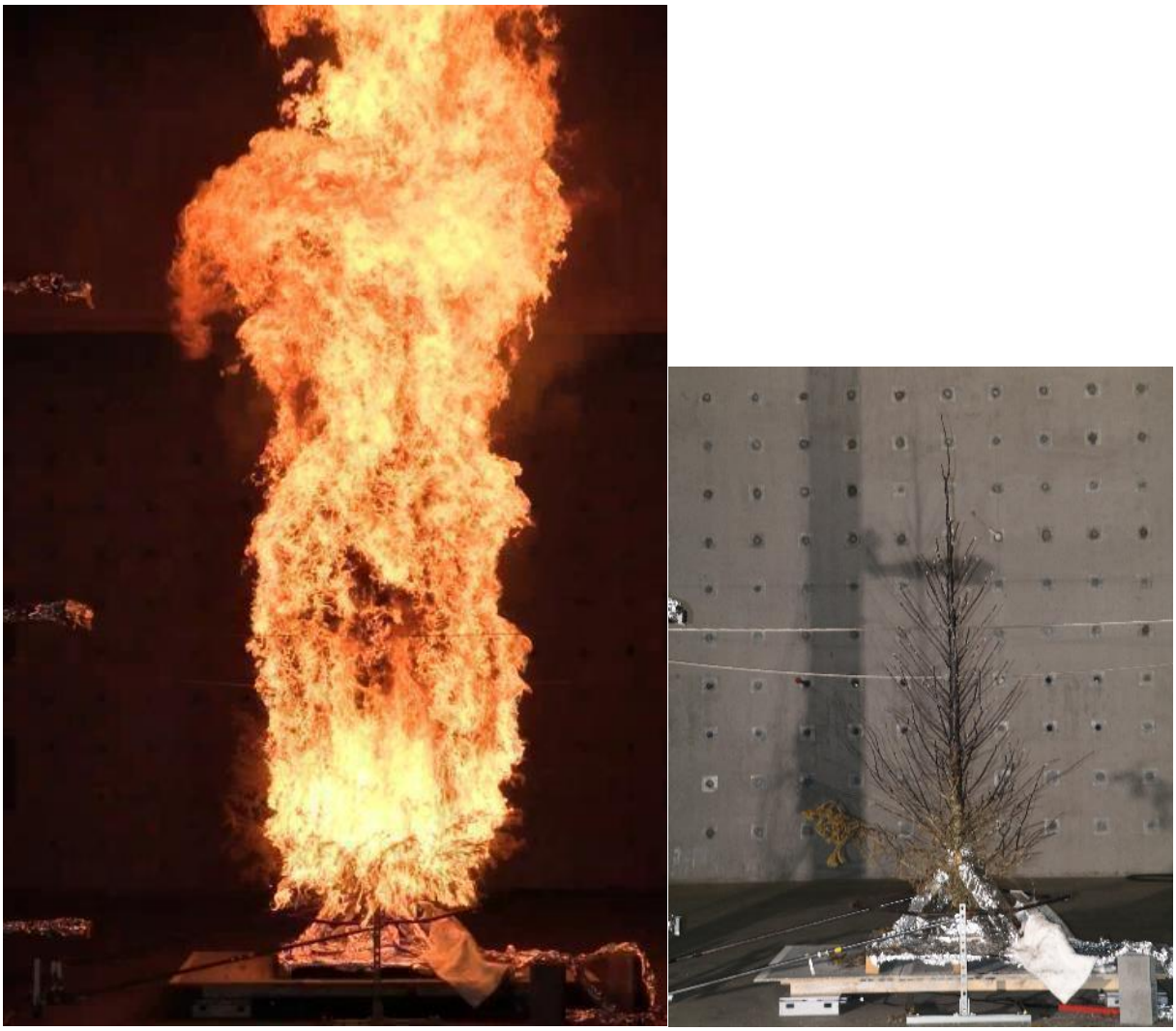

Figure A 20. Tree 2 during and after the test.

Figure A 21. Tree 3 during and after the test.

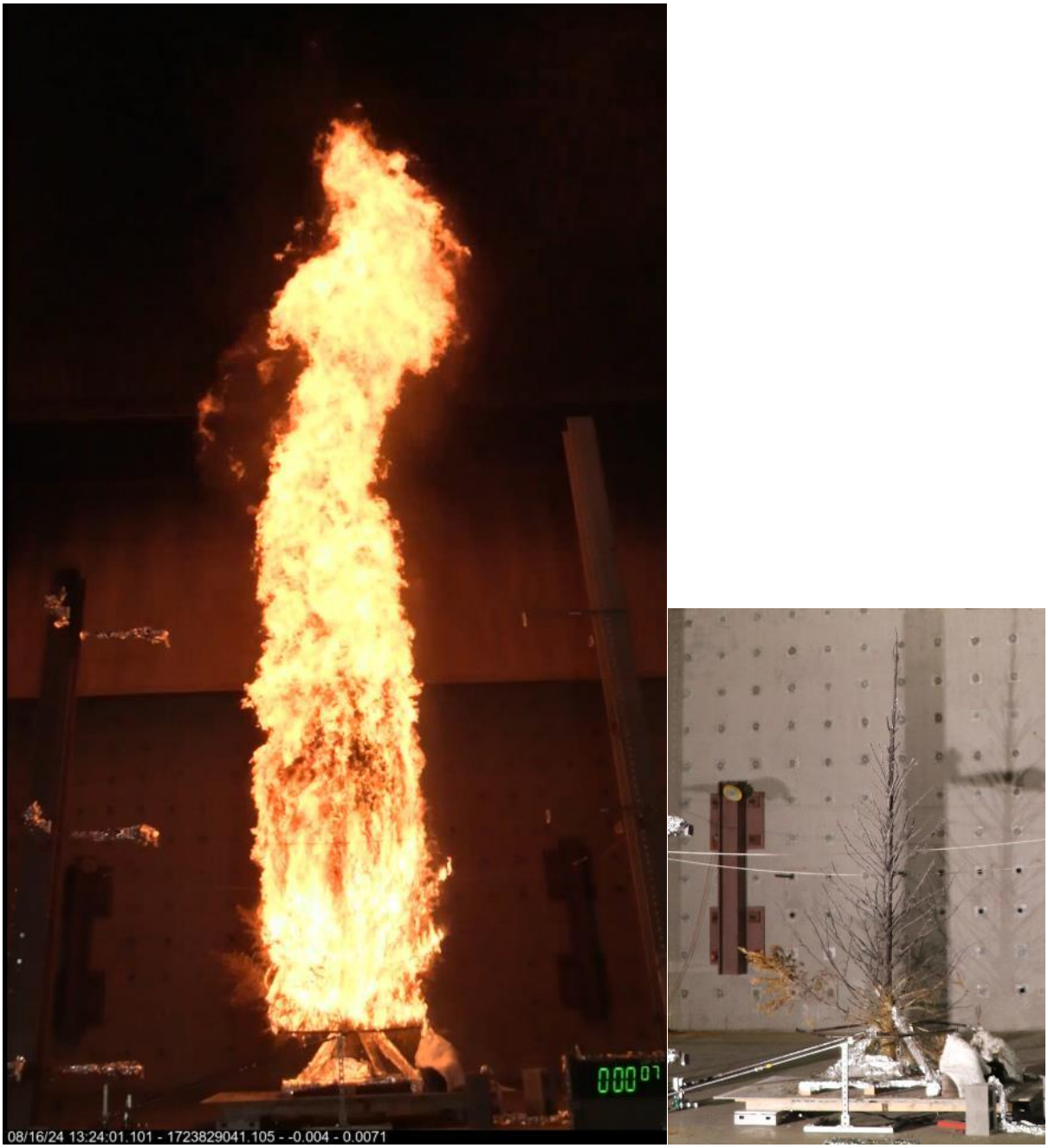

Figure A 22. Tree 4 during and after the test.

Figure A 23. Tree 5 during and after the test.

Figure A 24. Tree 6 during and after the test.

Figure A 25. Tree 7 during and after the test.

Figure A 26. Tree 8 during and after the test.

Figure A 27. Tree 9 during and after the test.

Figure A 28. Tree 10 during and after the test.

Figure A 29. Tree 11 during and after the test.

Figure A 30. Tree 12 during and after the test.

Figure A 31. Tree 13 during and after the test.

Figure A 32. Tree 14 during and after the test.

Figure A 33. Tree 15 during and after the test.

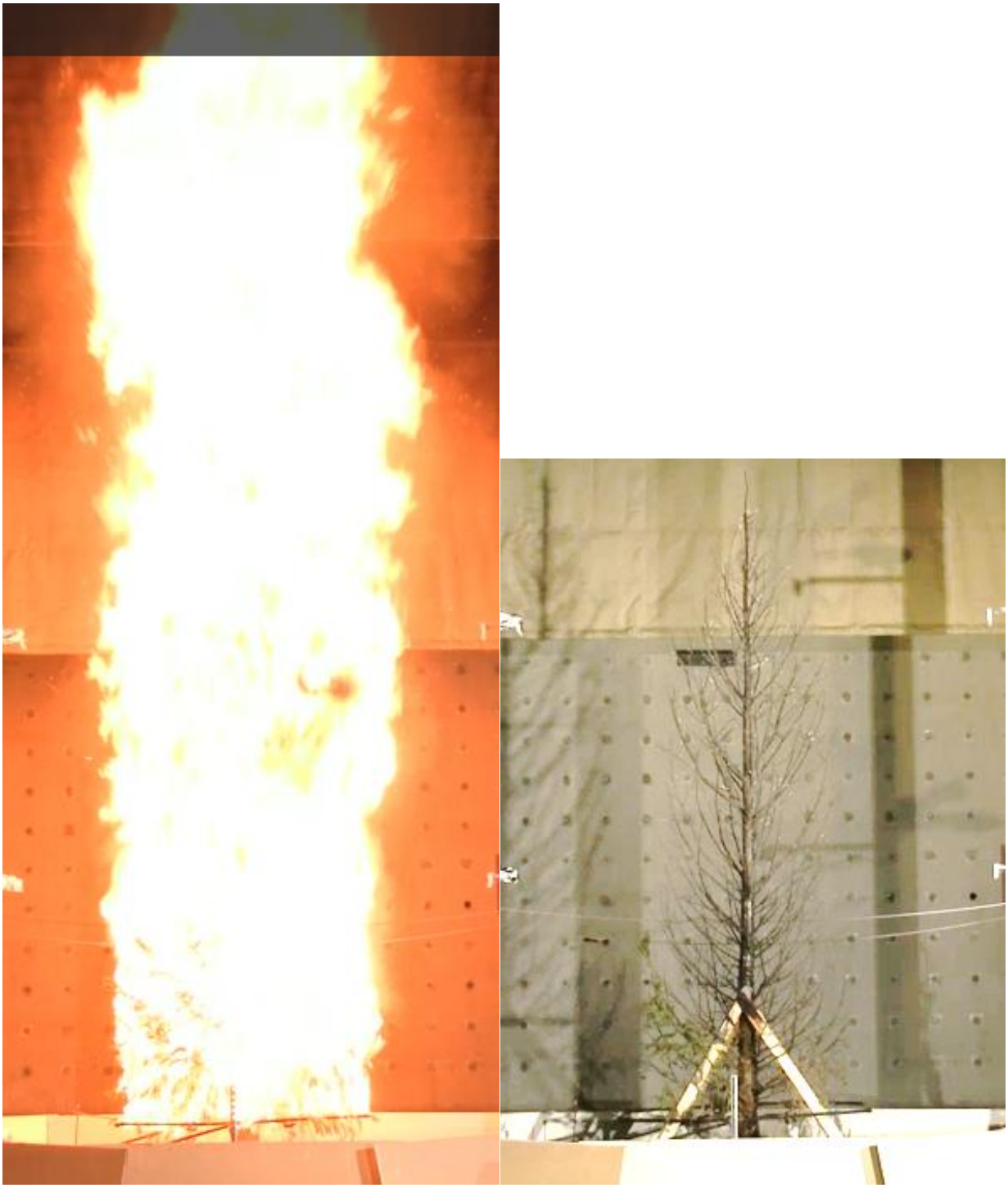

Figure A 34. Tree 16 during and after the test.

Figure A 35. Tree 17 during and after the test.

Figure A 36. Tree 18 during and after the test.

Appendix B. Calorimetry

Due to electrical signal interference from the spark igniters, the voltage signal from the load cell was unreliable for a portion of the trees. When the sparkers were turned on, a non-physical increase in the mass was observed. As the tree burned, the signal exhibited large fluctuations and instabilities. For reasons of data quality, the results of the time-resolved heat release rate derived from the mass loss rate for Trees 8 to 12 are omitted from this appendix.

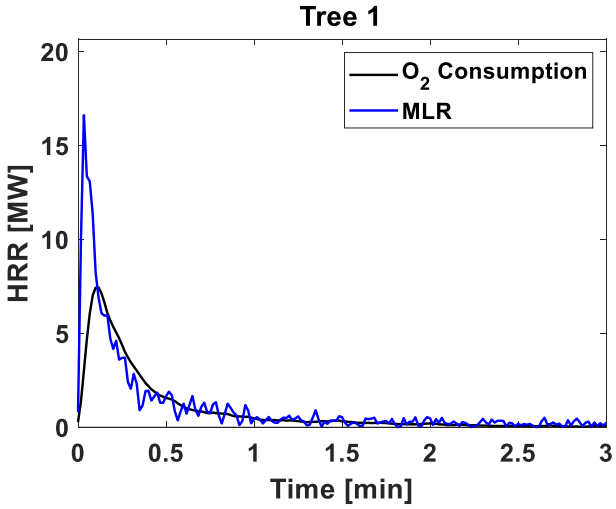

Figure B1. The heat Release rate measurement using oxygen consumption calorimetry (in black) and the mass loss rate (MLR) calorimetry (in blue) for Tree 1. The MLR trace is based on the measured transient mass loss profile seen in Appendix C.

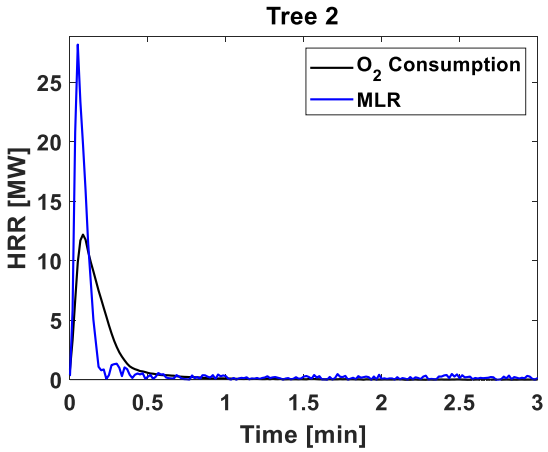

Figure B 2. The heat Release Rate measurement using oxygen consumption calorimetry (in black) and the mass loss rate (MLR) calorimetry (in blue) for Tree 2. The MLR trace is based on the measured transient mass loss profile seen in Appendix C.

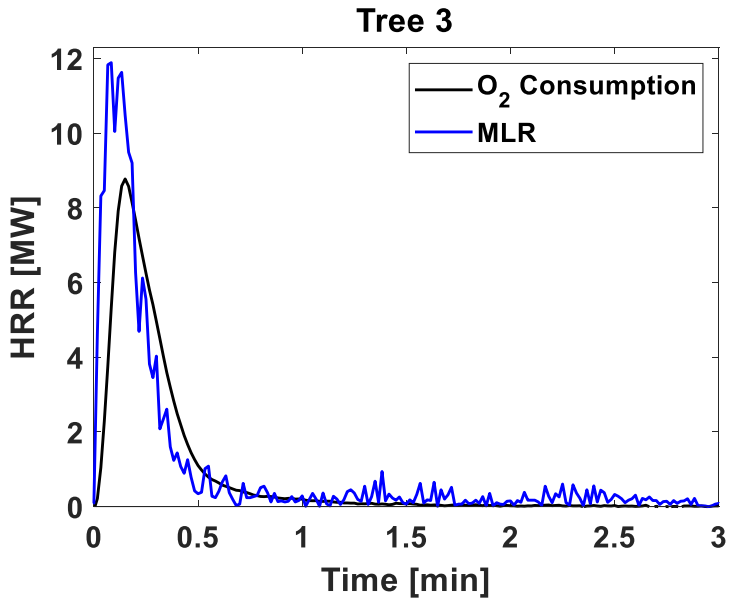

Figure B 3. The heat release rate measurement using oxygen consumption calorimetry (in black) and the mass loss rate (MLR) calorimetry (in blue) for Tree 3. The MLR trace is based on the measured transient mass loss profile seen in Appendix C.

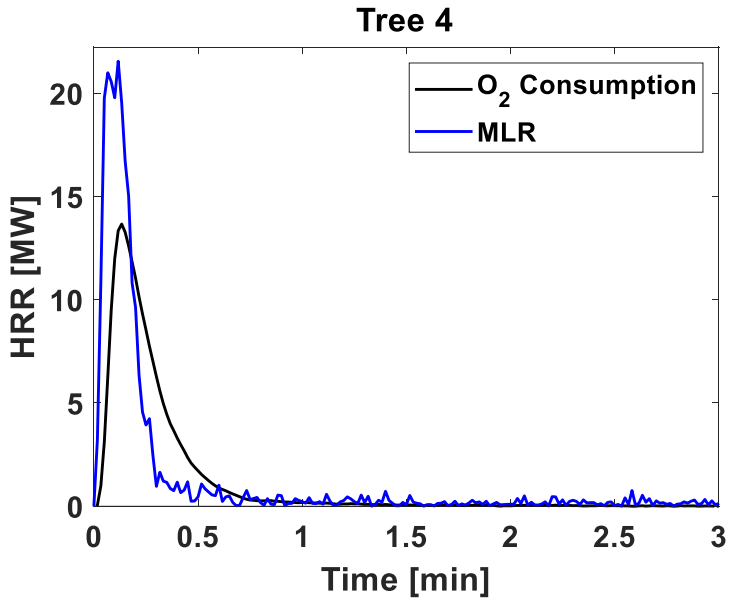

Figure B 4. The heat release rate measurement using oxygen consumption calorimetry (in black) and the mass loss rate (MLR) calorimetry (in blue) for Tree 4. The MLR trace is based on the measured transient mass loss profile seen in Appendix C.

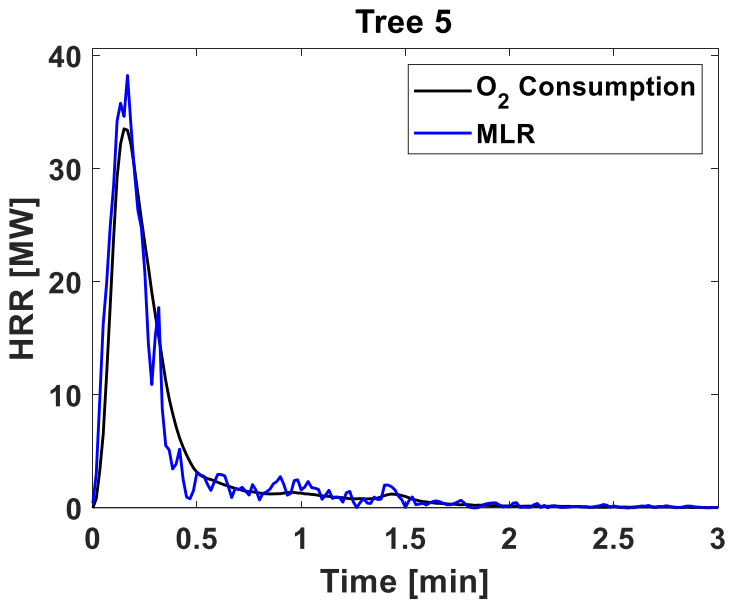

Figure B 5. The heat release rate measurement using oxygen consumption calorimetry (in black) and the mass loss rate (MLR) calorimetry (in blue) for Tree 5. The MLR trace is based on the measured transient mass loss profile seen in Appendix C.

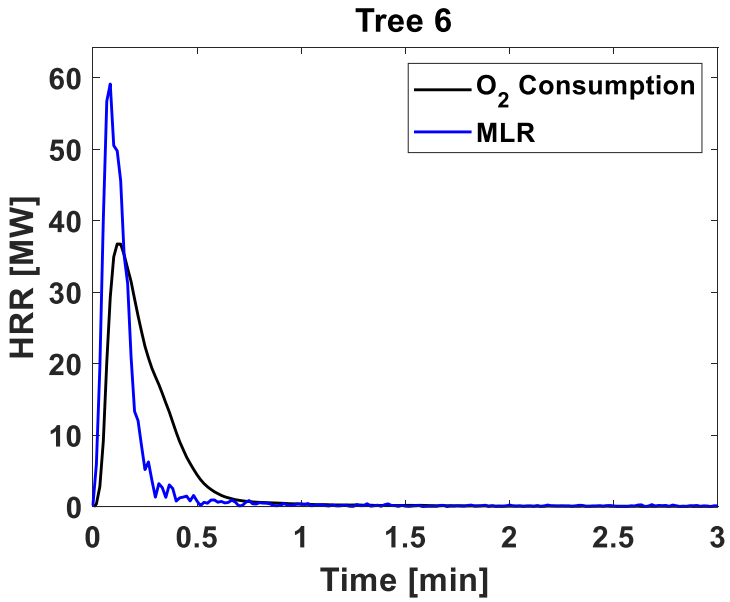

Figure B 6. The heat release rate measurement using oxygen consumption calorimetry (in black) and the mass loss rate (MLR) calorimetry (in blue) for Tree 6. The MLR trace is based on the measured transient mass loss profile seen in Appendix C.

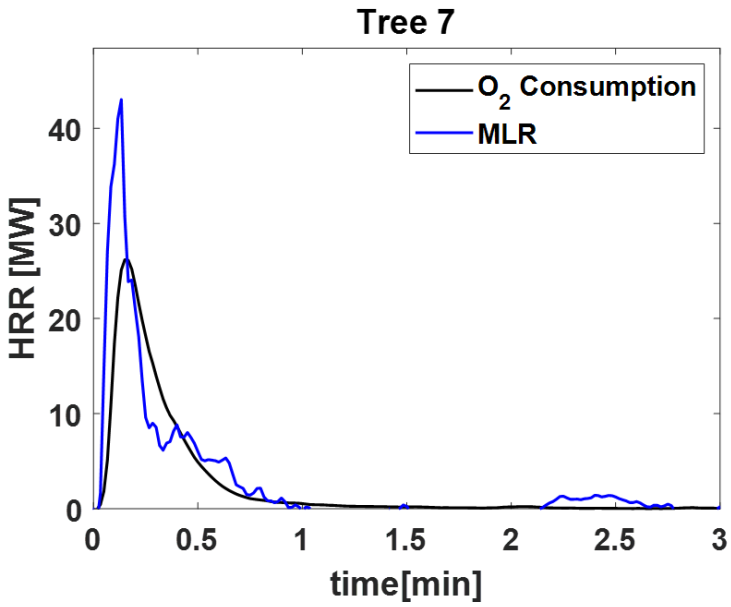

Figure B 7. The heat release rate measurement using oxygen consumption calorimetry (in black) and the mass loss rate (MLR) calorimetry (in blue) for Tree 7. The MLR trace is based on the measured transient mass loss profile seen in Appendix C.

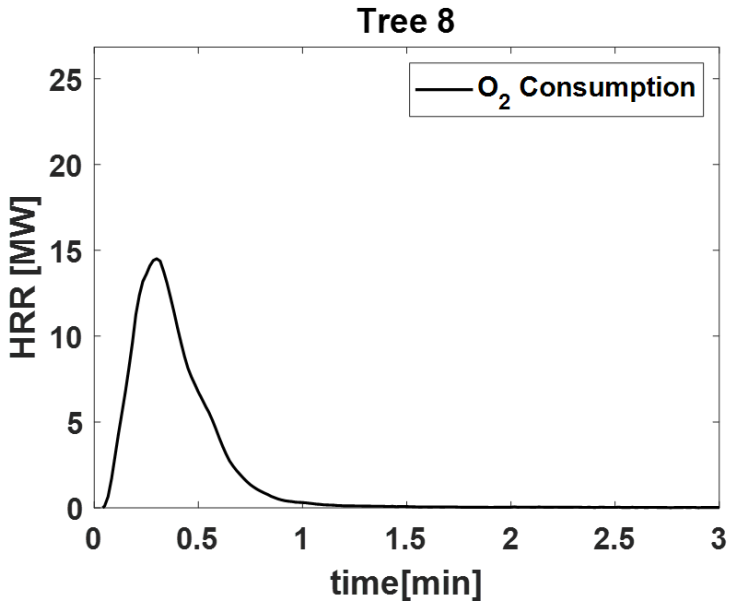

Figure B 8. The heat release rate measurement using oxygen consumption calorimetry for Tree 8. The time-resolved mass for Tree 10 is omitted (see explanation in Appendix C).

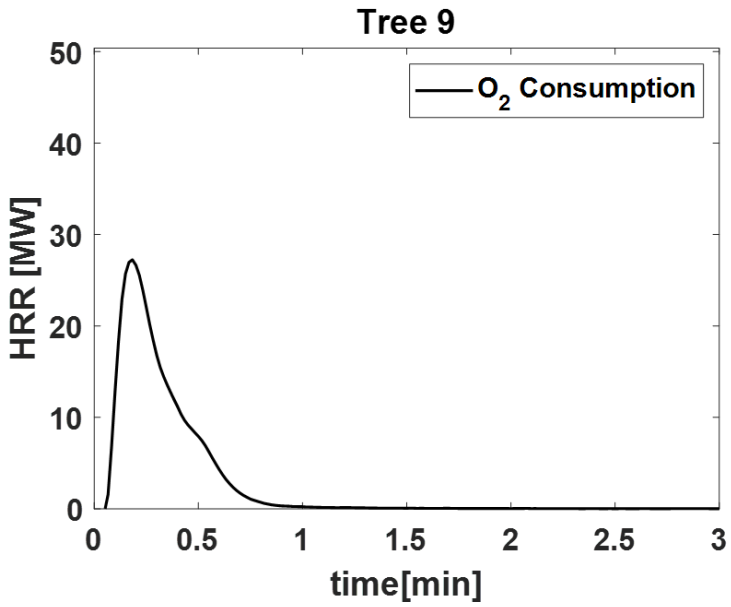

Figure B 9 The heat release rate measurement using oxygen consumption calorimetry for Tree 9. The time-resolved mass for Tree 10 is omitted (see explanation in Appendix C).

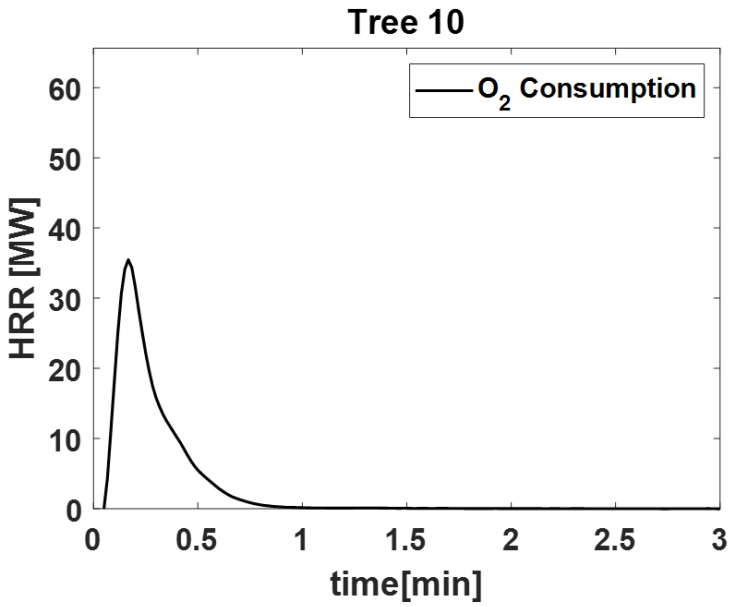

Figure B 10. The heat release rate measurement using oxygen consumption calorimetry for Tree 10. The time-resolved mass for Tree 10 is omitted (see explanation in Appendix C).

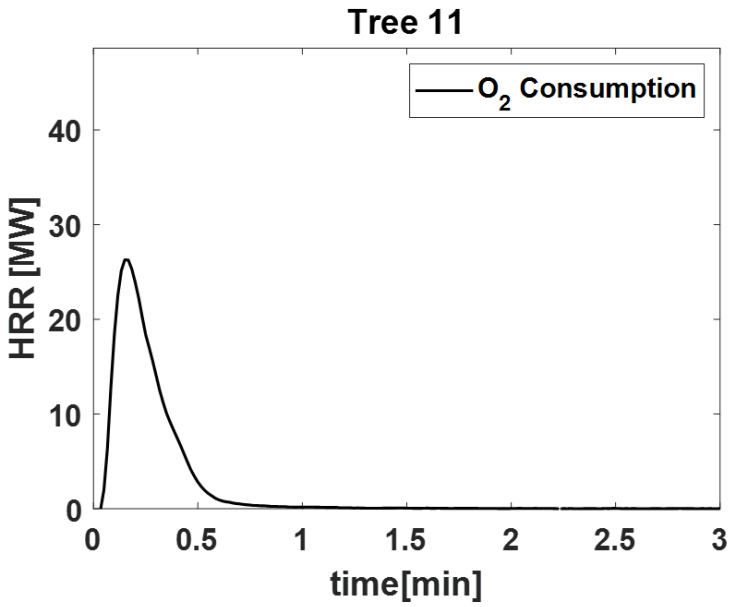

Figure B 11. The heat release rate measurement using oxygen consumption calorimetry for Tree 11. The time-resolved mass for Tree 10 is omitted (see explanation in Appendix C).

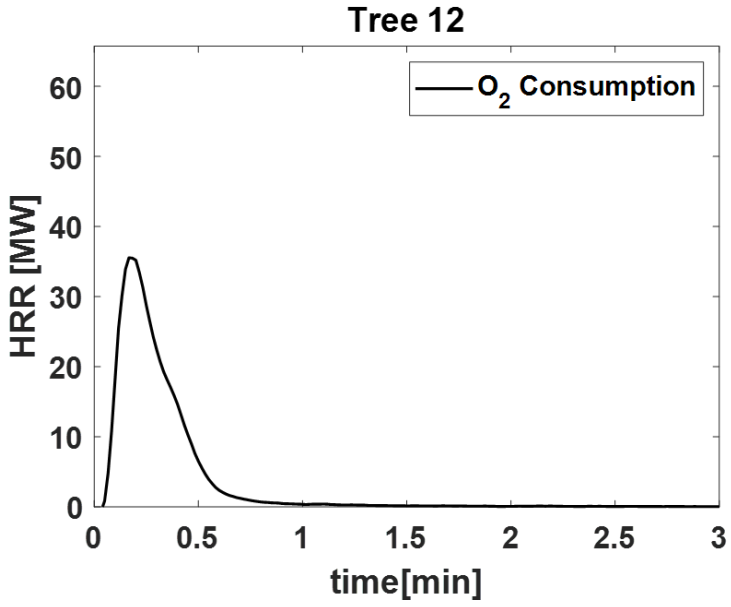

Figure B 12. The heat release rate measurement using oxygen consumption calorimetry for Tree 12. The time-resolved mass for Tree 10 is omitted (see explanation in Appendix C).

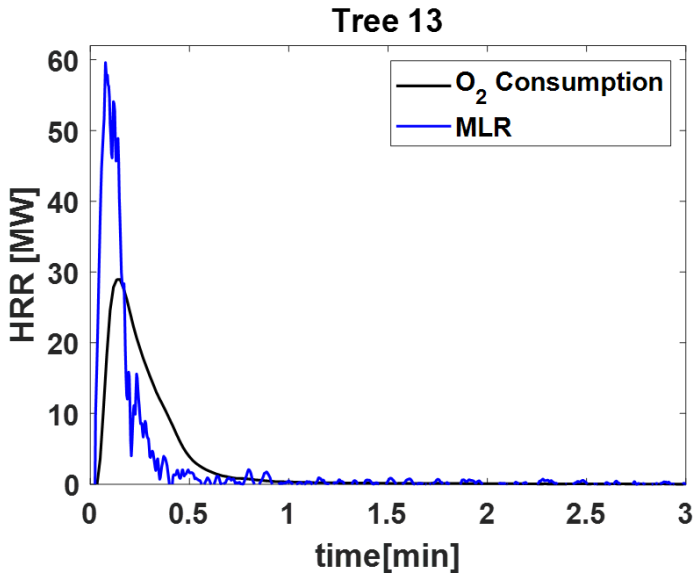

Figure B 13. The heat release rate measurement using oxygen consumption calorimetry (in black) and the mass loss rate (MLR) calorimetry (in blue) for Tree 13. The MLR trace is based on the measured transient mass loss profile seen in Appendix C.

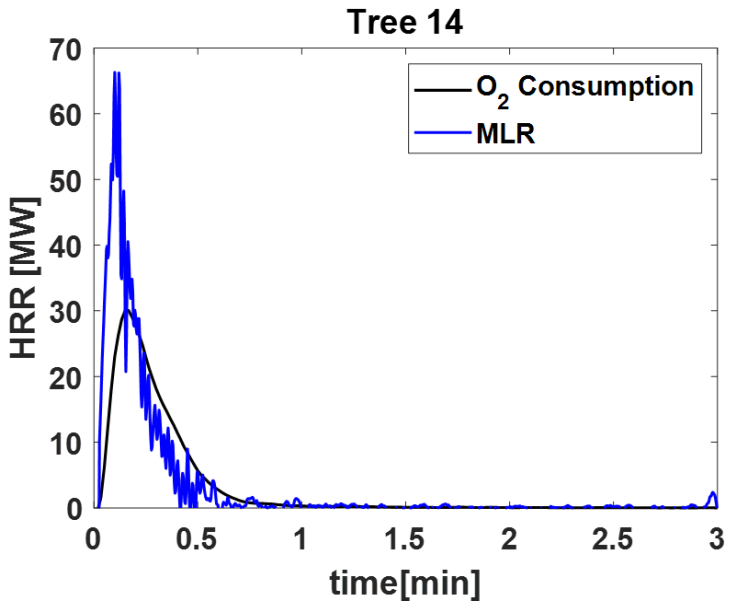

Figure B 14. The heat release rate measurement using oxygen consumption calorimetry (in black) and the mass loss rate (MLR) calorimetry (in blue) for Tree 14. The MLR trace is based on the measured transient mass loss profile seen in Appendix C.

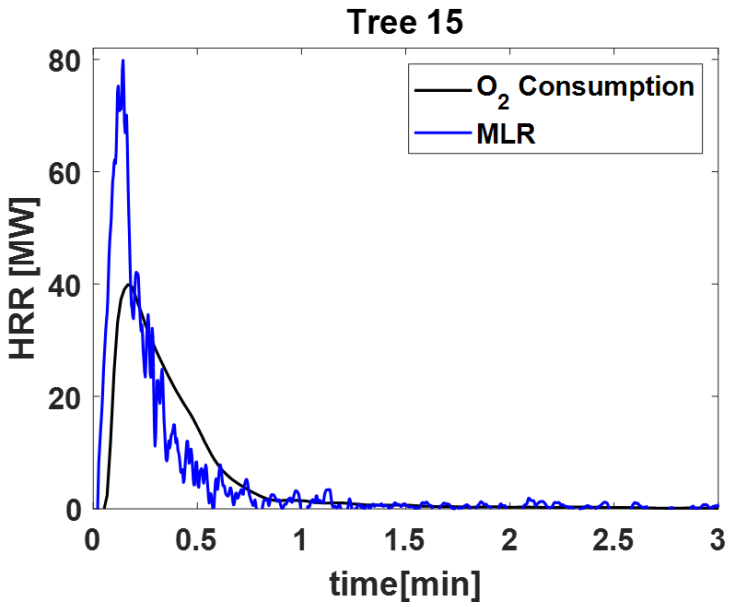

Figure B 15. The heat release rate measurement using oxygen consumption calorimetry (in black) and the mass loss rate (MLR) calorimetry (in blue) for Tree 15. The MLR trace is based on the measured transient mass loss profile seen in Appendix C.

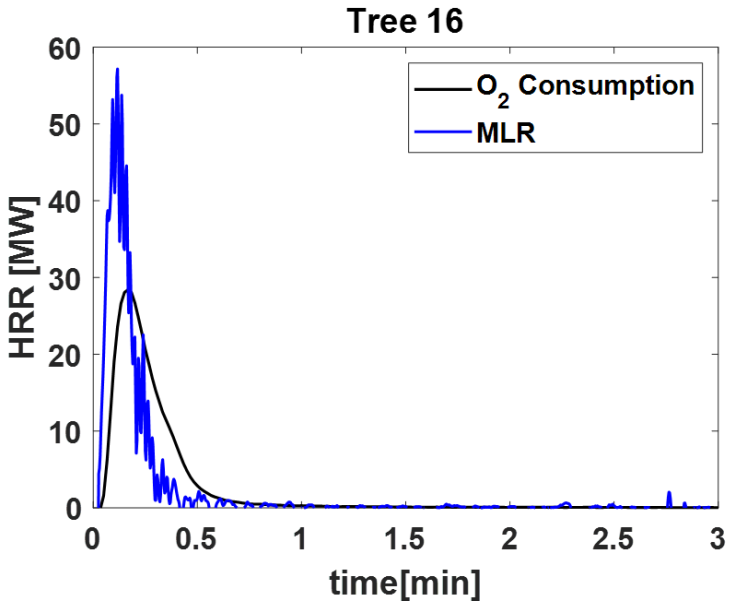

Figure B 16. The heat release rate measurement using oxygen consumption calorimetry (in black) and the mass loss rate (MLR) calorimetry (in blue) for Tree 16. The MLR trace is based on the measured transient mass loss profile seen in Appendix C.

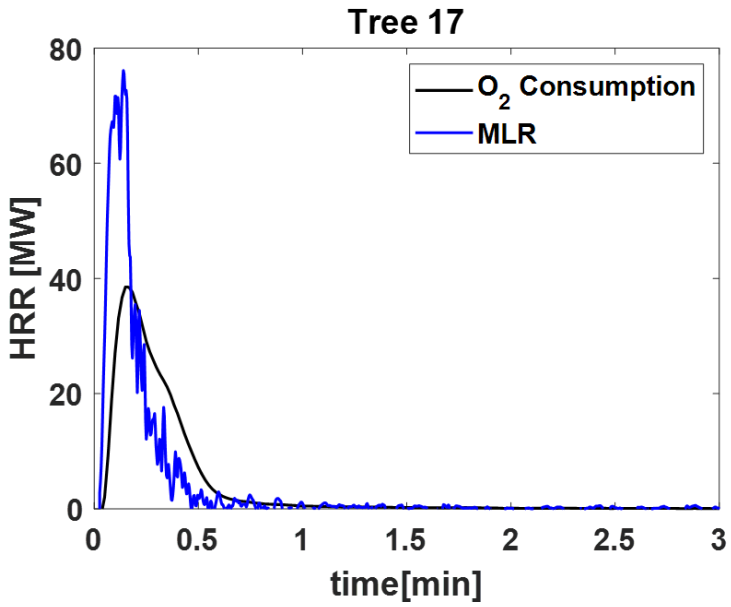

Figure B 17. The heat release rate measurement using oxygen consumption calorimetry (in black) and the mass loss rate (MLR) calorimetry (in blue) for Tree 17. The MLR trace is based on the measured transient mass loss profile seen in Appendix C.

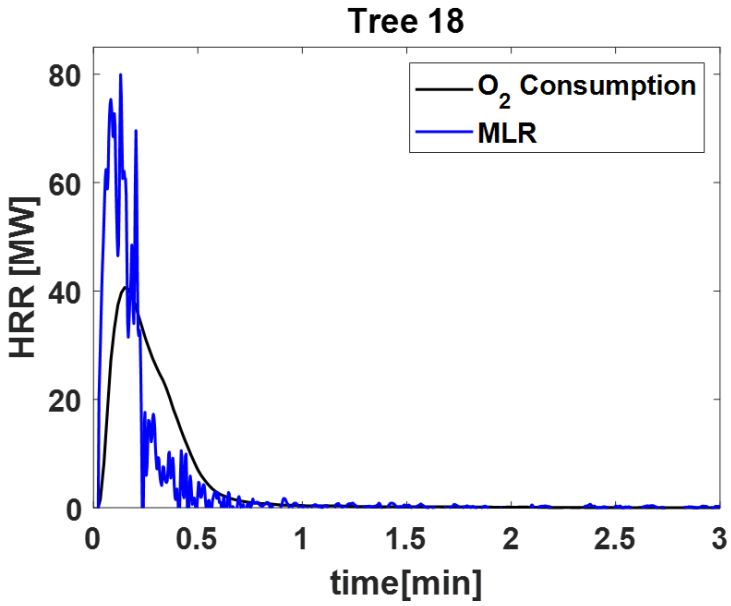

Figure B 18. The heat release rate measurement using oxygen consumption calorimetry (in black) and the mass loss rate (MLR) calorimetry (in blue) for Tree 18. The MLR trace is based on the measured transient mass loss profile seen in Appendix C.

Appendix C. Mass Loss

Due to electrical signal interference from the spark igniters, the voltage signal from the load cell was unreliable for a number of the tests. When the ignition sparkers were powered, a non-physical increase in the mass was observed. As the tree burned and the signal exhibited large fluctuations and instabilities. For reasons of data quality, the results of the time-resolved mass for Trees 8 to 12 are omitted from this appendix.

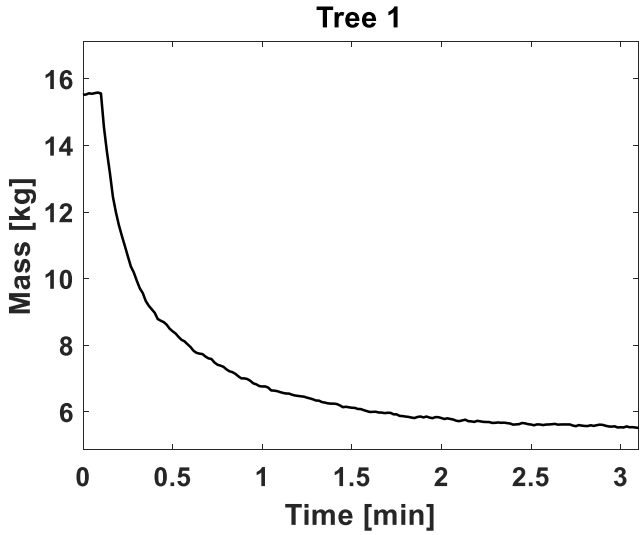

Figure C 1. Tree 1 transient load cell (wet) mass measurements with ignition at time zero.

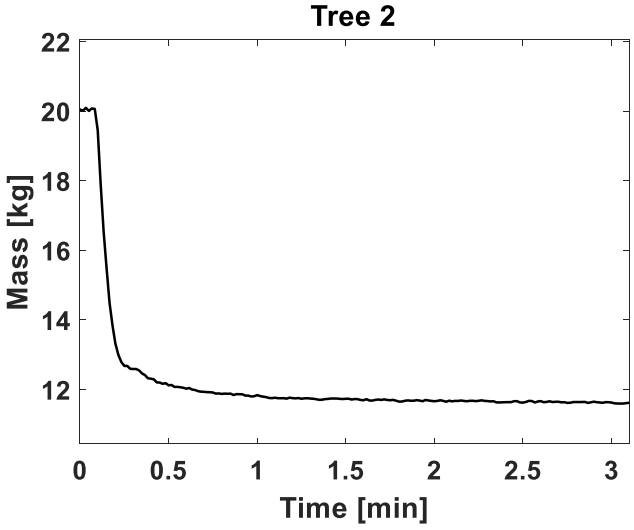

Figure C 2. Tree 2 transient load cell (wet) mass measurements with ignition at time zero.

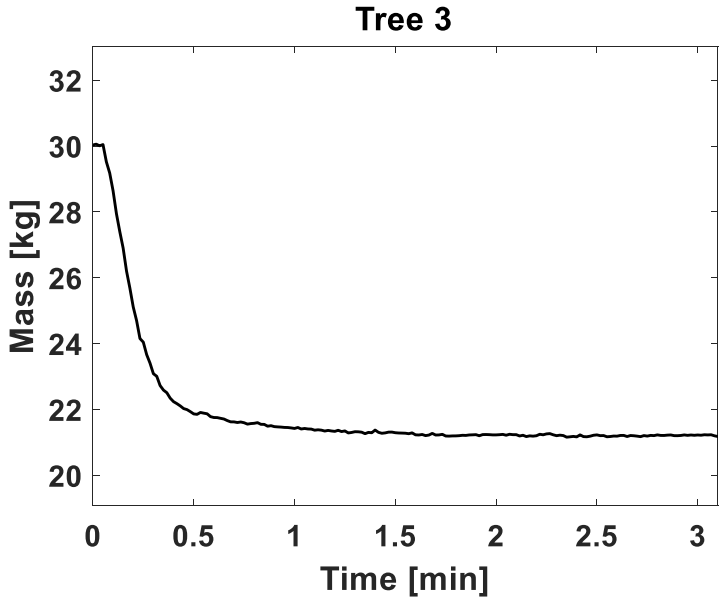

Figure C 3. Tree 3 transient load cell (wet) mass measurements with ignition at time zero.

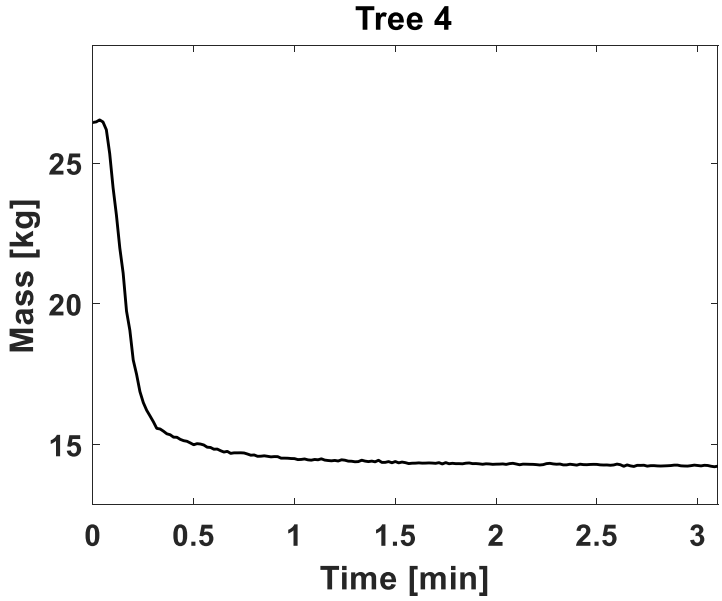

Figure C 4. Tree 4 transient load cell (wet) mass measurements with ignition at time zero.

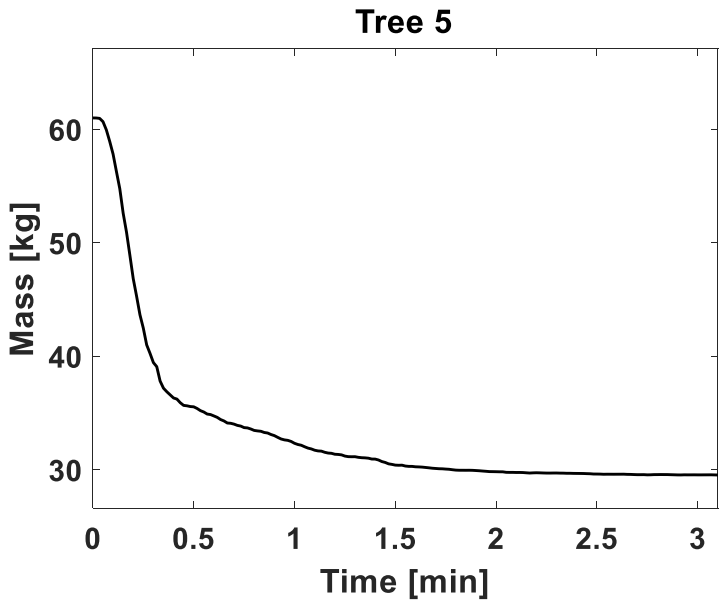

Figure C 5. Tree 5 transient load cell (wet) mass measurements with ignition at time zero.

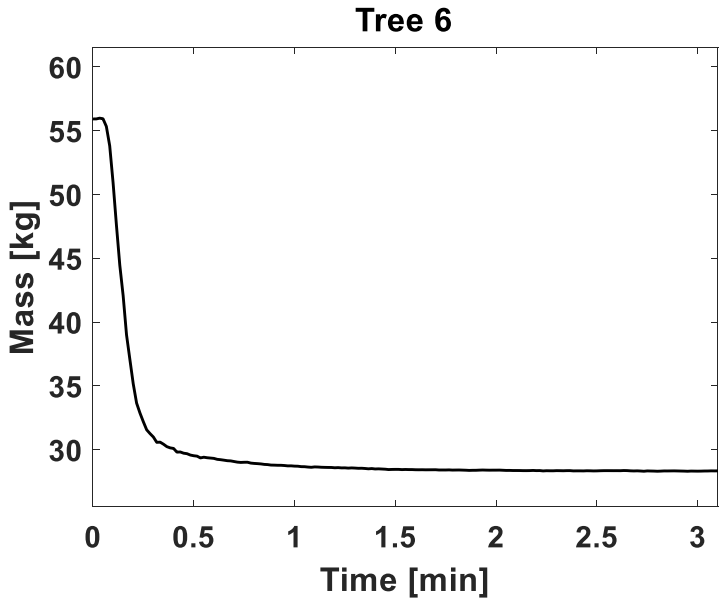

Figure C 6. Tree 6 transient load cell (wet) mass measurements with ignition at time zero.

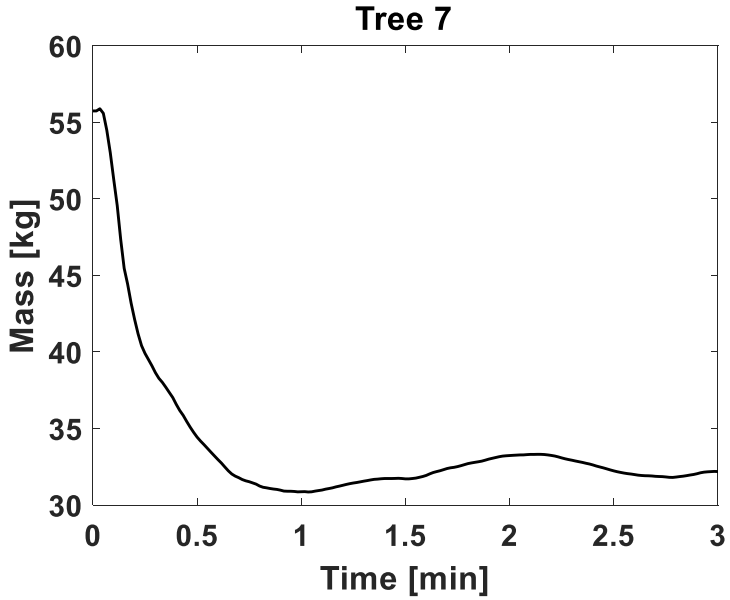

Figure C 7. Tree 7 transient load cell (wet) mass measurements with ignition at time zero.

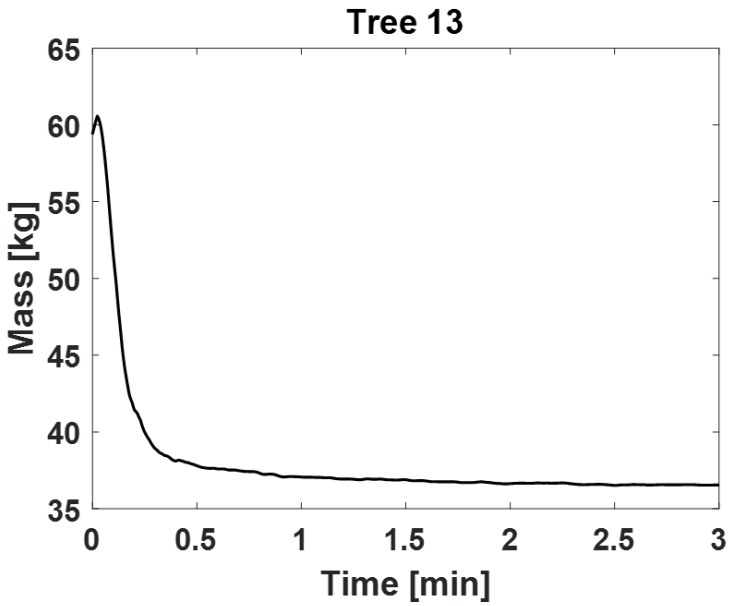

Figure C 8. Tree 13 transient load cell (wet) mass measurements with ignition at time zero.

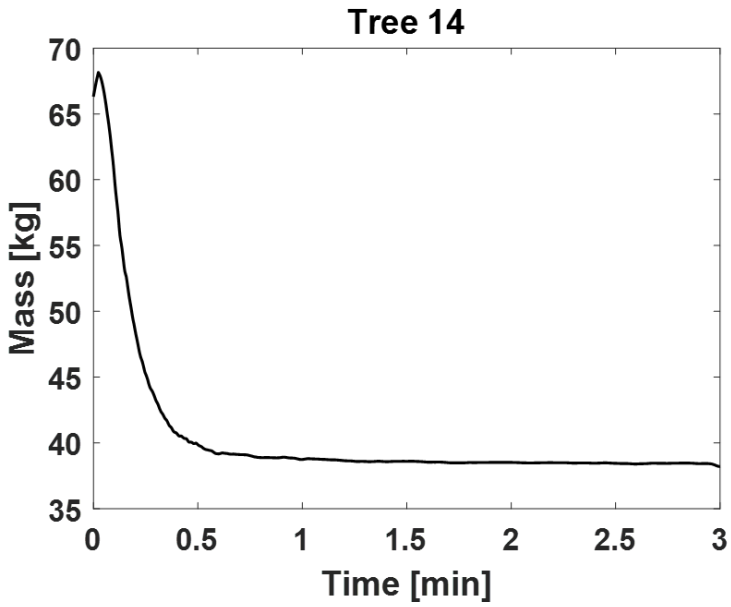

Figure C 9. Tree 14 transient load cell (wet) mass measurements with ignition at time zero.

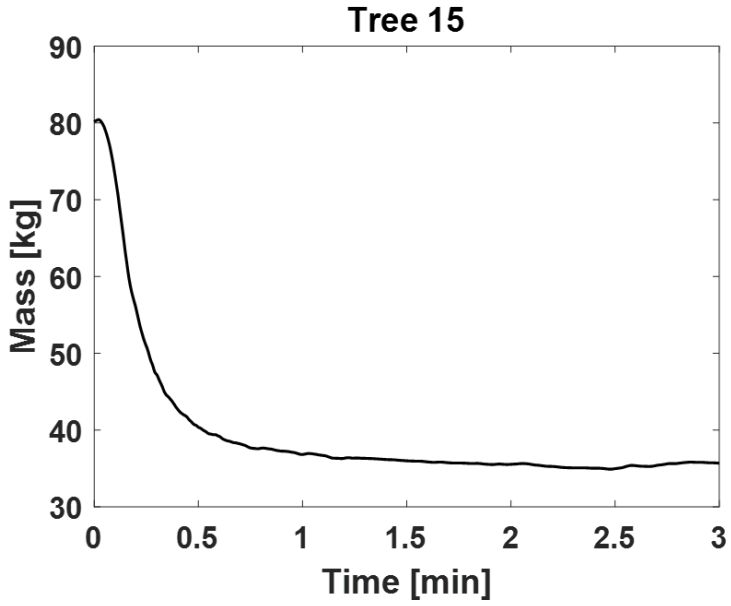

Figure C 10. Tree 15 transient load cell (wet) mass measurements with ignition at time zero.

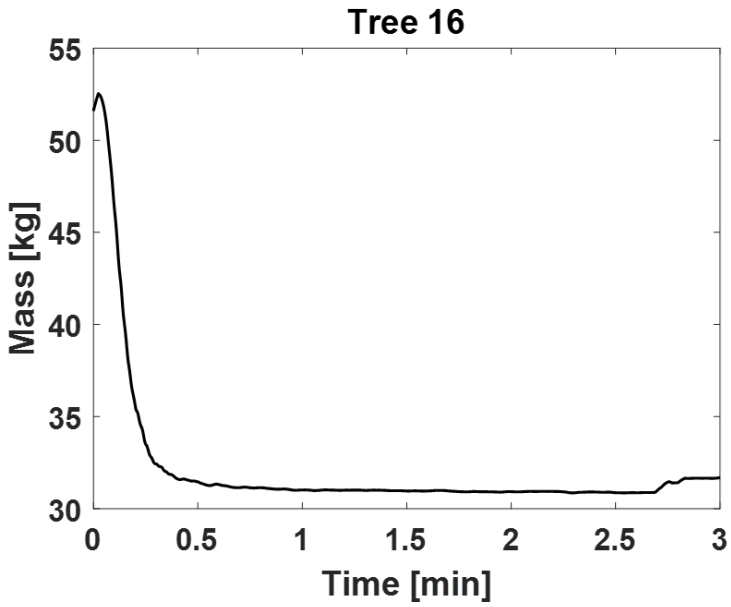

Figure C 11. Tree 16 transient load cell (wet) mass measurements with ignition at time zero.

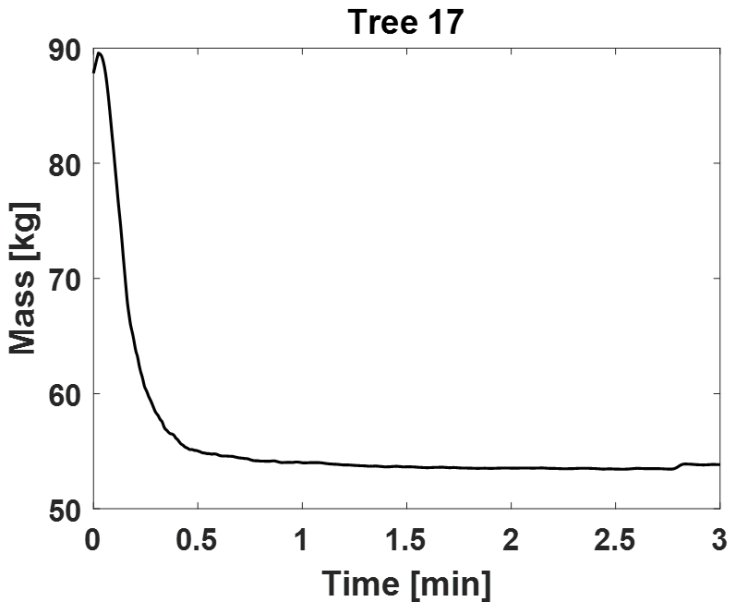

Figure C 12. Tree 17 transient load cell (wet) mass measurements with ignition at time zero.

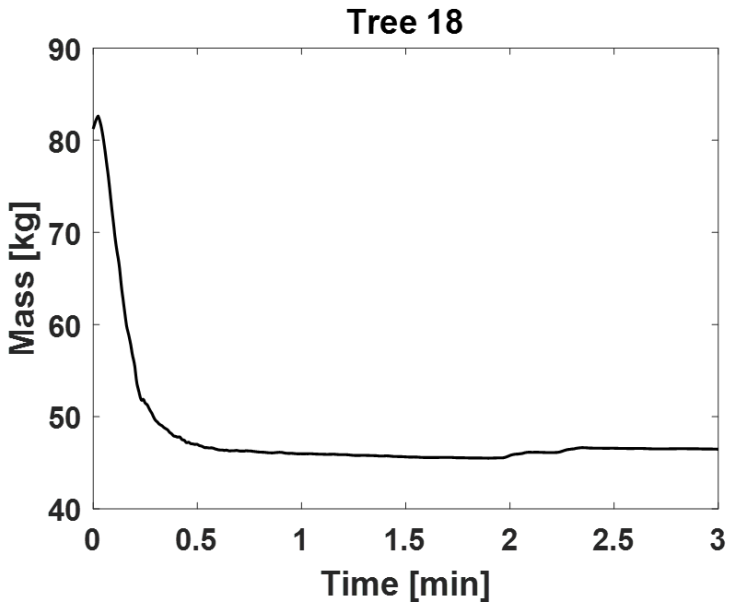

Figure C 13. Tree 18 transient load cell (wet) mass measurements with ignition at time zero.

Appendix D. Heat Flux

D.1. Heat Flux Gauge and Plate Thermometer Comparisons

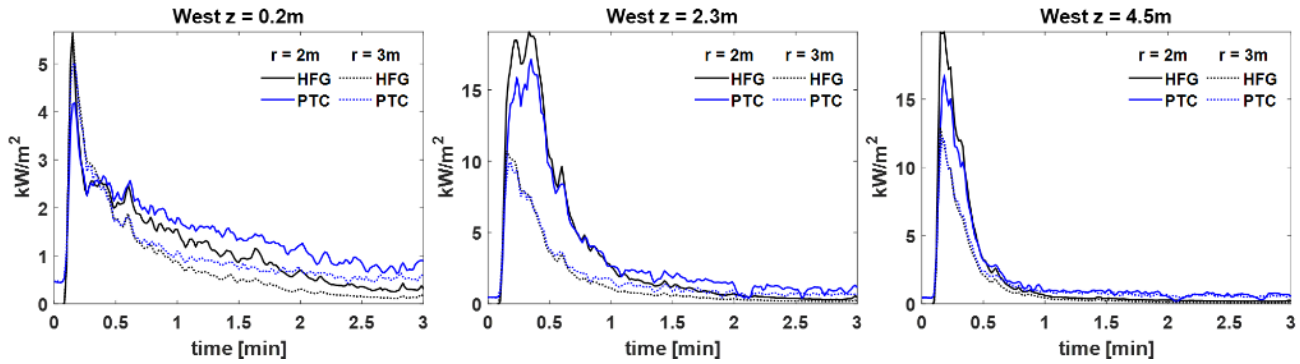

Figure D 1. Tree 1 heat flux gauge and plate thermometer comparison.

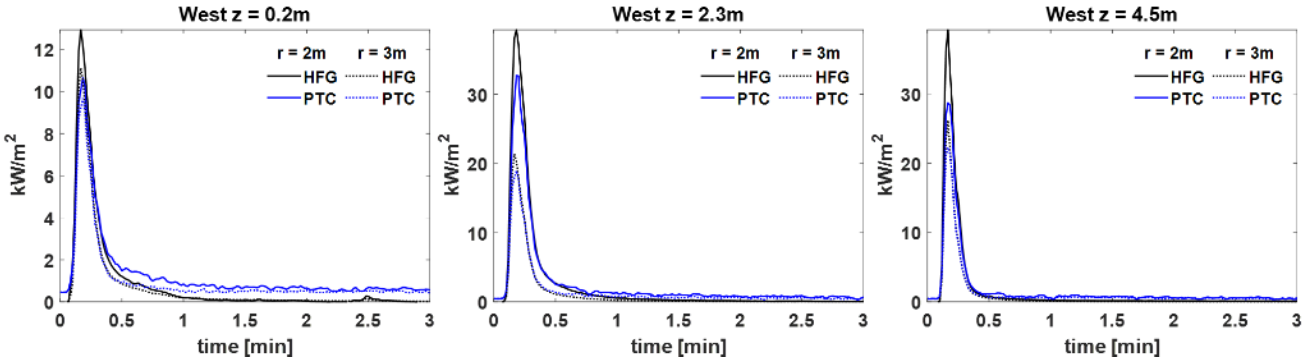

Figure D 2. Tree 2 heat flux gauge and plate thermometer comparison.

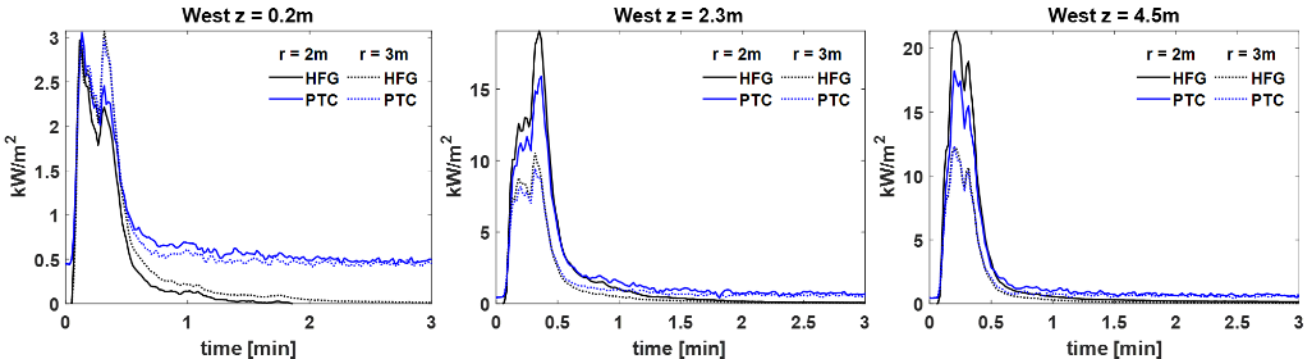

Figure D 3. Tree 3 heat flux gauge and plate thermometer comparison.

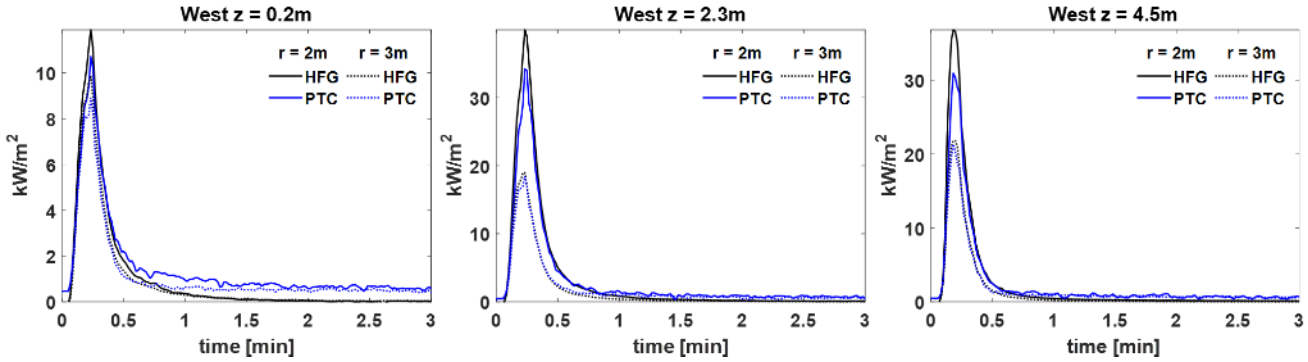

Figure D 4. Tree 4 heat flux gauge and plate thermometer comparison.

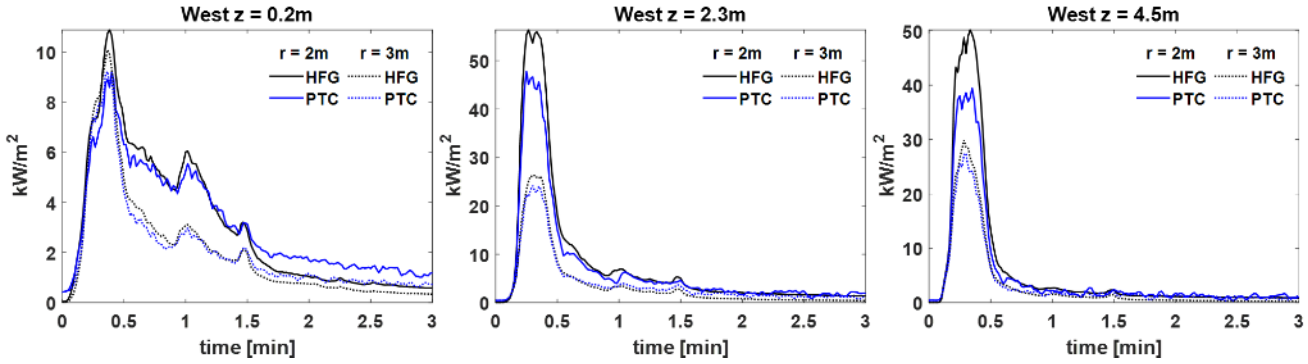

Figure D 5. Tree 5 heat flux gauge and plate thermometer comparison.

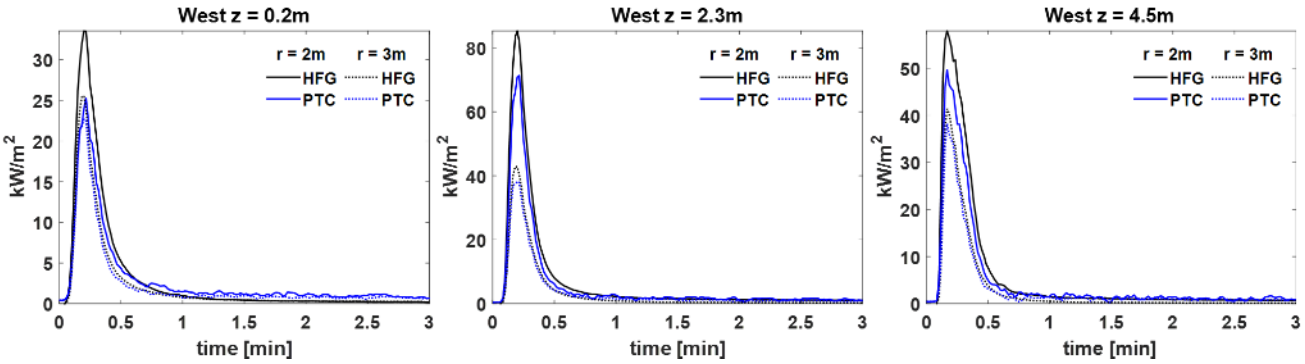

Figure D 6. Tree 6 heat flux gauge and plate thermometer comparison.

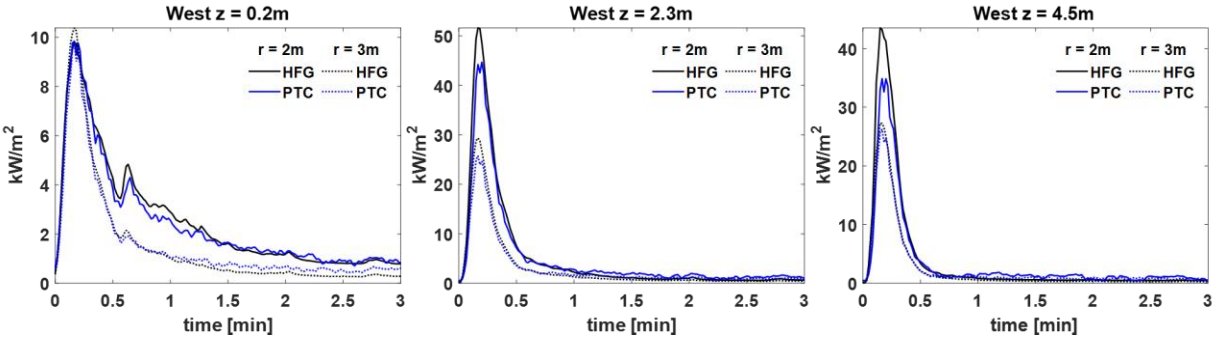

Figure D 7. Tree 7 heat flux gauge and plate thermometer comparison.

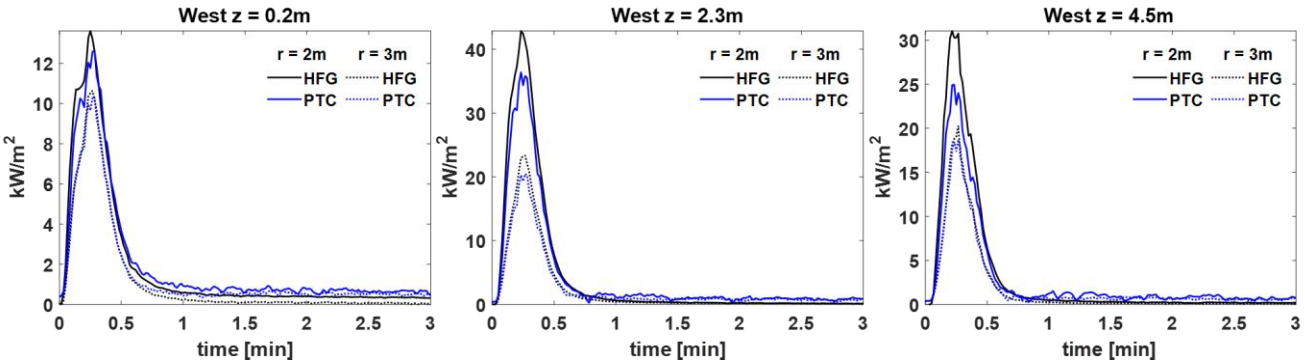

Figure D 8. Tree 8 heat flux gauge and plate thermometer comparison.

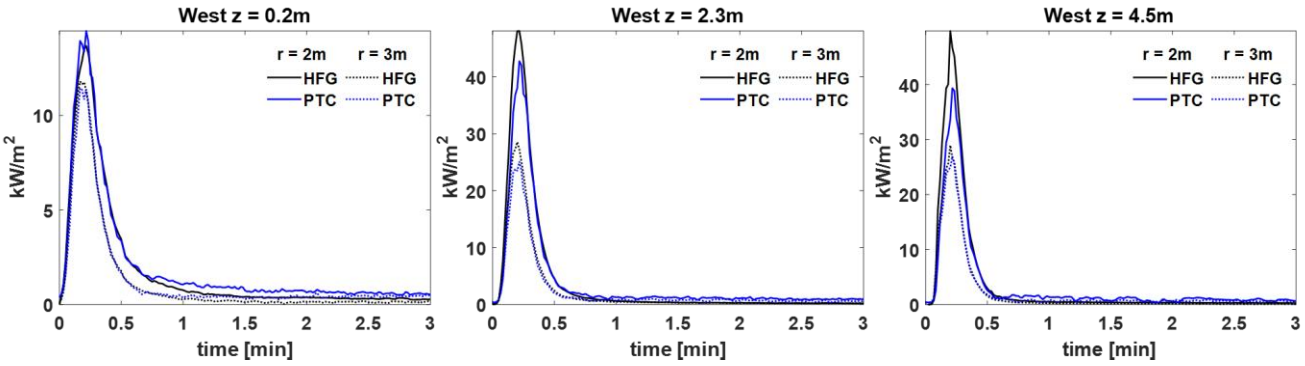

Figure D 9. Tree 9 heat flux gauge and plate thermometer comparison.

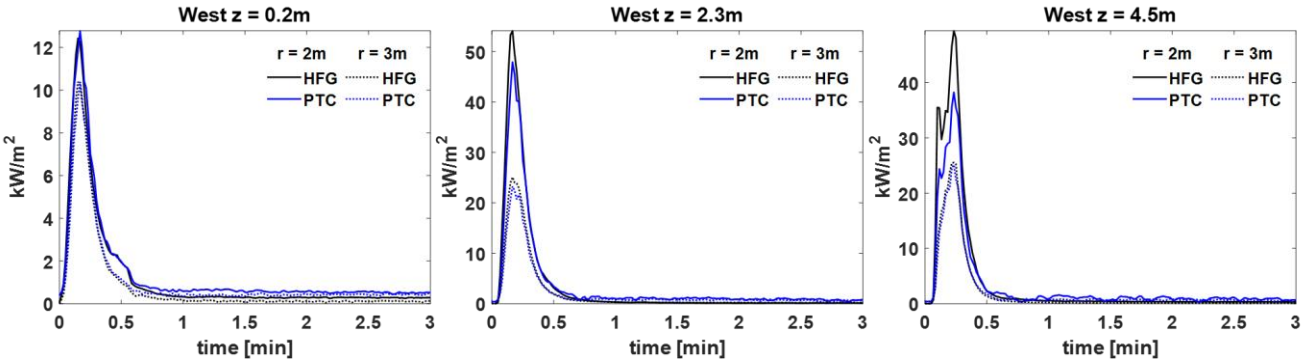

Figure D 10. Tree 10 heat flux gauge and plate thermometer comparison.

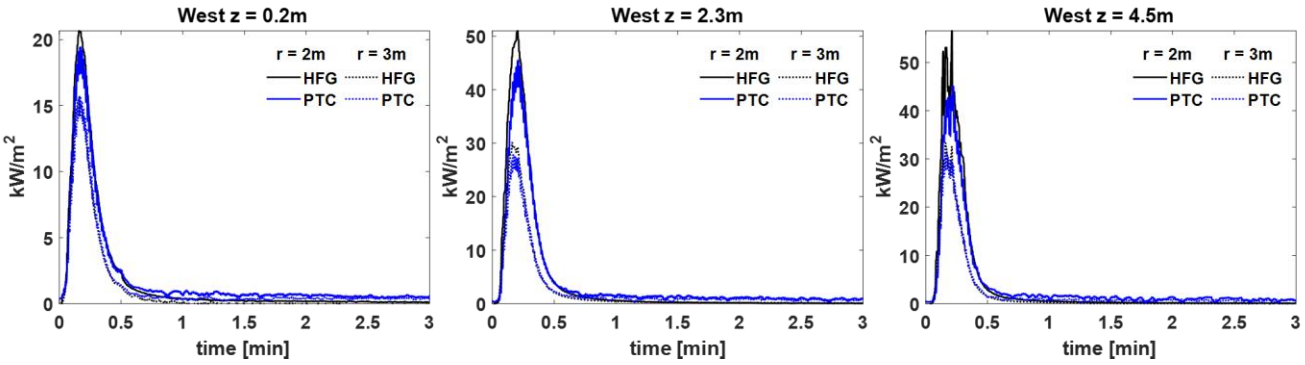

Figure D 11. Tree 11 heat flux gauge and plate thermometer comparison.

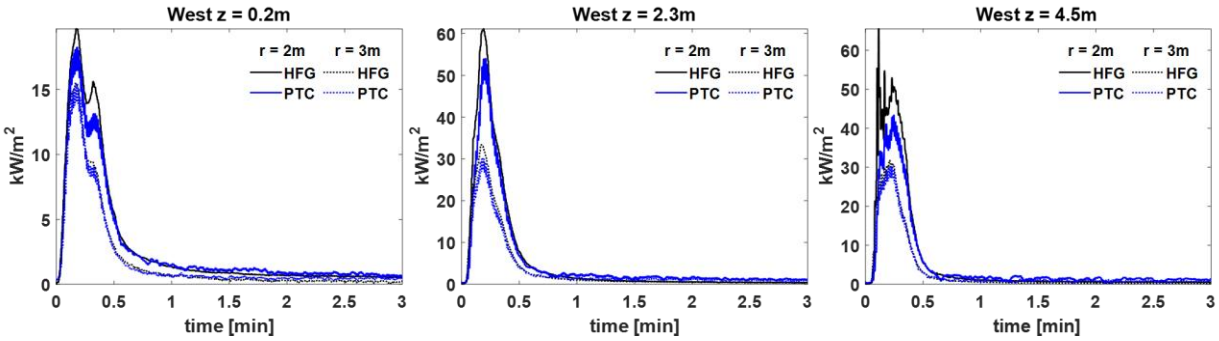

Figure D 12. Tree 12 heat flux gauge and plate thermometer comparison.

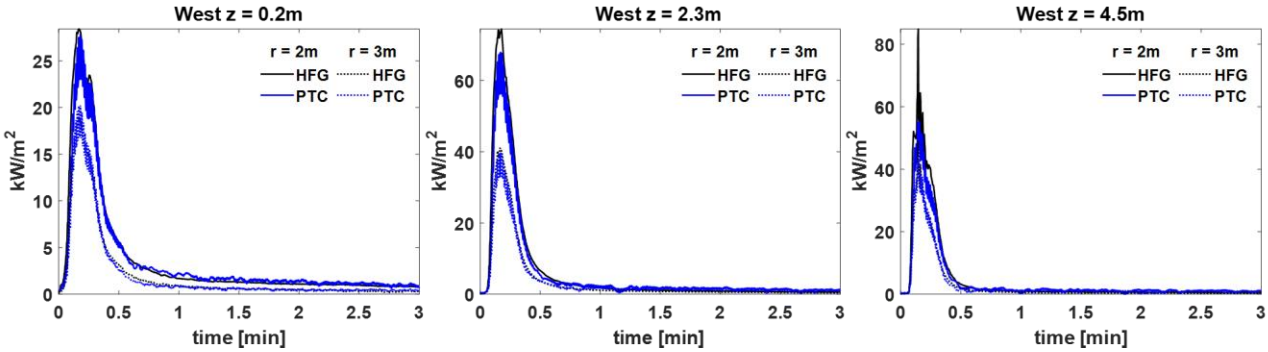

Figure D 13. Tree 13 heat flux gauge and plate thermometer comparison.

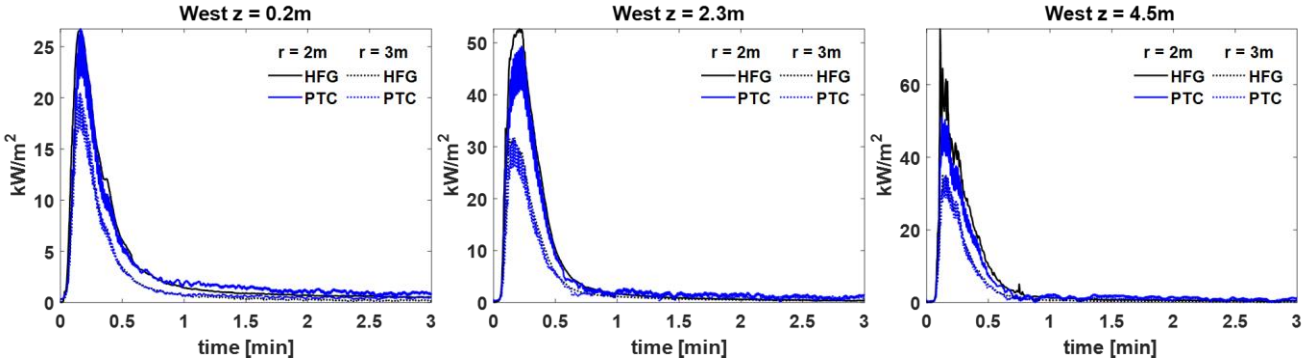

Figure D 14. Tree 14 heat flux gauge and plate thermometer comparison.

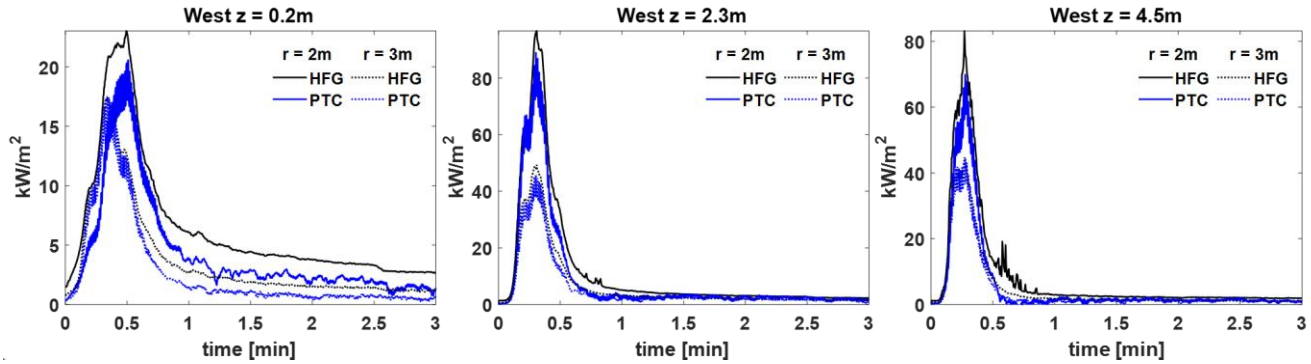

Figure D 15. Tree 15 heat flux gauge and plate thermometer comparison.

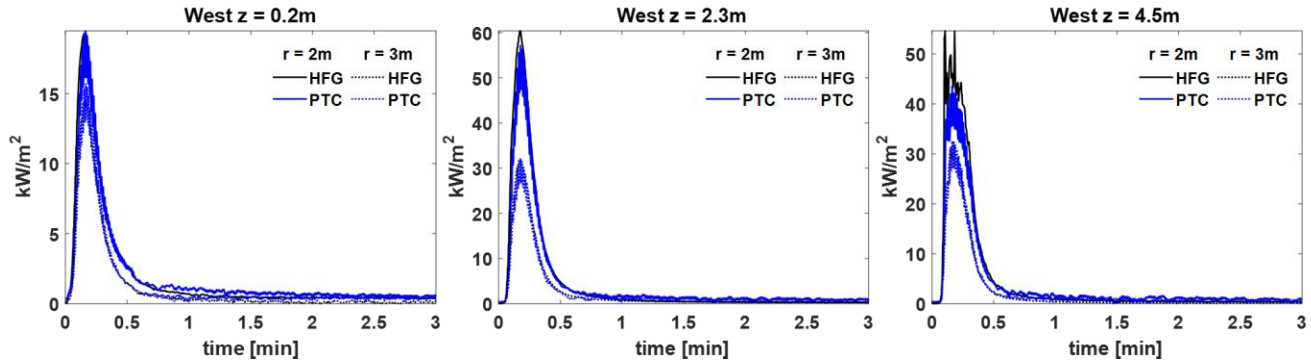

Figure D 16. Tree 16 heat flux gauge and plate thermometer comparison.

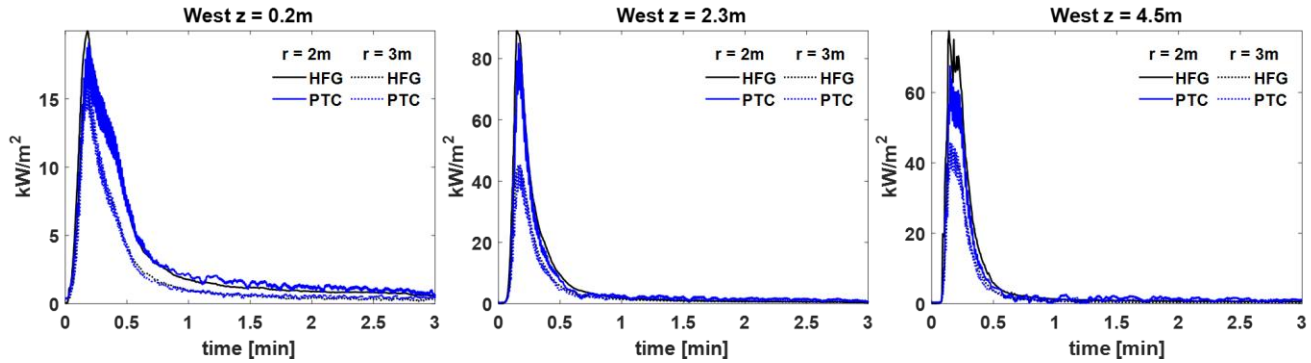

Figure D 17. Tree 17 heat flux gauge and plate thermometer comparison.

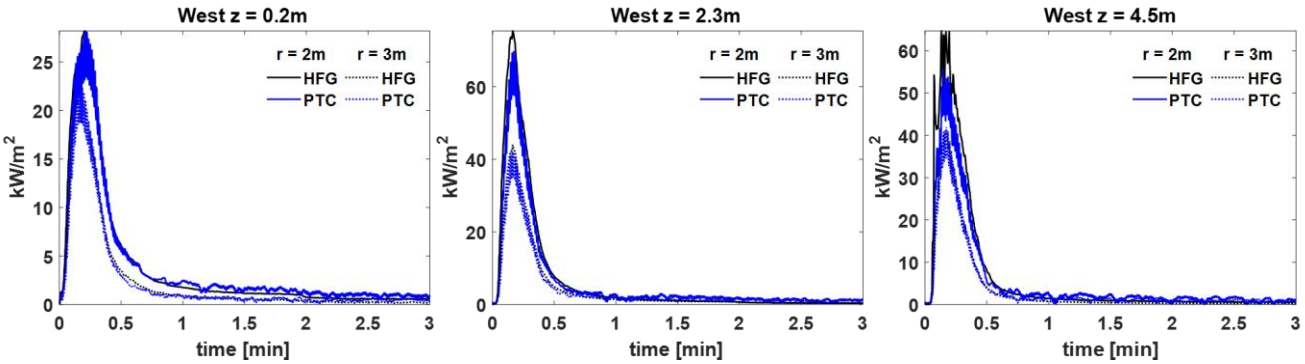

Figure D 18. Tree 18 heat flux gauge and plate thermometer comparison.

D.2. East and West Plate Thermometer Comparisons

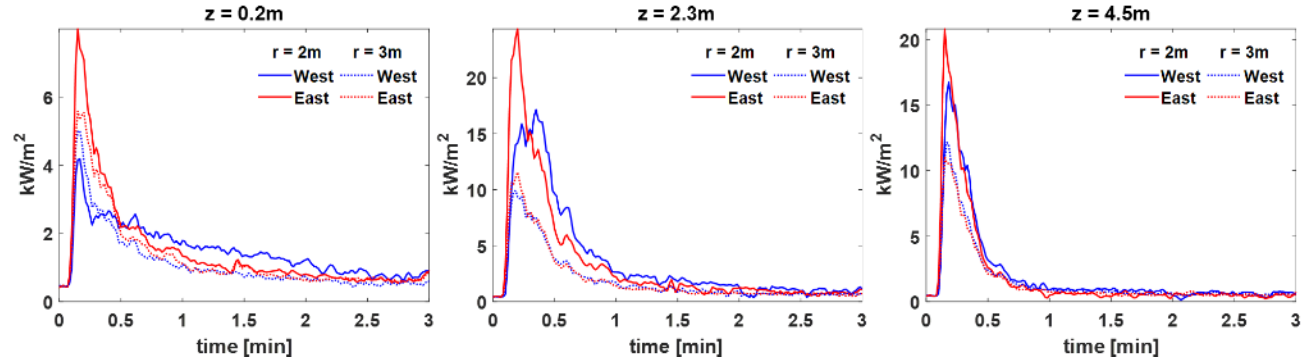

Figure D 19. Tree 1 east and west PT comparisons.

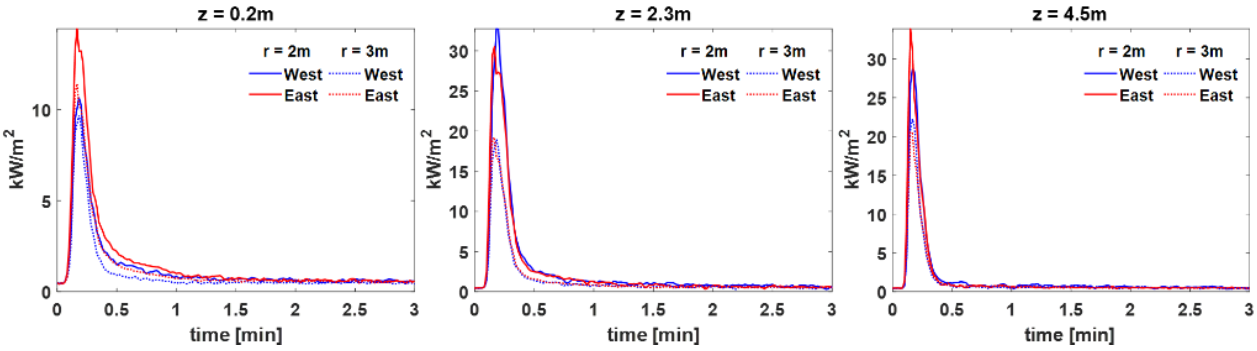

Figure D 20. Tree 2 east and west PT comparisons.

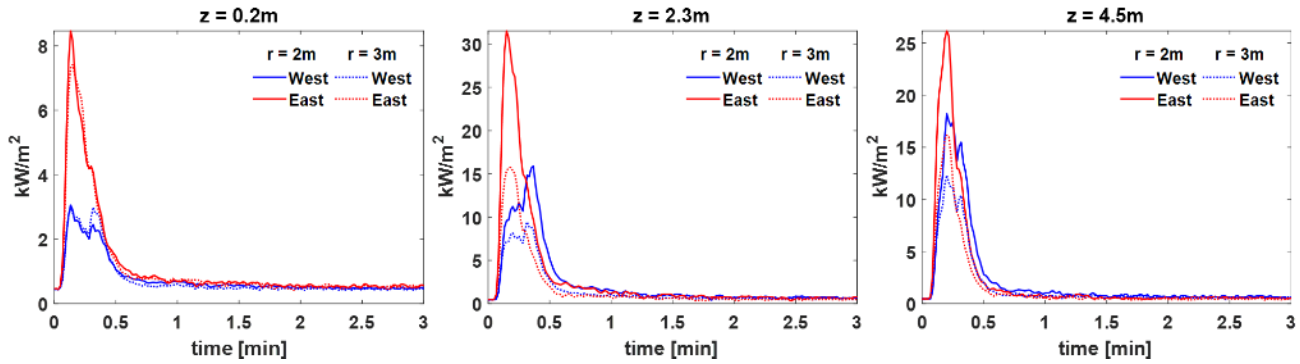

Figure D 21. Tree 3 east and west PT comparisons.

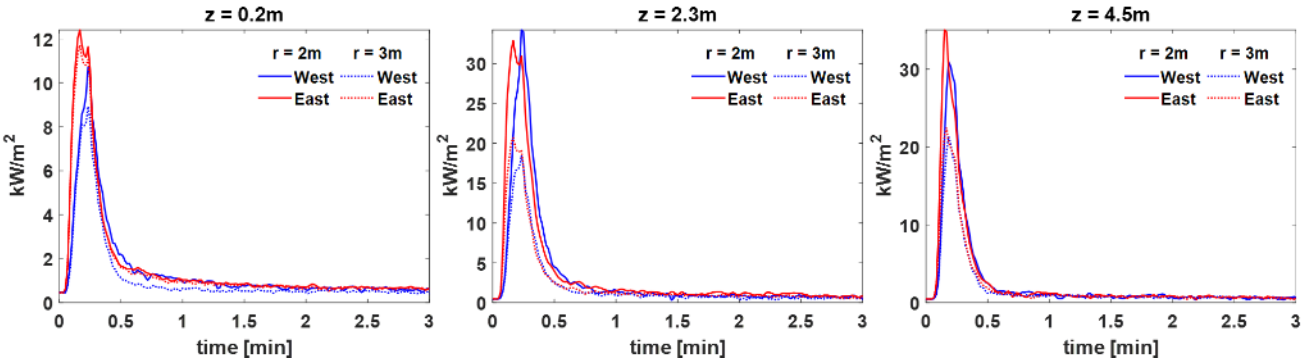

Figure D 22. Tree 4 east and west PT comparisons.

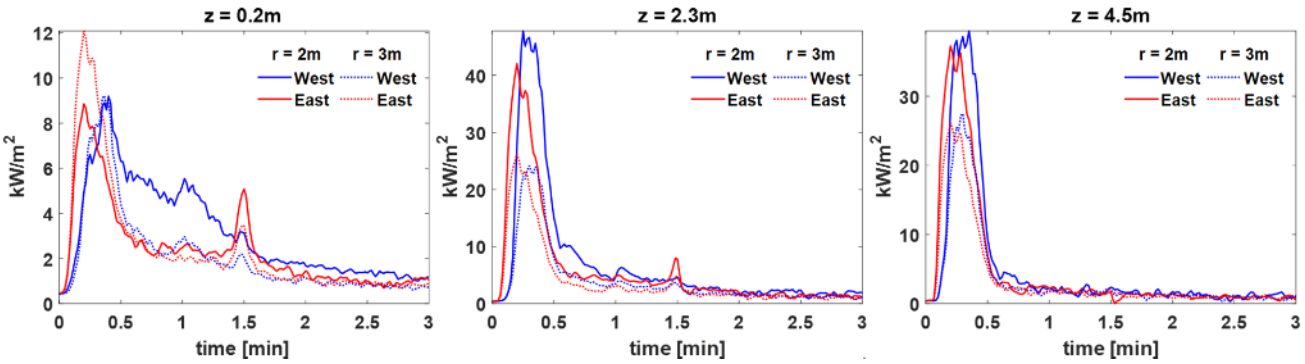

Figure D 23. Tree 5 east and west PT comparisons.

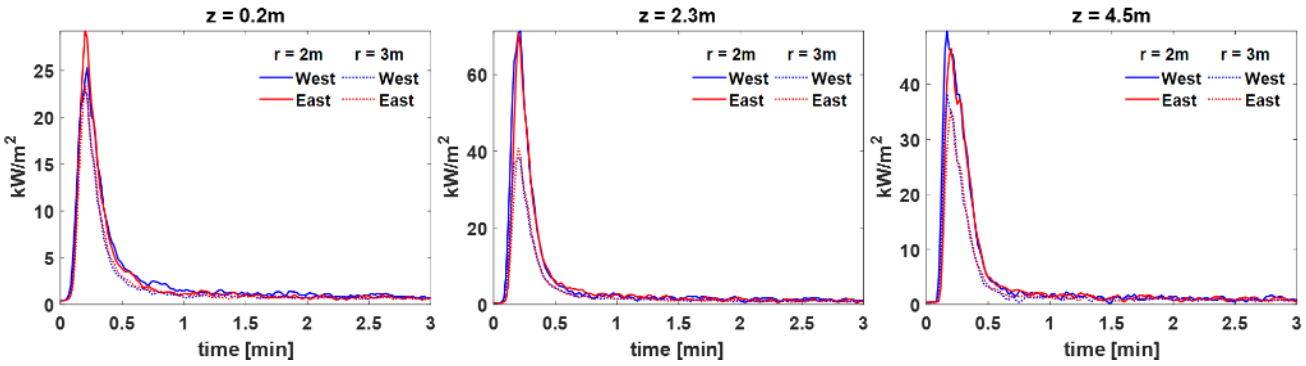

Figure D 24. Tree 6 east and west PT comparisons.

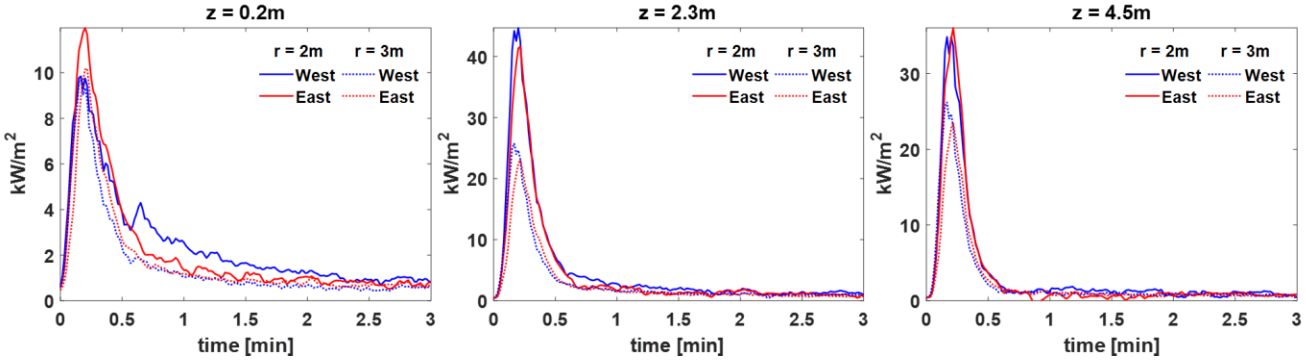

Figure D 25. Tree 7 east and west PT comparisons

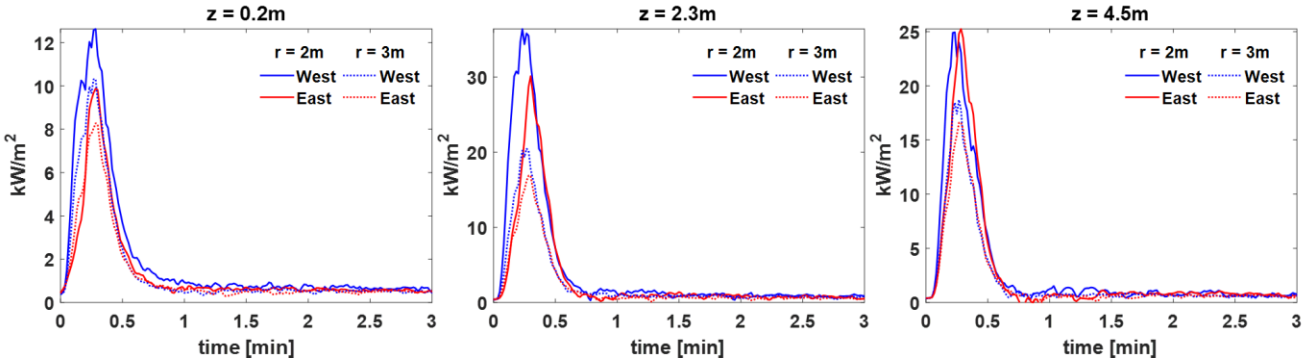

Figure D 26. Tree 8 east and west PT comparisons

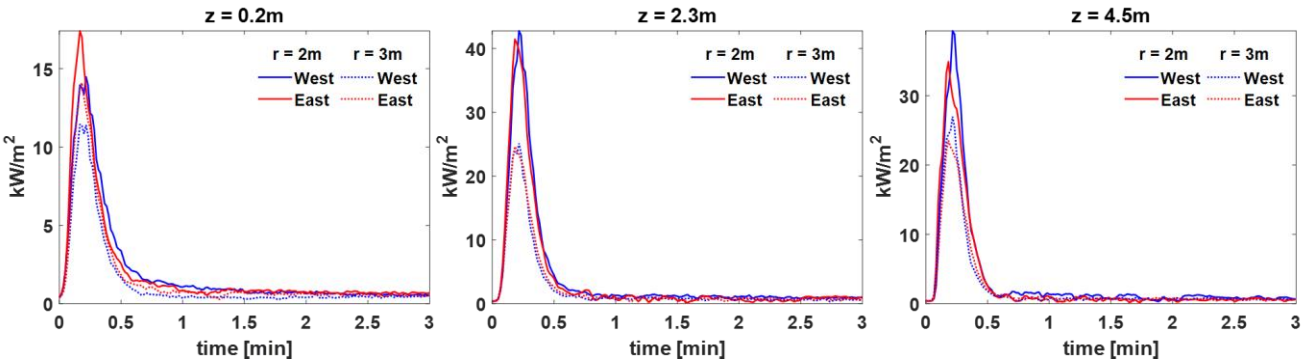

Figure D 27. Tree 9 east and west PT comparisons

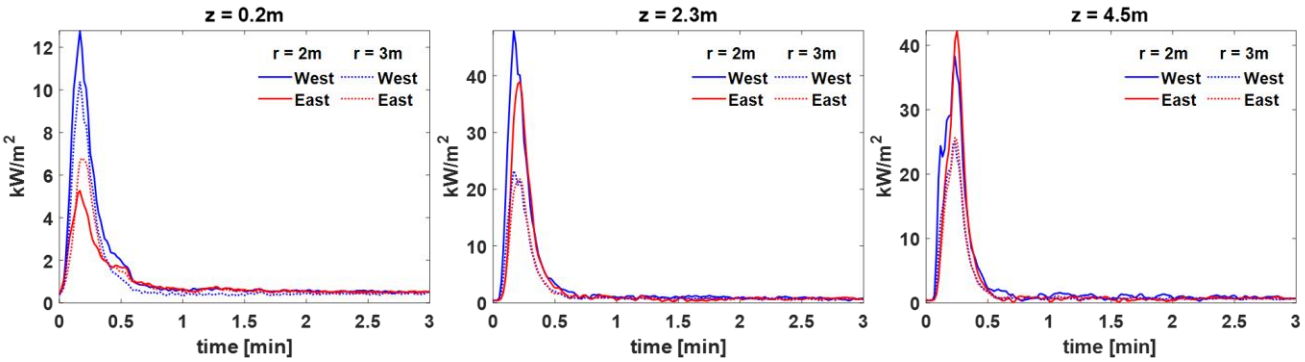

Figure D 28. Tree 10 east and west PT comparisons

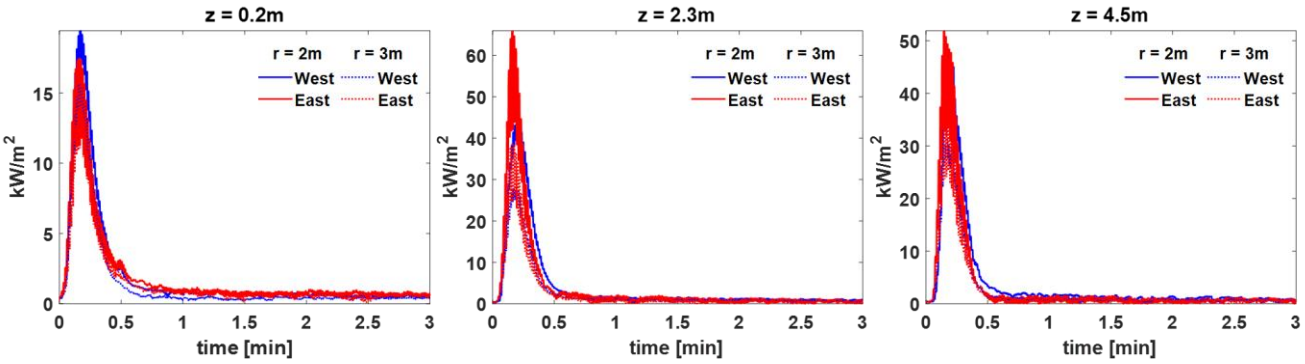

Figure D 29. Tree 11 east and west PT comparisons

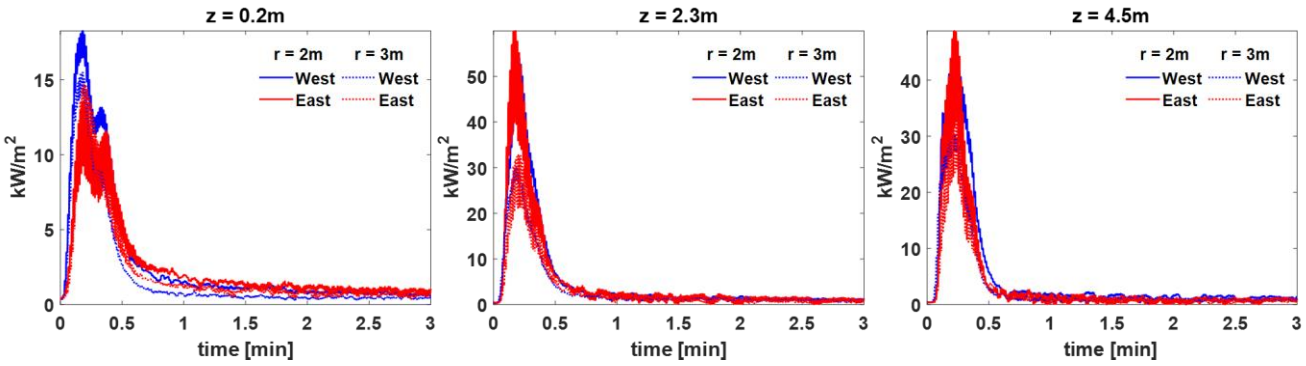

Figure D 30. Tree 12 east and west PT comparisons

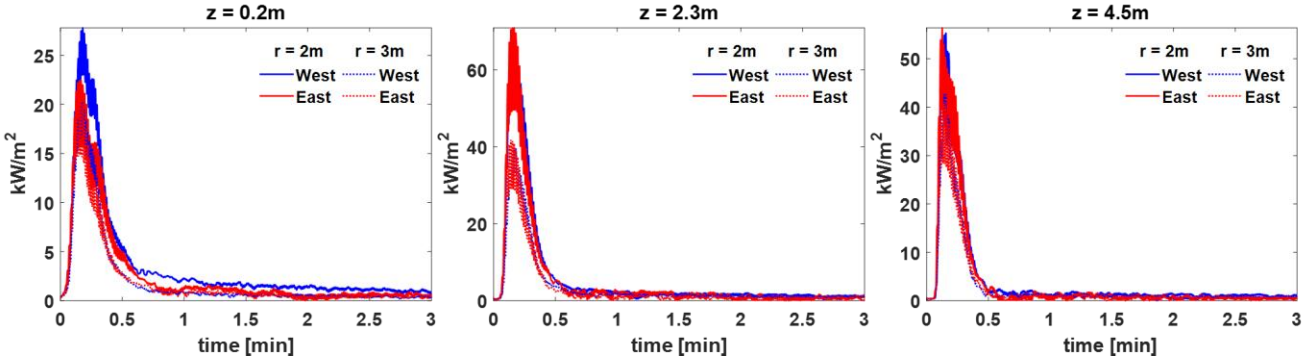

Figure D 31. Tree 13 east and west PT comparisons

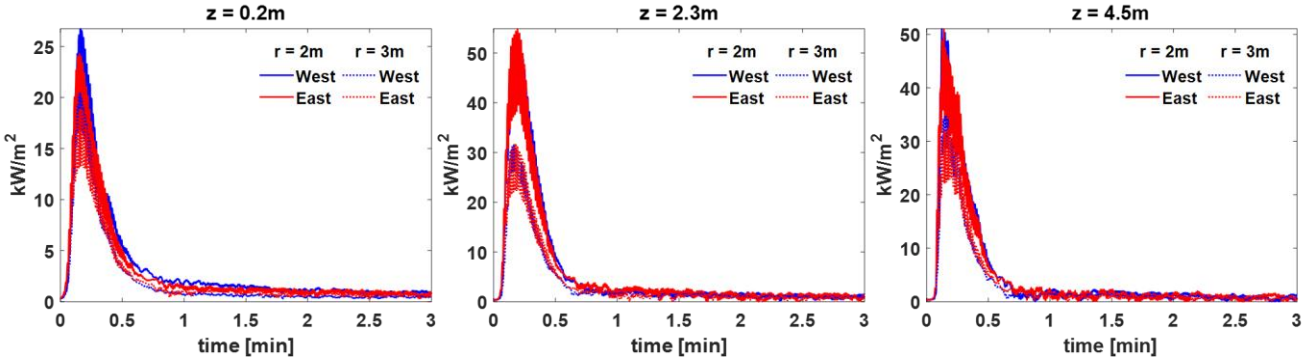

Figure D 32. Tree 14 east and west PT comparisons

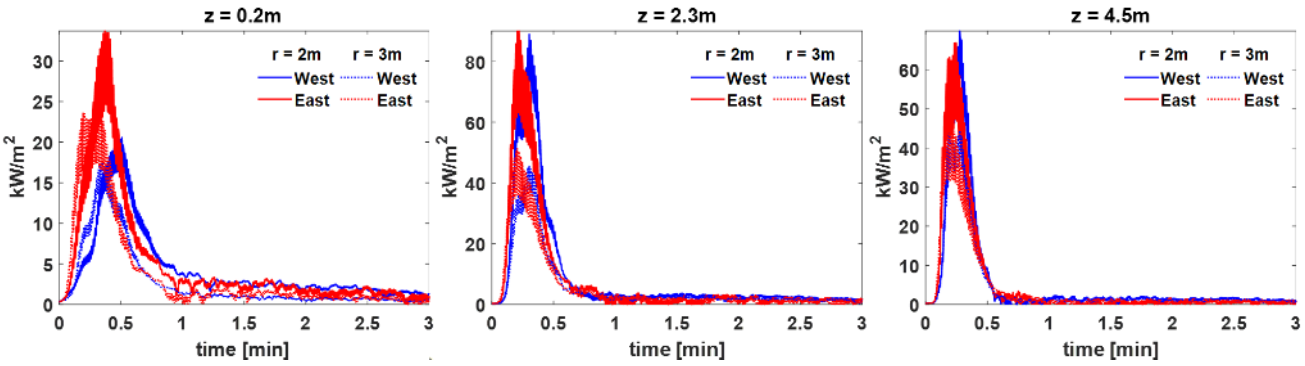

Figure D 33. Tree 15 east and west PT comparisons

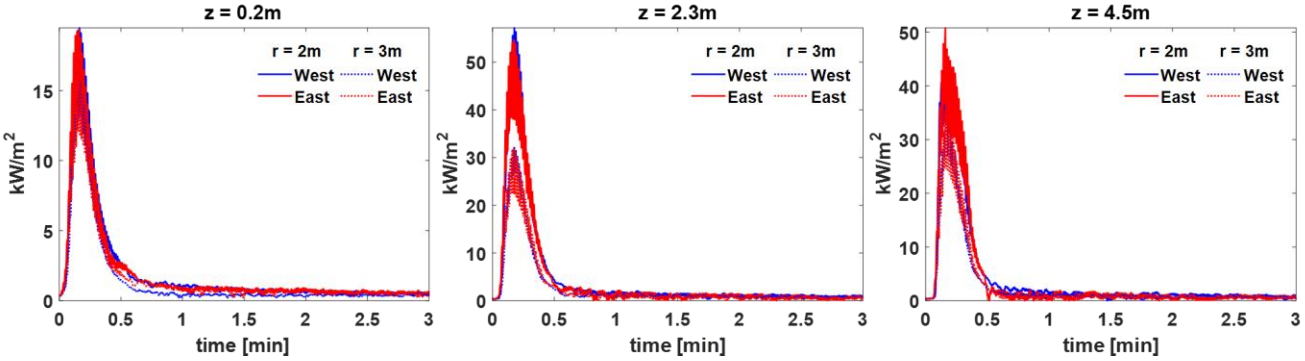

Figure D 34. Tree 16 east and west PT comparisons

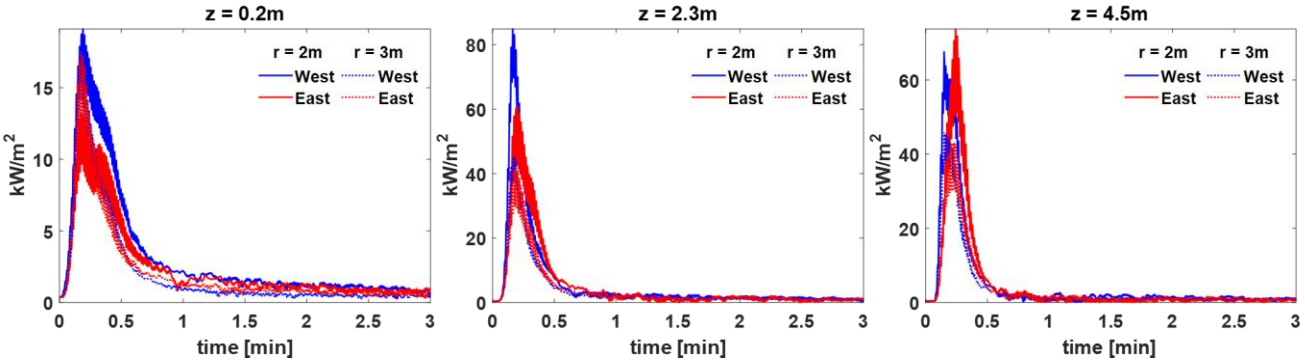

Figure D 35. Tree 17 east and west PT comparisons

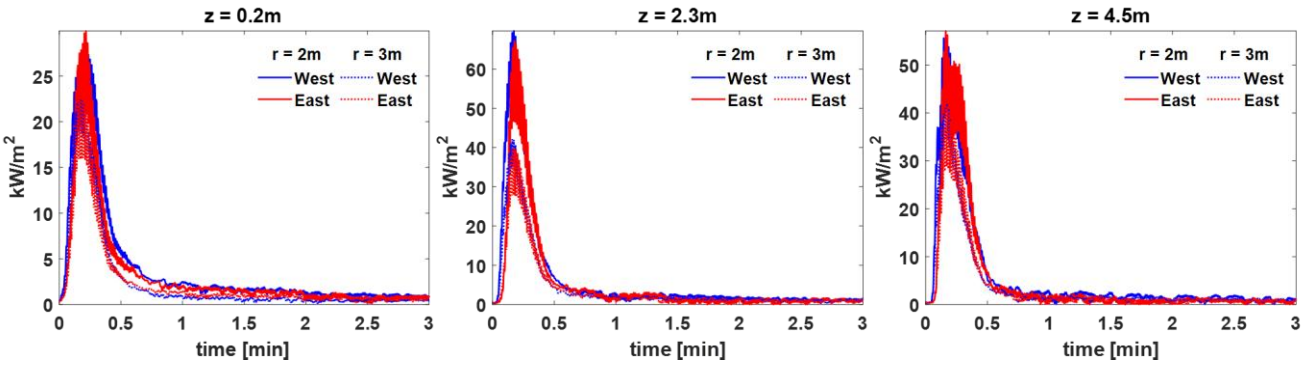

Figure D 36. Tree 18 east and west PT comparisons

D.3. Far-Field Heat Flux

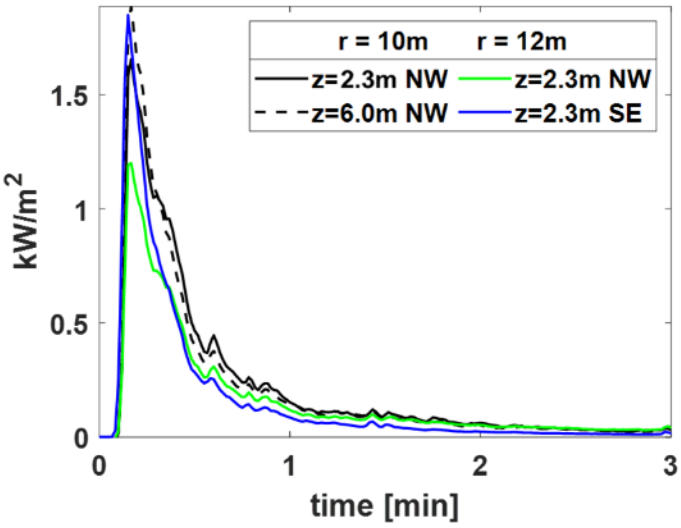

Figure D 37. Tree 1 far-field heat fluxes.

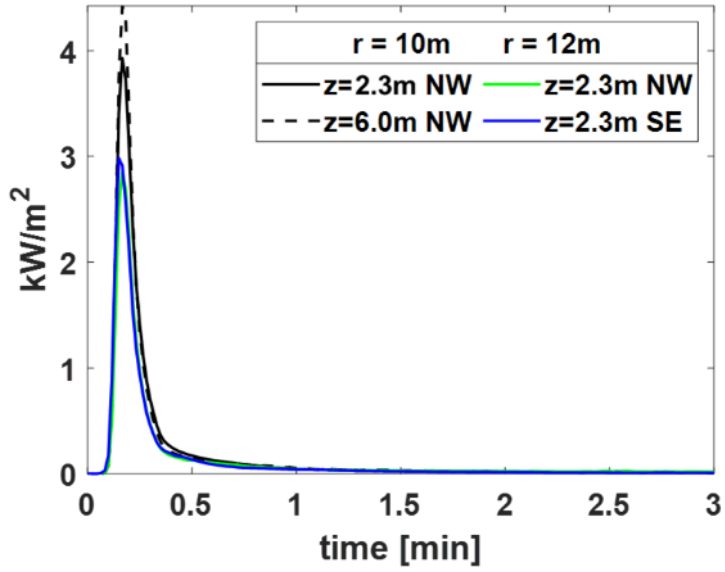

Figure D 38. Tree 2 far-field heat fluxes.

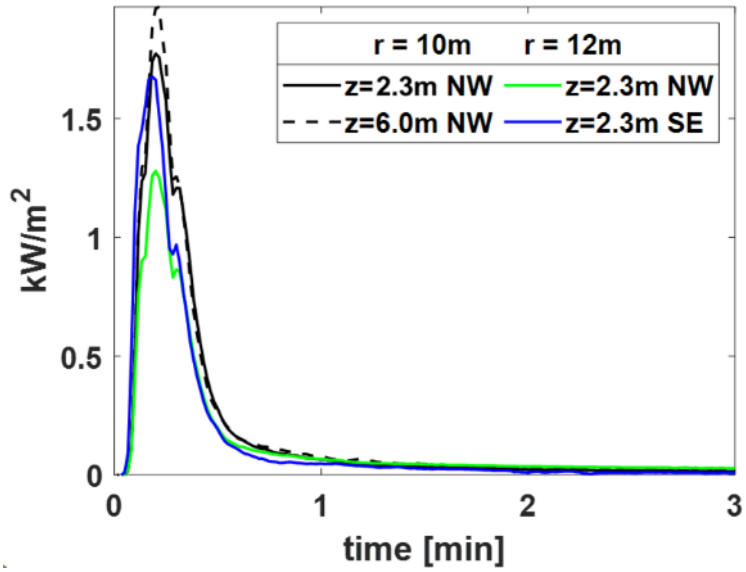

Figure D 39. Tree 3 far-field heat fluxes.

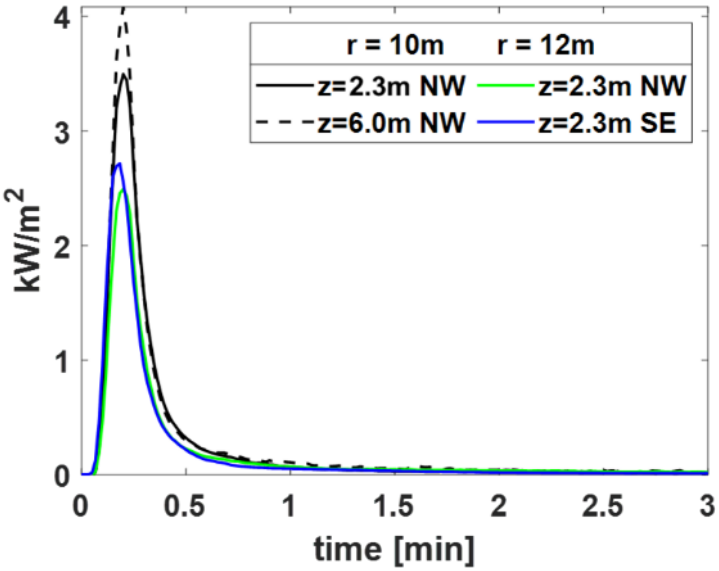

Figure D 40. Tree 4 far-field heat fluxes.

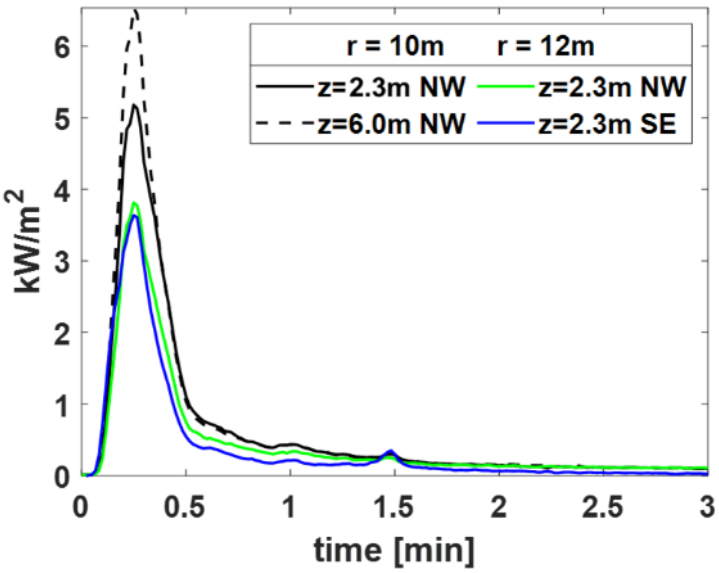

Figure D 41. Tree 5 far-field heat fluxes.

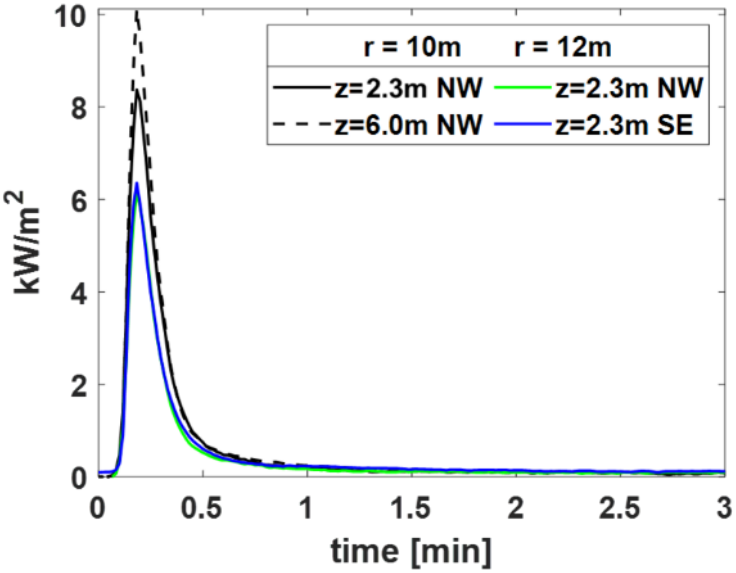

Figure D 42. Tree 6 far-field heat fluxes.

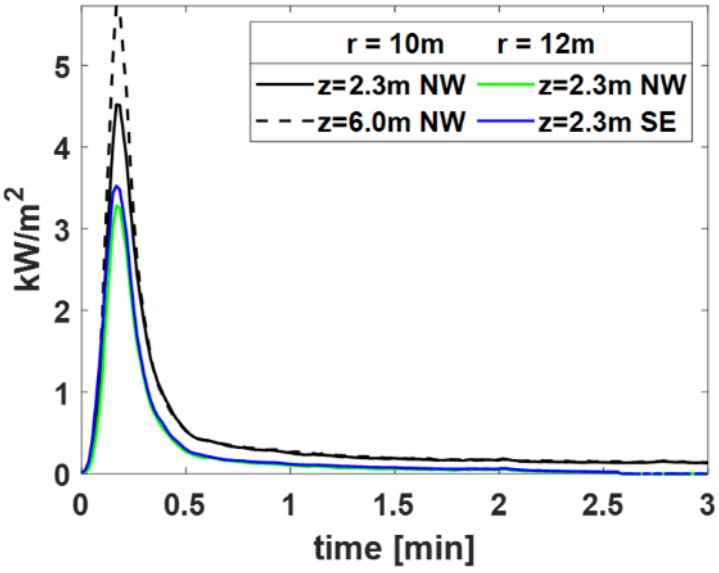

Figure D 43. Tree 7 far-field heat fluxes

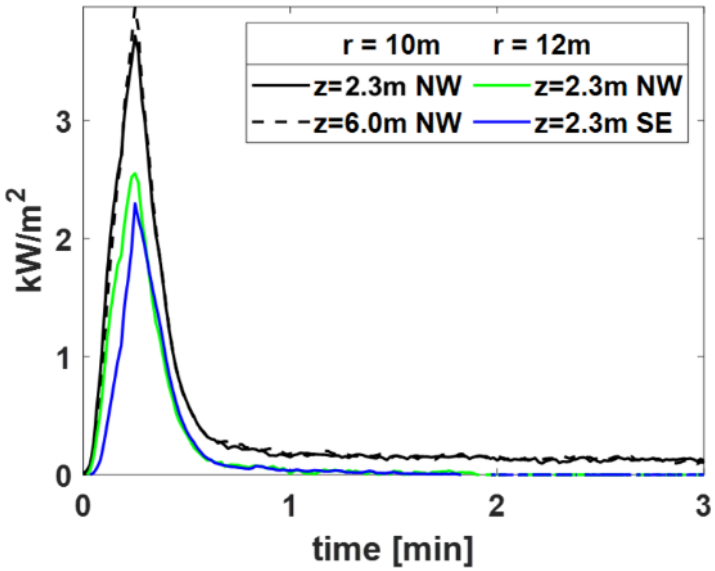

Figure D 44. Tree 8 far-field heat fluxes

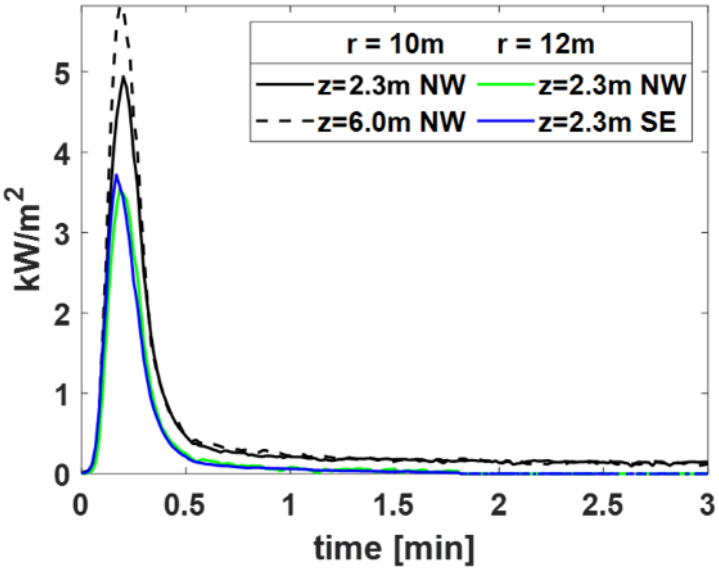

Figure D 45. Tree 9 far-field heat fluxes

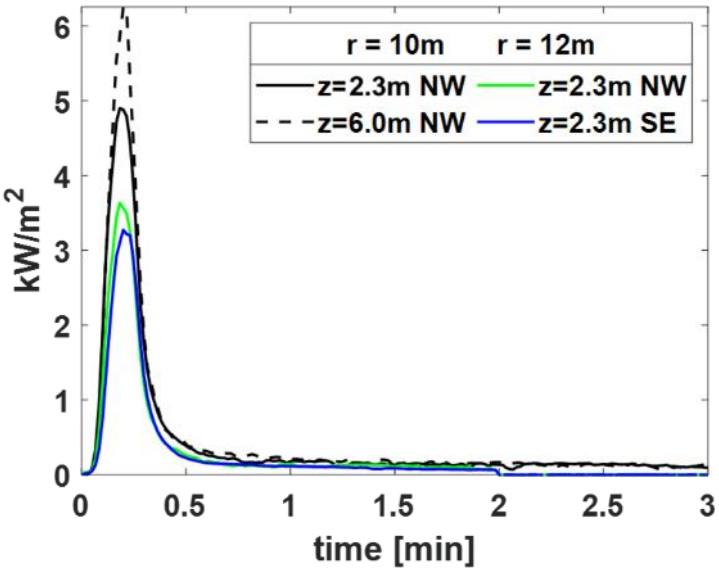

Figure D 46. Tree 10 far-field heat fluxes.

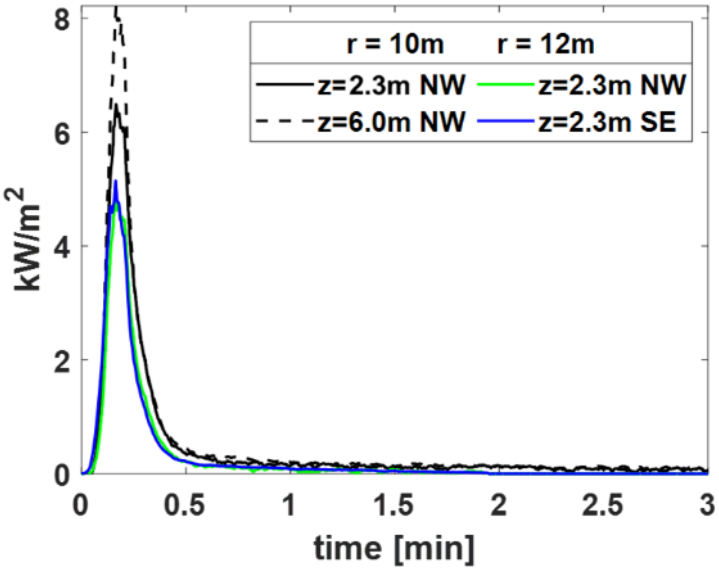

Figure D 47. Tree 11 far-field heat fluxes.

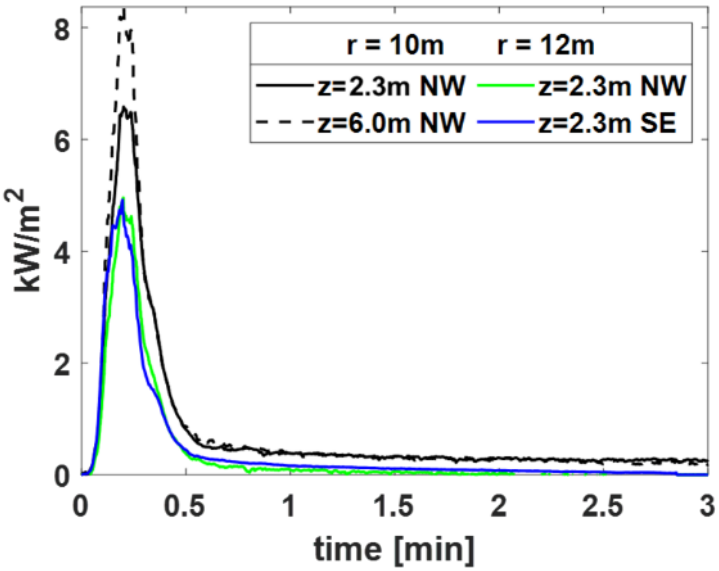

Figure D 48. Tree 12 far-field heat fluxes

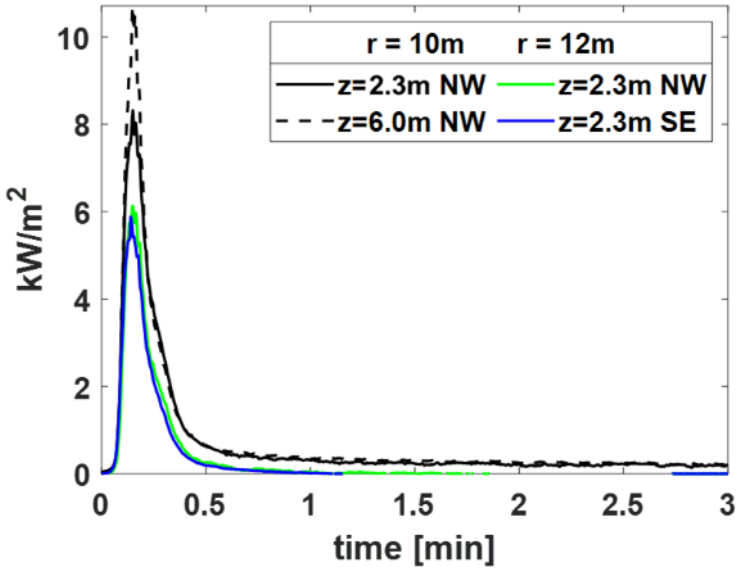

Figure D 49. Tree 13 far-field heat fluxes

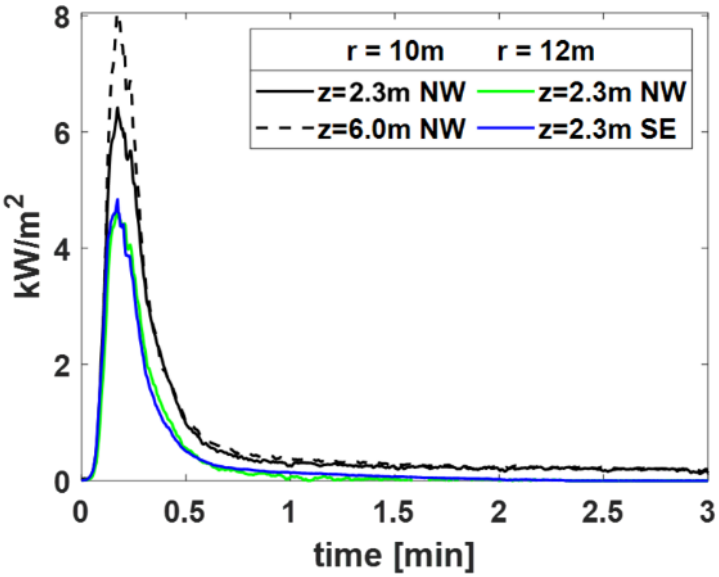

Figure D 50. Tree 14 far-field heat fluxes

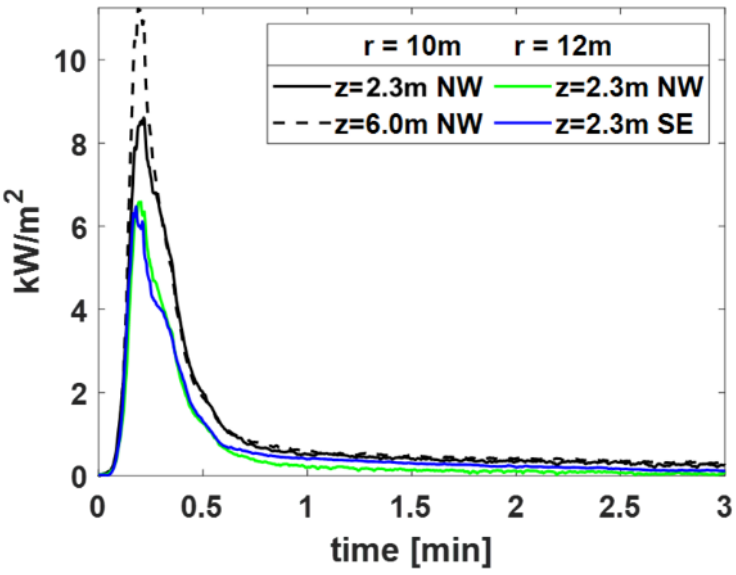

Figure D 51. Tree 15 far-field heat fluxes

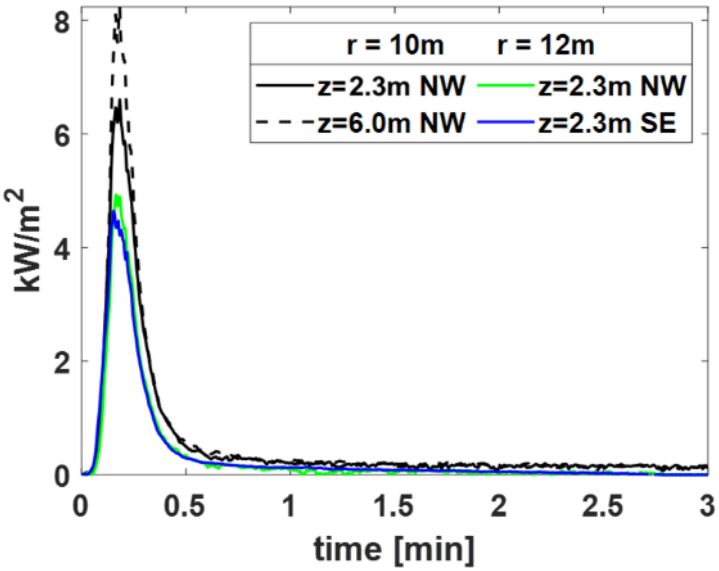

Figure D 52. Tree 16 far-field heat fluxes

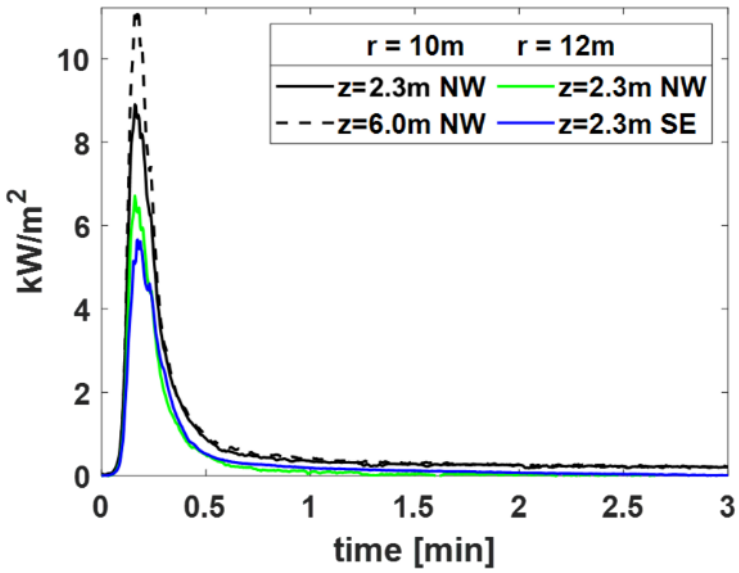

Figure D 53. Tree 17 far-field heat fluxes

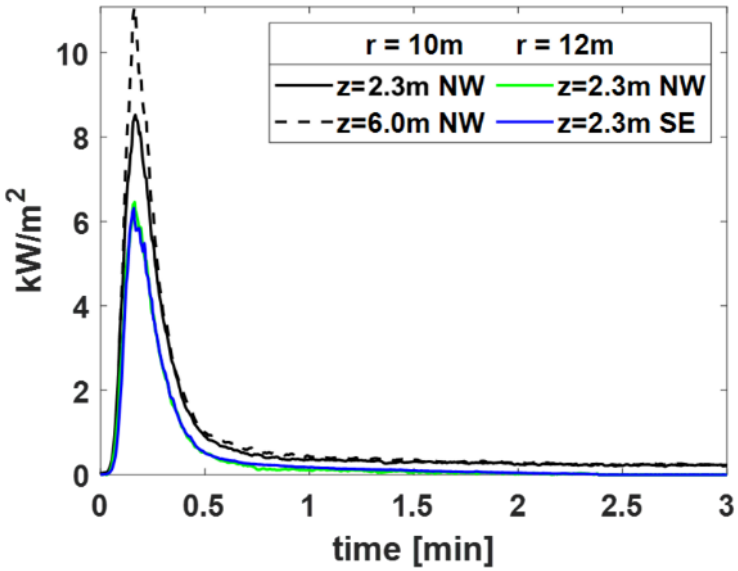

Figure D 54. Tree 18 far-field heat fluxes

Appendix E. Uncertainty in Photogrammetry Measurements

This section provides an estimate of the uncertainty associated with geometry measurements derived from photogrammetry. The first six trees are used as an example. The results for the other trees are expected to yield similar results. The proprietary algorithm does not have any stated accuracy, so instead, a point cloud was created from a known object using the same technique applied to the trees. In this case, one of the instrumentation support columns was used, with specific focus on two reference lengths: (1) the width of the column from the outside of the flanges, and (2) the width of the base plate. The photogrammetric model and the two references lengths are shown in Figure E1.

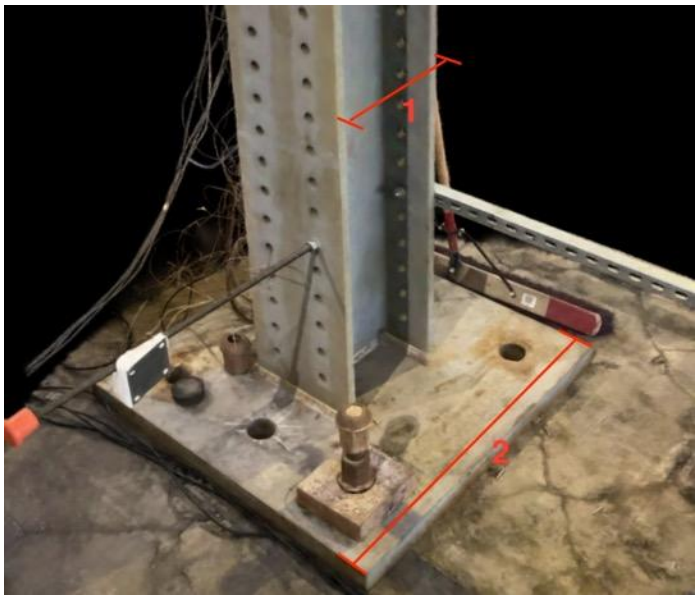

Figure E 1. Photogrammetric model of reference object (east column in Figure 2).

Points were extracted that were associated with the outside of the flanges over a 20 cm vertical length and 20 cm depth and associated with the edges of the base plate over a 20 cm depth. The reference edges were oriented in the x-direction and the average x-location of the relevant points was used to define the reference length, as shown in Figure E1.

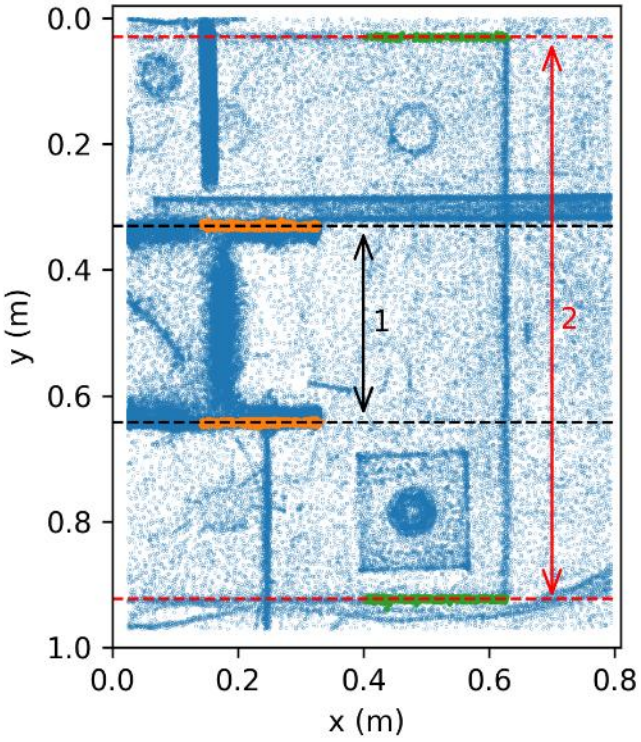

Figure E 2. Raw point cloud from photogrammetric model in previous figure. The points corresponding to the reference measurements are highlighted in orange (reference length 1) and green (reference length 2). The calculated model distances are shown as dashed lines.

The uncertainty shown in Table E1 is considered a conservative estimate because the orientation of the scene and the determination of points associated with reference edges was performed by hand. This conservative approach is followed yielding an uncertainty of a point location as 2 cm.

Table E 1 Type A uncertainty in point cloud location based on measurement of reference distances.

Reference Length	Actual Length (cm)	Average Point Cloud Distance (cm)	Uncertainty (cm)	Relative Uncertainty (%)
1	32.8	31.3	1.5	4.6
2	91.4	89.4	2.0	2.2

The absolute uncertainties for point locations are smaller than the dimensions used in the voxelization process, thus a significant contribution to uncertainty of voxel-based measurements is assumed to come from the voxel sizes (Δx) themselves. Linear measurements are assumed to

have a combined expanded uncertainty (coverage factor $k = 2$) of:

$$U_{dist} = 2\sqrt{\Delta x^2 + (0.02)^2}$$

The uncertainty of the volume is more complicated to quantify due to the irregular nature of the voxelized geometry. However, a rough estimate can be derived from assuming an elliptical conical volume from the three linear dimensions estimated (r_0, r_1, H). This gives an expanded uncertainty of:

$$U_{vol} = \frac{2\pi}{3}\sqrt{(\Delta x^2 + (0.02)^2)[(r_0 r_1)^2 + (r_0 H)^2 + (r_1 H)^2]}$$

While the 5 cm voxel size was selected for the main analysis of tree geometry, the following tables provide the same estimates produced for both 10 cm and 15 cm voxels. This provides an evaluation of the influence of fire model grid resolution when using a voxelized representation for tree geometry. The largest difference between 10 cm and 15 cm voxels on the estimated major and minor crown radii is 5 cm all within the overlapping uncertainty estimates provided in the tables below. The largest difference in the crown volumes is 2.5 m^3 or 16 %, which is also within the overlapping uncertainty estimates provided.

Table E 2. Tree dimensions determined using a 10 cm voxel size, including the combined expanded (k=2) uncertainties, representing a 95 % confidence interval.

Tree	Height (m)	Major Crown Radius (m)	Minor Crown Radius (m)	Crown Volume (m^3)
1	3.30 ± 0.20	1.21 ± 0.20	1.19 ± 0.20	6.54 ± 1.22
2	3.60 ± 0.20	1.13 ± 0.20	1.07 ± 0.20	5.73 ± 1.19
3	4.20 ± 0.20	1.46 ± 0.20	1.34 ± 0.20	9.86 ± 1.75
4	4.00 ± 0.20	1.22 ± 0.20	1.09 ± 0.20	6.92 ± 1.34
5	5.90 ± 0.20	1.56 ± 0.20	1.43 ± 0.20	17.30 ± 2.59
6	5.70 ± 0.20	1.49 ± 0.20	1.42 ± 0.20	15.23 ± 2.49

Table E 3. Tree dimensions determined using a 15 cm voxel size, including the combined expanded (k=2) uncertainties, representing a 95 % confidence interval.

Tree	Height (m)	Major Crown Radius (m)	Minor Crown Radius (m)	Crown Volume (m^3)
1	3.30 ± 0.30	1.23 ± 0.30	1.22 ± 0.30	7.59 ± 1.87
2	3.60 ± 0.30	1.14 ± 0.30	1.10 ± 0.30	6.54 ± 1.81
3	4.20 ± 0.30	1.49 ± 0.30	1.35 ± 0.30	11.45 ± 2.63
4	4.05 ± 0.30	1.27 ± 0.30	1.13 ± 0.30	8.05 ± 2.11
5	5.85 ± 0.30	1.58 ± 0.30	1.48 ± 0.30	19.80 ± 3.96
6	5.70 ± 0.30	1.53 ± 0.30	1.47 ± 0.30	17.73 ± 3.81

Appendix F. Gravimetric Particulate Matter and PAH Analysis

Particulate material (PM) was collected and analyzed as described in Section 2.3.5. Table F 1 lists the gravimetric particulate material yields based on mass collected on filters during Tests 7, 8, and 10. The average yield for these three tests was 0.011 ± 0.001 (kg/kg). The results are a factor of 2 to 3 larger than the optical particulate matter measurements (from Table 10). The reasons for the discrepancy are unclear but could be due to a number of factors. Whereas gravimetric methods measure the total mass of all particulate matter (PM), optical transmission measures only the light-absorbing components in the optical field of view at a specific wavelength (632 nm). Some portion of the particulate may consist of non-absorbing compounds like small ash particles mixed in with carbonaceous soot. It's also possible that some organic compounds, like PAH (see discussion below), could coat the soot particles, increasing their mass but not their optical absorption in the same proportion.

Appropriate calibration of the optical method could also play a role in the discrepancy. In this study and in the NIST Fire Calorimetry Database (FCD), the specific extinction coefficient for PM or "soot" is assumed to be 8.7 m^2/g. The specific optical extinction coefficient for smoldering is known to be about a factor of 2 larger than the optical extinction coefficient for flaming soot [Seader and Einhorn, 1976], which may also account for a portion of the discrepancy. It's clear that further work is needed on this topic.

PAH is a marker of incomplete burning and is a precursor to soot [Hamins, 1993; Michelsen, 2017]. The individual PAH yields for Trees 8 and 10 are shown in Figure F 1. The figure quantifies molecules with three to six rings only. The results are fairly similar for the two trees. Both share a similar trend in PAH emission profiles; both have higher yields for lighter molecular weight PAH compounds and lower yields for heavier PAHs.

Table F 1. Gravimetric and optical measurements of particulate matter yield and their ratio for Tests 7, 8, and 10. The MC from Table 1 is also listed.

Test	Gravimetric (kg/kg)	Optical (kg/kg)	Gravimetric/ Optical	MC (%)
7	0.009 ± 0.002	0.0029 ± 0.0004	3.1 ± 0.8	35.0 ± 2.2
8	0.011 ± 0.003	0.0024 ± 0.0006	4.5 ± 1.7	42.1 ± 15.6
10	0.011 ± 0.003	0.0021 ± 0.0008	5.3 ± 2.4	49.1 ± 25.8

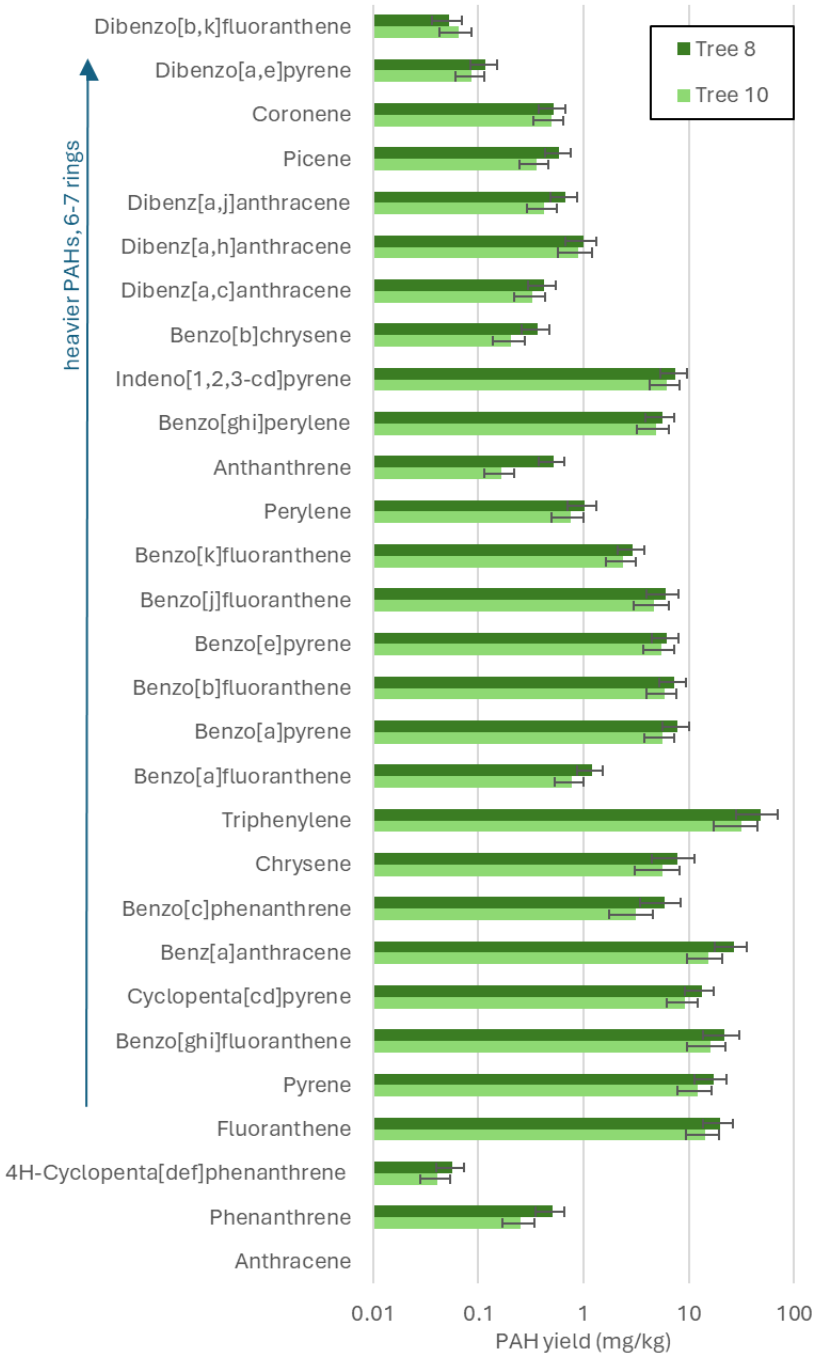

Figure F 1. The PAH yields for Tests 8 and 10.

Appendix G. Correcting the Heat Release Rates for the Calorimetry Time Response

Like all oxygen consumption calorimetry systems, the NIST NFRL calorimeter possesses an inherent system time response which is related to mixing and diffusion of the gas sample as well as the time response of the gas analyzers and flow measurement instrumentation. Utilizing near-square-wave natural gas pulses, Bryant and Bundy [2019] demonstrated that the 20 MW system has a characteristic time constant of approximately 8 s. While the calorimetry measurement system accurately conserves the total heat release (THR) over the entire burn, the system time constant significantly impacts the transient measurement of rapid fire growth events such as those observed in the present dry Douglas-fir tree experiments for which fires reached their peak HRR within 7 s to 18 s after ignition, a characteristic time on the same order as the calorimetry system's time constant. Because the system acts as a low-pass filter, it artificially "smears" or broadens the transient HRR profile. This results in two primary distortions in the calorimetry results presented in Table 8:

(1) Underestimation of the peak HRR: The measured peak HRR using oxygen consumption calorimetry is inherently lower than the true, instantaneous peak HRR of the fire. The faster the fire grows (and decays), the larger the magnitude of the discrepancy.

(2) Delay in the time to peak HRR: The time to the measured peak is delayed compared to the actual time the fire reaches its maximum.

The 20 MW exhaust hood calorimetry system effectively acts as a physical low-pass filter on rapid fire growth phenomena due to duct transport delays, mixing within the exhaust stream, and gas analyzer transit responses. To correct for the system time response, the instantaneous HRR profiles were rescaled using the relatively fast responding mass load cell and far-field radiometers as models for the corrected heat release rate profiles. The methodology, including its assumptions and limitations, are outlined in Di Cristina et al. [2025] and the Appendix of Johnson et al. [2025]. The basis for the correction is that the measured total heat release (THR; see Table 8) is invariant:

$$HRR'_q(t) = 4\pi R^2 \, \dot{q}''(t) \, \frac{THR}{TRE} \tag{G1}$$

$$HRR'_m(t) = MLR(t) \, \frac{THR}{\int_0^{t_f} MLR(t)\, dt} = MLR(t) \, \frac{THR}{\Delta m} \tag{G2}$$

where $HRR'_q(t)$ and $HRR'_m(t)$ are the corrected HRR profile rescaled using the heat flux gauges and the load cells, respectively, *TRE* is the average total radiated energy in Table 9 (using the NW and SE far-field heat flux gauges), and $\dot{q}''(t)$ is the averaged profile of the measured far field transient heat flux (see Appendix D.3) at a radial distance *R* from the tree's central axis (≅ 12 m).

The time varying fuel *MLR(t)* is corrected for moisture content as determined from the load cell data using a central differencing scheme, and t_f is the observed time when the flames were out. The parameter, *Δm*, is the total fuel mass burned, and the ratio (*THR/Δm*) is the net heat of combustion (see Table 8). The corrected HRR profiles using Eqs. G1 and G2 are shown in Figure G1 to Figure G18. The figures also show the (uncorrected) heat release rate (HRR), and the HRR estimated from the mass loss rate and the heat of combustion defined in Eq. 9 (previously presented in Figure B1 to Figure B 18).

The peak values of the corrected HRRs to the measured calorimetry HRR are of particular interest as they indicate the effect of the system time response on the actual HRR. Table G1 lists the values of the peak HRR measured by calorimetry (see Table 8) and the rescaled peak values. The time to the peak HRRs are also listed. The results in Table G1 shows that the corrected peak HRRs are on-average larger than the uncorrected oxygen calorimetry values reported in Table 8 by a factor of 1.3 and 1.4 for $HRR'_q(t_{peak})$ and $HRR'_m(t_{peak})$, respectively. Similarly, the time to $HRR'_m(t_{peak})$ values are on-average about 2.7 s earlier than the uncorrected calorimetric times. This is not surprising as the time constant for the mass load cells is much faster than the calorimetry system. What is surprising is that the time to the corrected peak based on the heat flux gauges $HRR'_q(t_{peak})$ is not significantly faster than the uncorrected peaks, which may possibly be at least partially due to synchronization of time zero (that is, ignition) for the two time series. Further investigation of this matter may be warranted. Table G1 also shows the expanded uncertainties of the HRRs and the times to the peak corrected HRRs, which are discussed in detail in Sections G.1 to G.3 below.

Table G 1 The peak HRR, the time to the peak HRR, the rescaled values using Equations G1 and G2 (also see Eq. 6 from Di Cristina et al. [2025]). The THR from Table 8 is reproduced here. The expanded (k=2) uncertainties are also listed.

	HRR O_2 Calorimetry			HRR'_m		HRR'_q	
Test	**Peak [MW]**	**Time to Peak [s]**	**THR [MJ]**	**Peak [MW]**	**Time to Peak [s]**	**Peak [MW]**	**Time to Peak [s]**
1	7.5 ± 0.8	8.0 ± 4.2	169 ± 19	11.9 ± 1.9	2 ± 2	9.8 ± 2.4	5 ± 3
2	12.5 ± 1.3	8.2 ± 4.2	160 ± 18	22.0 ± 3.4	3 ± 2	20.6 ± 4.9	6 ± 3
3	9.0 ± 1.0	9.0 ± 4.2	154 ± 17	8.2 ± 1.3	5 ± 2	10.0 ± 2.4	8 ± 3
4	13.7 ± 1.4	7.0 ± 4.2	218 ± 25	16.9 ± 2.6	7 ± 2	17.8 ± 4.3	8 ± 3
5	36.6 ± 3.9	10.0 ± 4.2	594 ± 66	37.4 ± 5.9	10 ± 2	32.4 ± 7.8	12 ± 3

Test	HRR O_2 Calorimetry			HRR'_m		HRR'_q	
	Peak [MW]	Time to Peak [s]	THR [MJ]	Peak [MW]	Time to Peak [s]	Peak [MW]	Time to Peak [s]
6	42.1 ± 4.5	8.0 ± 4.2	622 ± 67	69.8 ± 10.9	5 ± 2	56.1 ± 13.5	6 ± 3
7	26.2 ± 2.8	9.0 ± 4.2	455 ± 50	18.5 ± 2.9	7 ± 2	31.2 ± 7.5	10 ± 3
8	14.5 ± 1.6	9.6 ± 4.2	324 ± 36	*	*	21.3 ± 5.1	15 ± 3
9	27.2 ± 2.9	9.6 ± 4.2	495 ± 55	*	*	37.9 ± 9.1	11 ± 3
10	35.0 ± 3.8	10.0 ± 4.2	513 ± 57	*	*	36.4 ± 8.7	12 ± 3
11	26.3 ± 2.8	9.0 ± 4.2	406 ± 45	*	*	37.9 ± 4.2	9.8 ± 2.4
12	35.5 ± 3.7	10.0 ± 4.2	616 ± 68	*	*	42.4 ± 4.7	11.8 ± 2.4
13	29.0 ± 3.1	9.0 ± 4.2	481 ± 54	50.0 ± 7.0	4.4 ± 0.2	53.5 ± 5.9	8.8 ± 2.4
14	30.1 ± 3.2	10.0 ± 4.2	550 ± 61	50.9 ± 7.2	7.0 ± 0.2	37.4 ± 4.1	10.2 ± 2.4
15	39.9 ± 4.3	10.0 ± 4.2	885 ± 99	65.3 ± 9.2	8.4 ± 0.2	45.0 ± 5.0	10.8 ± 2.4
16	28.4 ± 3.0	10.0 ± 4.2	445 ± 50	45.1 ± 6.4	6.8 ± 0.2	34.1 ± 3.8	9.6 ± 2.4
17	38.5 ± 4.1	9.0 ± 4.2	701 ± 79	64.4 ± 9.1	8.4 ± 0.2	54.8 ± 6.0	10.2 ± 2.4
18	40.7 ± 4.3	9.0 ± 4.2	753 ± 84	66.6 ± 9.4	7.6 ± 0.2	55.9 ± 6.1	9.6 ± 2.4
* not available – the mass loss data during Tests 8 to 12 were corrupted.							

G.1. Uncertainty Estimate of $HRR'_q(t = t_{peak})$

The value and uncertainty of the peak of the corrected HRR based on the radiative heat flux in Eq. G1 is listed in Table G1. It can be determined by considering the definition of TRE given in Eq. 2. For the i^{th} heat flux gauge:

$$HRR'_{q\_peak} = 4\pi R_i^2 \, \dot{q}''_{i\_peak} \, \frac{THR}{\int_0^{te} 4\pi R_i^2 \, \dot{q}''_i(t) \, dt} = \frac{THR}{\int_0^{te} \frac{(S_i(t) - S_b)}{(S_{i\_peak} - S_b)} dt} \quad \text{(G3)}$$

where the $4\pi R_i^2$ and the calibration factor drop out of the equation since this term appears in both the numerator and denominator, leaving the integral of the heat flux signal. The main uncertainty in S_i(t) is the DAQ uncertainty, which is negligible.

The heat flux signal peaked at about 5 s to 12 s (see Table G1) and had a full-width at half-maximum from about 6 s to 14 s. Data was taken for longer than 100 s with the signal

approaching the baseline at about 50 s to 60 s after ignition. The data was acquired at 200 Hz, time averaged, and recorded at 1 Hz and 10 Hz for Trees 1 – 10 and Trees 11 – 18, respectively so that random measurement errors are very small. The integral of the heat flux gauge signal was calculated using numerical trapezoidal integration, which makes the result essentially invariant to instrument time response.

Examination of the signal showed that the standard uncertainty of the background signal $u(S_b)$, was about 2 % of the peak signal (after background subtraction), that is 0.02· $(S_{i\_peak}$- $S_b)$, representing a systematic bias in both the numerator and denominator of the integral in Eq. G3, rewritten here as:

$$I = \int_0^{t_e} \frac{(S_i(t) - S_b)}{(S_{i\_peak} - S_b)}\, dt \tag{G4}$$

The uncertainty of the integral in terms of the background signal, S_b, can be written as:

$$u_c(I) = c_{S_b} \cdot u(S_b) = \int_0^{t_e} \left(\frac{S_i(t) - S_{i\_peak}}{(S_{i_{peak}} - S_b)^2}\right) dt \cdot \left(0.02\, S_{i_{peak}}\right) \tag{G5}$$

where c_{S_b} is the sensitivity coefficient $(\frac{\partial \mathrm{I}}{\partial \mathrm{S}_b})$. The denominator of c_{S_b} is composed of constants and the integral can be broken into parts:

$$c_{S_b} = \frac{1}{(S_{i_{peak}} - S_b)^2} \left[\int_0^{t_e} S_i(t)dt - \int_0^{t_e} S_{i_{peak}}(t)dt\right] \tag{G6}$$

where the second integral is simply: $S_{i_{peak}}(t) \cdot t_e$. The uncertainty in the integral is affected by the uncertainty in the baseline. To simplify error propagation of the first integral in Eq. G6, the profile $S_i(t)$ was modelled as a Lorentzian-like line shape (Maddams, 1980).

The integrated area (I) of a Lorentzian profile is: $I = \gamma\, \pi$, where γ is the half-width at half-maximum of the Lorentzian profile. For Tests 1–10, the 1 Hz data recording time exceeded the Schmidt-Boelter heat flux gauge's 0.45 s response time, so discretization error dominates the profile uncertainty, smearing the peak determination. However, for Tests 11–18, the 10 Hz recording interval, the signal is not smearing 1 s worth of data together, the true, sharp physical shape of the Lorentzian-like peak is essentially resolved and the baseline tail drops to its true value faster, so the discretization error is essentially eliminated.

Then considering the integral for Tests 1 -10 and propagating uncertainty following Taylor and Kuyatt [1994], a closed form solution for c_{S_b} in Eq. G6 is found such that the sensitivity coefficient becomes:

$$c_{S_b} = \frac{\pi\gamma - t_e}{S_{i\_peak} - S_b} \tag{G7}$$

Equations G5 and G7 lead to:

$$\frac{u_c(I)}{I} = \frac{c_{S_b} \cdot u(S_b)}{I} = \left(\frac{|\pi\gamma - t_e|}{S_{i_{peak}} - S_b}\right) \frac{0.025\ (Si_{peak} - Sb}{\gamma\ \pi}) = \left(\frac{|\pi\gamma - t_e|}{\gamma\ \pi}\right) 0.025 = 0.02\ |1 - \frac{t_e}{\pi\gamma}| \quad \text{(G8)}$$

The value of γ varied from about 3 s to 7 s, depending on the test as seen in Figure G1 to Figure G 18. Taking t_e= 60 s, the relative contribution of the uncertainty in the background signal is 10.7 % and 3. 4 % for γ equal to 3 s and 7 s, respectively.

The combined expanded uncertainty of the corrected peak HRR (HRR'_{q_peak}) must also consider the uncertainty in the numerator of Eq. G3, involving THR:

$$\frac{U_c\left(HRR'_{q_{peak}}\right)}{HRR'_{q_{peak}}} = 2\sqrt{(\frac{u_c(\text{THR})}{THR})^2 + (\frac{u_c(I)}{I})^2} \quad \text{(G9)}$$

with $(\frac{u_c(\text{THR})}{THR})$ = 5.5 % from Table G1 and $\frac{u_c(\text{I})}{I}$ from Eq. G8, then Eq. G9 is estimated as 24 % for Tests 1-10 and 11 % for Tests 11-18.

G.2. Uncertainty Estimate of $HRR'_m(t = t_{peak})$

The uncertainty in the peak of the corrected HRR based on the radiative heat flux in Eq. G2 is related to the uncertainties in the total heat release measured by calorimetry (THR), the total mass loss measurement, and the mass loss rate at the time of the peak:

$$\frac{U_c\left(HRR'_{m\_peak}\right)}{HRR'_{m\_peak}} = 2\sqrt{(\frac{u_c(\text{THR})}{THR})^2 + (\frac{u_c(\Delta m)}{\Delta m})^2 + (\frac{u_c\left(MLR(t_{peak})\right)}{MLR(t_{peak})})^2} \quad \text{(G10)}$$

where the first two terms are given in Table 8. The last term is related to biases associated with the central differencing scheme (which was used to calculate the peak from the load cell measurements) as well as the data recording frequency. Here, both of these biases are treated as uncertainties. The central differencing scheme was good to first order. Consideration of second order terms in the Taylor series expansion of $\dot{m}$ leads to an uncertainty estimate of:

$$u_{trunc} \approx \frac{\Delta t^2}{6} \left|\frac{d^2\dot{m}\ (t_{peak})}{dt^2}\right| \quad \text{(G11)}$$

where Δt is the data acquisition time step equal to 1 s and 0.1 s for Tests 1-10 and Tests 11-18, respectively. The $\frac{d^2\dot{m}}{dt^2}$ term is always negative about a maxima, so the peak value is always underestimated.

Because the time rate of change of the mass ($\Delta\dot{m}$) is relatively fast compared to the recording frequency, the peak may be missed. In a worst case, the true peak occurs exactly halfway between two recording intervals. Near the peak, the signal profile can be approximately modeled as a parabola:

$$\dot{m}_{recorded\ peak}(t_{peak}) = \dot{m}_{true\ peak} + \frac{d\dot{m}(t_{peak})}{dt}\,(t - t_{true}) - \frac{1}{2}\,\frac{d^2\dot{m}(t_{peak})}{dt^2}\,(t - t_{true})^2 \quad \text{(G12)}$$

where $\frac{d\dot{m}}{dt} = 0$ at the true peak. At worst, the term $(t\text{-}t_{true}) = \pm \frac{1}{2}\,\Delta t$, so Eq. G12 becomes:

$$\dot{m}_{true\ peak} - \dot{m}_{recorded\ peak} = -\frac{1}{2}\,\frac{d^2\dot{m}(t_{peak})}{dt^2}\,(\tfrac{1}{2}\,\Delta t)^2 = -\frac{\Delta t^2}{8}\left(\frac{d^2\dot{m}(t_{peak})}{dt^2}\right) \quad \text{(G13)}$$

and the error in the peak due to the recording frequency is then less than:

$$u_{rec\_freq} = \frac{\Delta t^2}{8}\left|\frac{d^2\dot{m}(t_{peak})}{dt^2}\right| \quad \text{(G14)}$$

The value of $u_c\big(MLR(t_{peak})\big)$ must consider u_{rec_freq} and u_{trunc} (Eq. G11)

$$u_c\big(MLR(t_{peak})\big) = \sqrt{\left(\frac{\Delta t^2}{6}\left(\frac{d^2\dot{m}(t_{peak})}{dt^2}\right)\right)^2 + \left(\frac{\Delta t^2}{8}\left(\frac{d^2\dot{m}(t_{peak})}{dt^2}\right)\right)^2} \approx \frac{\Delta t^2}{10}\left|\frac{d^2\dot{m}\,(t_{peak})}{dt^2}\right| \quad \text{(G15)}$$

Increasing the data recording frequency ($1/\Delta t$) by an order of magnitude for Tests 11-18 significantly reduced the uncertainty of $u_c\big(MLR(t_{peak})\big)$. For this reason, it is convenient to group the uncertainty results by the data recording rate. Consideration of the mass loss rate profiles near the peak yielded a mean value of $\left|\frac{d^2\dot{m}\,(t_{peak})}{dt^2}\right|$, which is listed in **Error! Reference source not found.** along with the relative uncertainty of MLR (Eq. 15) for the two data recording frequencies.

Table G 2. Summary of $u_c\big(MLR(t_{peak})\big)$ for Tests 1-7 and Tests 13-18.

Tests*	Data rate (Hz)	Δt^2 (s^2)	$\left\|\frac{d^2\dot{m}}{dt^2}\right\|$ (g/s^3)	$\left(\frac{u_c(MLR(t_{peak}))}{MLR(t_{peak})}\right)$ (-)
1 – 7	1	1	14	0.034
13 - 18	10	0.01	76	0.0007
* mass loss rate data is not available for Tests 8 -12				

Referring to Eq. G10, on-average for all the tests, $\frac{u_c(\mathrm{THR})}{THR} = 5.5\ \%, \frac{u_c(\Delta m)}{\Delta m} = 4.4\ \%,$ and $\frac{u_c(MLR((t_{peak}))}{MLR(t_{peak})}$ is equal to 3.4 % or less as seen in **Error! Reference source not found.**, yielding values of 16 % and 14 % for $\frac{U_c(HRR'_{m\_peak})}{HRR'_{m\_peak}}$ for Tests 1-7 and Tests 13-18, respectively.

G.3. Uncertainty Estimate of the Time of the Peak Heat Release Rate

The time to the peak of the corrected HRR profiles in Eqs. G1 and G2 are considered in terms of the instrument time response, the data acquisition rate, the data recording frequency, and the signal to noise ratio. As previously stated, data was acquired at 200 Hz and recorded at 1.0 s and 0.10 s intervals for Tests 1 – 10 and Tests 11-18, respectively. The Huskeflex SGB01 thermal heat flux sensor has a time constant of 450 ms [Huskeflex], about 20 times faster than the calorimetry system. Strain gauge type devices such as the load cell are very fast, with time constants on the order of 1 ms to 10 ms.

The total uncertainty in the time to peak is estimated by combining the uncertainty contributions associated with the sensor lag (time response), the time discretization error, and the combination of the time averaging and the recording interval.

When the highest point is picked on a profile with a maxima, the true physical peak always occurs between the recorded data. This error can be modeled as a uniform rectangular distribution spanning ±½ Δt (the recording interval) about the recorded peak with the standard uncertainty given as:

$$\mathrm{u}_d = {}^{\frac{1}{2}}\Delta\mathrm{t}\Big/\sqrt{3} = 0.29\ \Delta\mathrm{t} \qquad \text{(G16)}$$

which is equal to 0.29 s and 0.029 s for the 1.0 s and the 0.1 s recording intervals, respectively.

An uncorrected delay (u_{ri}) of Δt/2 due to the recording interval, equal to 0.5 s and 0.05 s for the 1.0 s and the 0.1 s recording intervals, respectively, must be considered because the data acquisition system records a time averaged value following the end of the acquisition interval. This delay affects the recorded peak time, treated here as an uncertainty.

Lastly, the time constant of the sensors (450 ms and 10 ms for the Huskeflex heat flux gauges and the load cells) add an uncorrected time lag (u_s) to the uncertainty of the peaks of the HRR'_{q_peak} and HRR'_m profiles, respectively.

The total uncertainty can then be estimated for Tests 1 – 10 as:

$$u(HRR'_{q\_peak}) = \sqrt{(u_d)^2 + (u_{ri})^2 + (u_s)^2} = \sqrt{0.29^2 + 0.5^2 + 0.45^2} = 1.5 \text{ s} \quad \text{(G17)}$$

$$u(HRR'_{m\_peak}) = \sqrt{(0.29\ s)^2 + (0.5\ s)^2 + (0.01 \text{ s})^2} = 1.2 \text{ s} \quad \text{(G18)}$$

and for Tests 11 – 18 as:

$$u(HRR'_{q\_peak}) = \sqrt{(0.029\ s)^2 + (0.05\ s)^2 + (0.45 \text{ s})^2} = 0.91 \text{ s} \quad \text{(G19)}$$

$$u(HRR'_{m\_peak}) = \sqrt{(0.029\ s)^2 + (0.05\ s)^2 + (0.01 \text{ s})^2} = 0.12 \text{ s} \quad \text{(G20)}$$

The uncertainty results using Eqs. G19 and G20 are presented in Table G1 as expanded uncertainties $(2u)$.

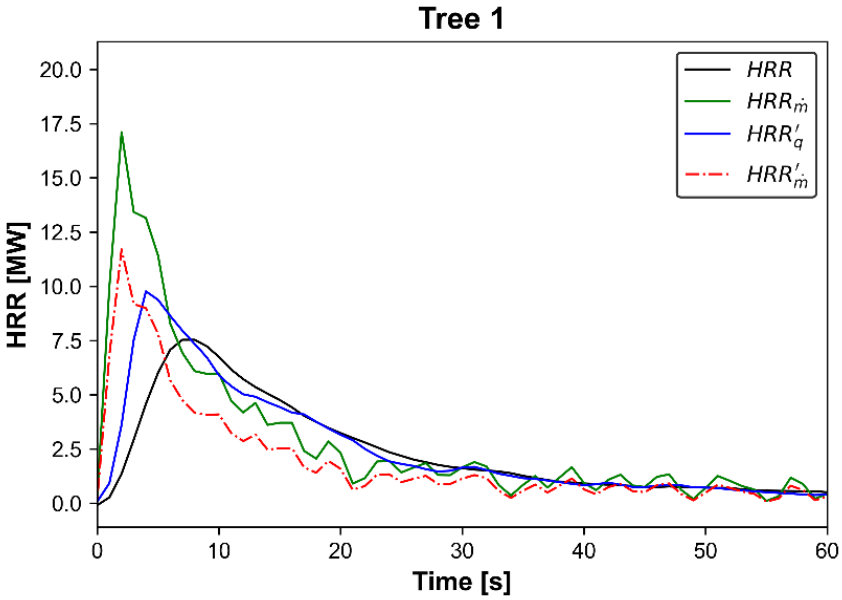

Figure G 1. The measured transient heat release rate (HRR), the calculated HRR based on the measured transient mass loss rate, and the corrected HRR profiles for Tree 1 based on the measured transient heat flux and mass loss rate profiles using Eqs. G1 and G2.

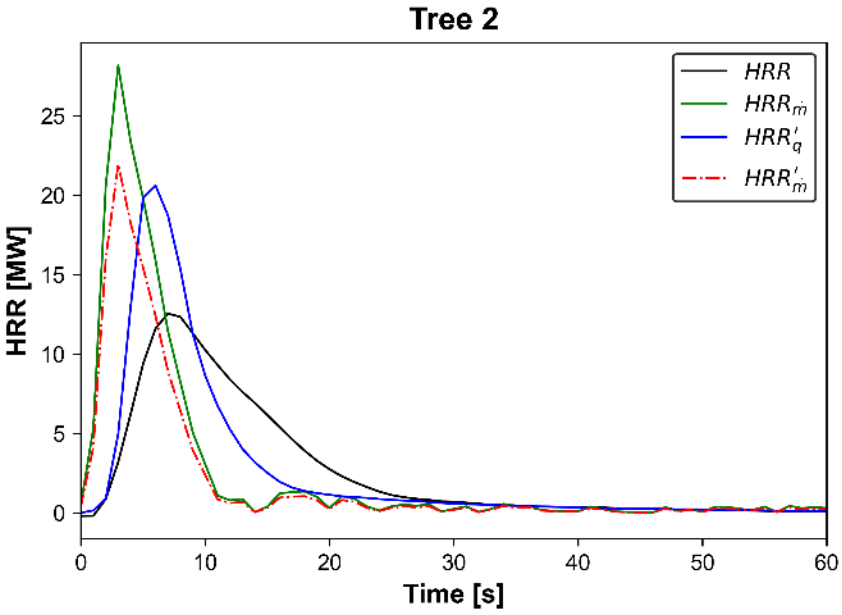

Figure G 2. The measured transient heat release rate (HRR), the calculated HRR based on the measured transient mass loss rate, and the corrected HRR profiles for Tree 2 based on the measured transient heat flux and mass loss rate profiles using Eqs. G1 and G2.

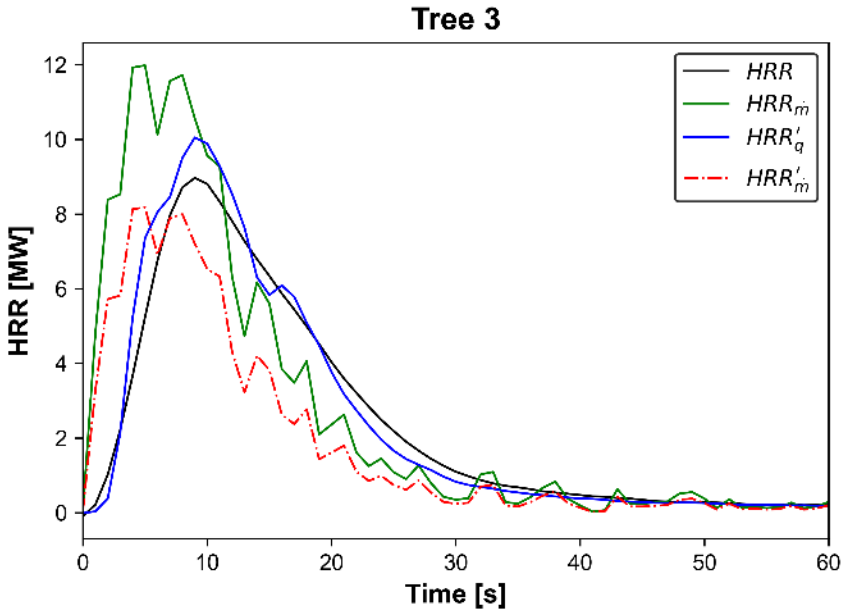

Figure G 3. The measured transient heat release rate (HRR), the calculated HRR based on the measured transient mass loss rate, and the corrected HRR profiles for Tree 3 based on the measured transient heat flux and mass loss rate profiles using Eqs. G1 and G2.

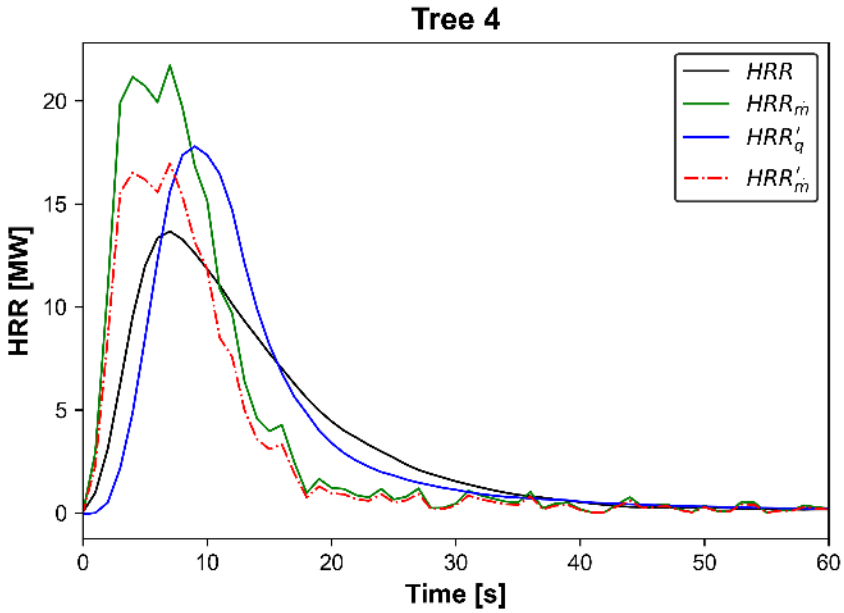

Figure G 4. The measured transient heat release rate (HRR), the calculated HRR based on the measured transient mass loss rate, and the corrected HRR profiles for Tree 4 based on the measured transient heat flux and mass loss rate profiles using Eqs. G1 and G2.

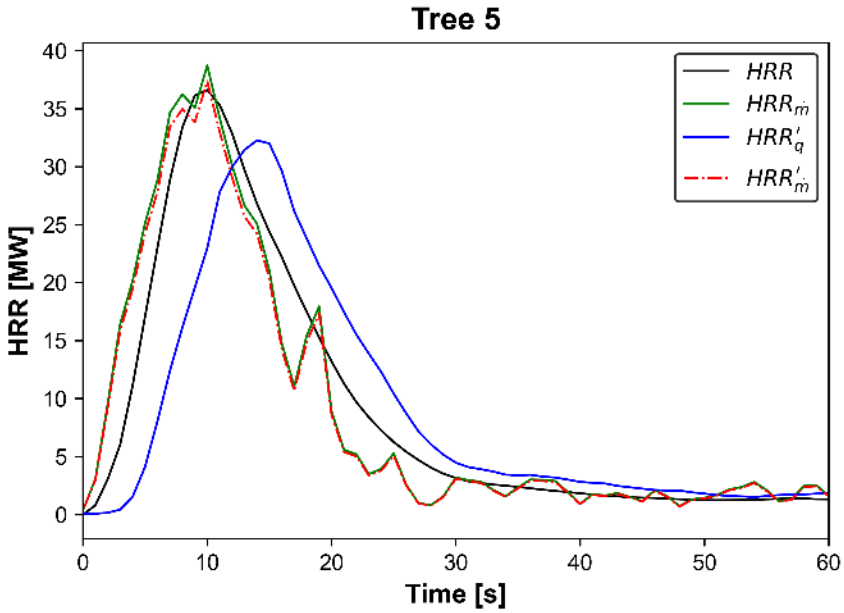

Figure G 5. The measured transient heat release rate (HRR), the calculated HRR based on the measured transient mass loss rate, and the corrected HRR profiles for Tree 5 based on the measured transient heat flux and mass loss rate profiles using Eqs. G1 and G2.

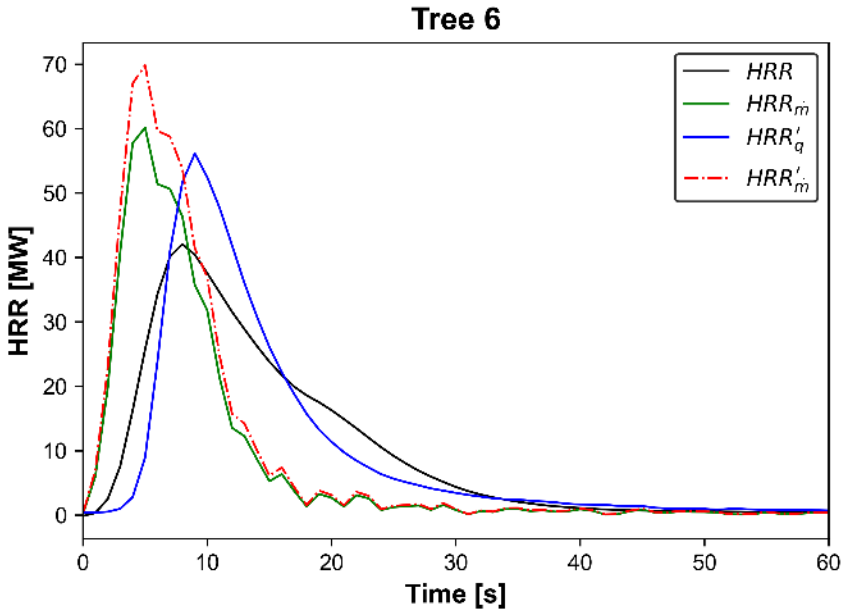

Figure G 6. The measured transient heat release rate (HRR), the calculated HRR based on the measured transient mass loss rate, and the corrected HRR profiles for Tree 6 based on the measured transient heat flux and mass loss rate profiles using Eqs. G1 and G2.

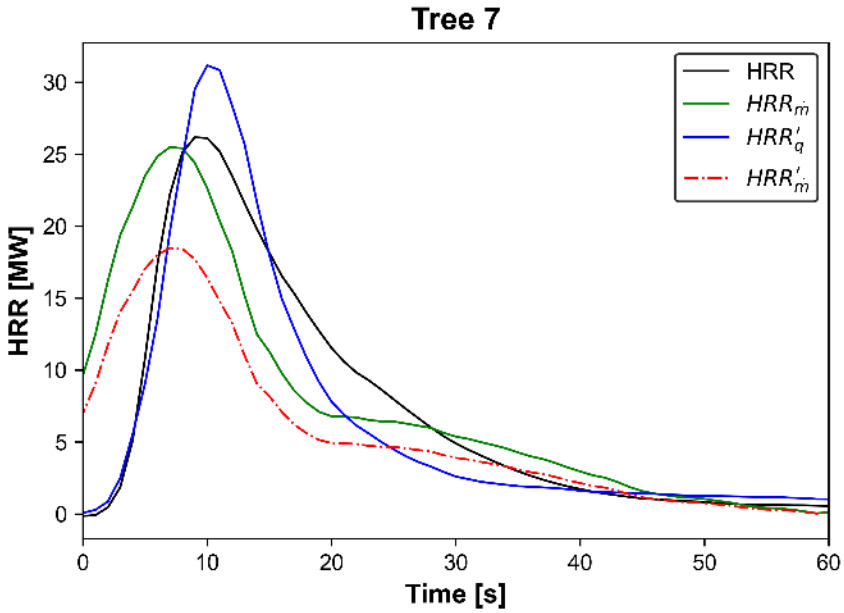

Figure G 7. The measured transient heat release rate (HRR), the calculated HRR based on the measured transient mass loss rate, and the corrected HRR profiles for Tree 7 based on the measured transient heat flux and mass loss rate profiles using Eqs. G1 and G2.

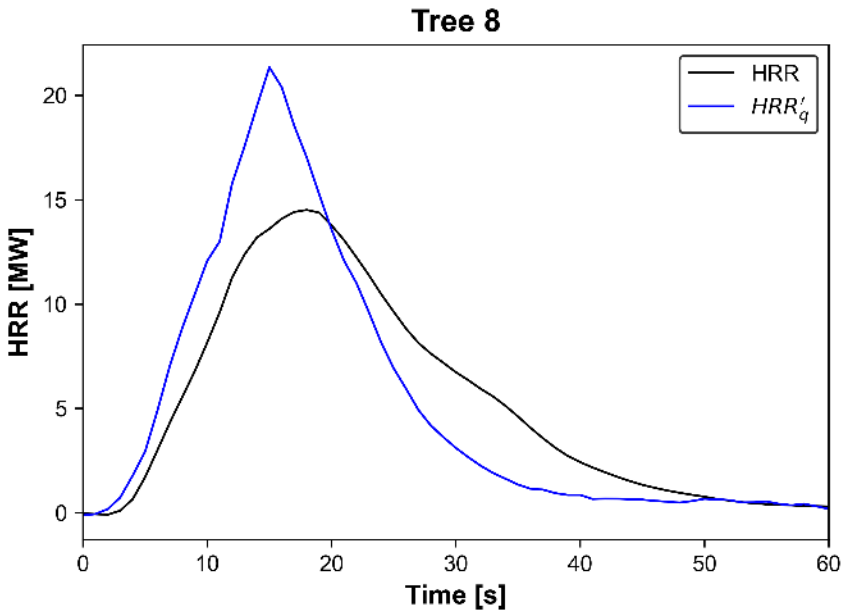

Figure G 8. The measured transient heat release rate (HRR) and the corrected HRR profiles for Tree 8 based on the measured transient heat flux rate profile using Eq. G1.

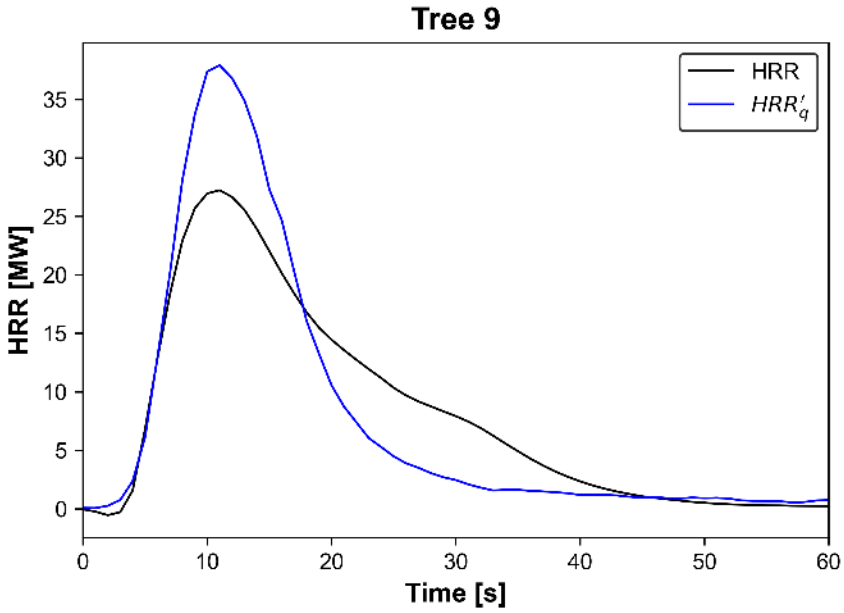

Figure G 9. The measured transient heat release rate (HRR) and the corrected HRR profiles for Tree 9 based on the measured transient heat flux rate profile using Eq. G1.

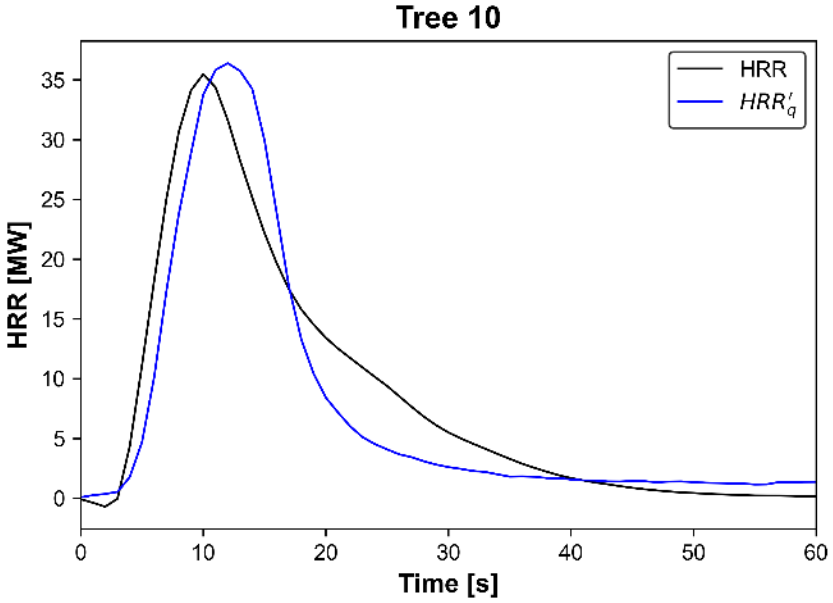

Figure G 10. The measured transient heat release rate (HRR) and the corrected HRR profiles for Tree 10 based on the measured transient heat flux rate profile using Eq. G1.

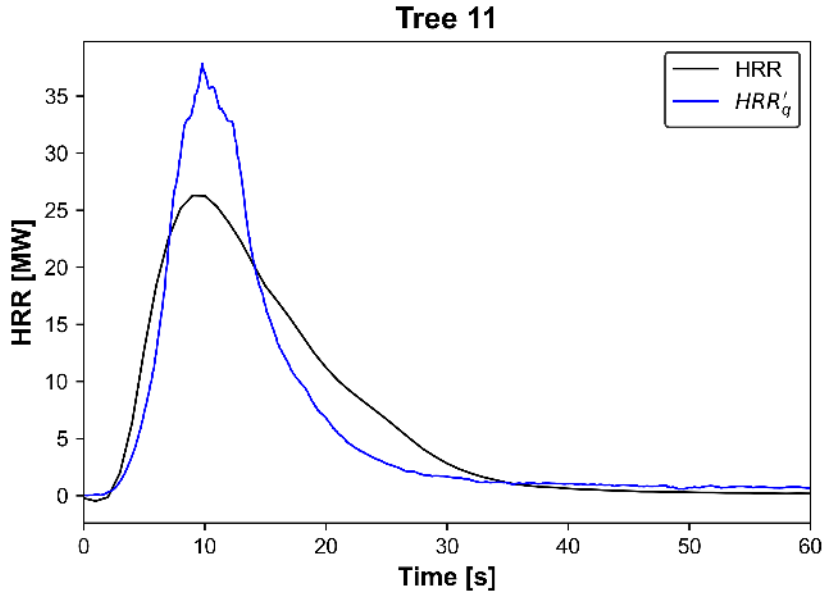

Figure G 11. The measured transient heat release rate (HRR) and the corrected HRR profiles for Tree 11 based on the measured transient heat flux rate profile using Eq. G1.

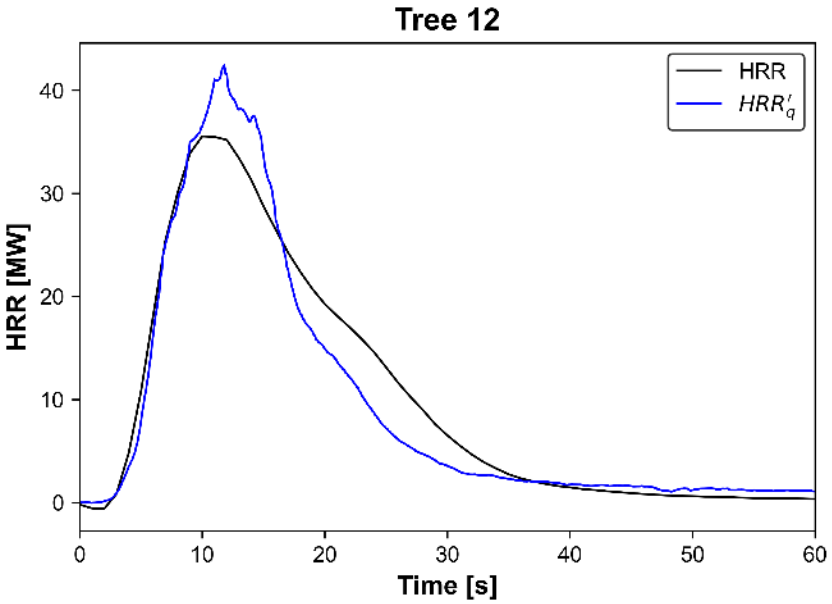

Figure G 12. The measured transient heat release rate (HRR) and the corrected HRR profiles for Tree 12 based on the measured transient heat flux rate profile using Eq. G1.

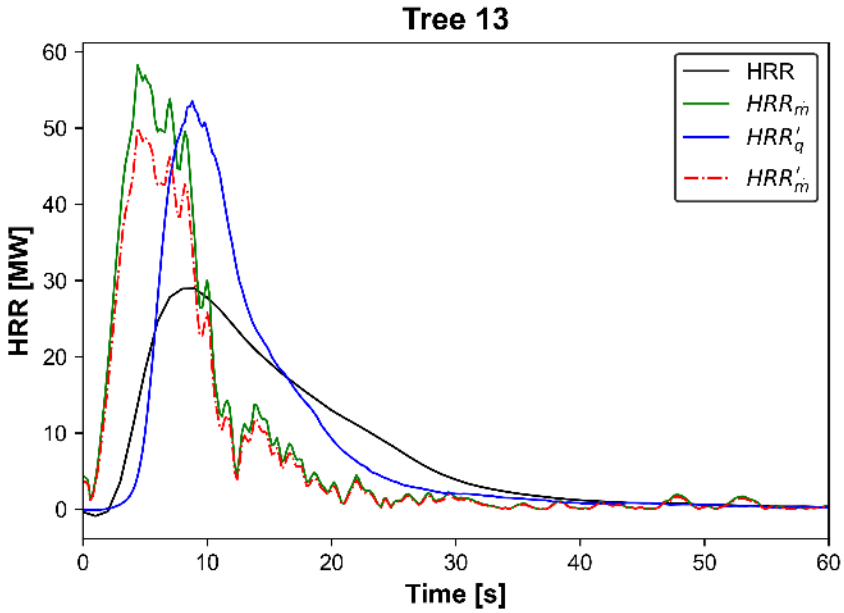

Figure G 13. The measured transient heat release rate (HRR), the calculated HRR based on the measured transient mass loss rate, and the corrected HRR profiles for Tree 13 based on the measured transient heat flux and mass loss rate profiles using Eqs. G1 and G2.

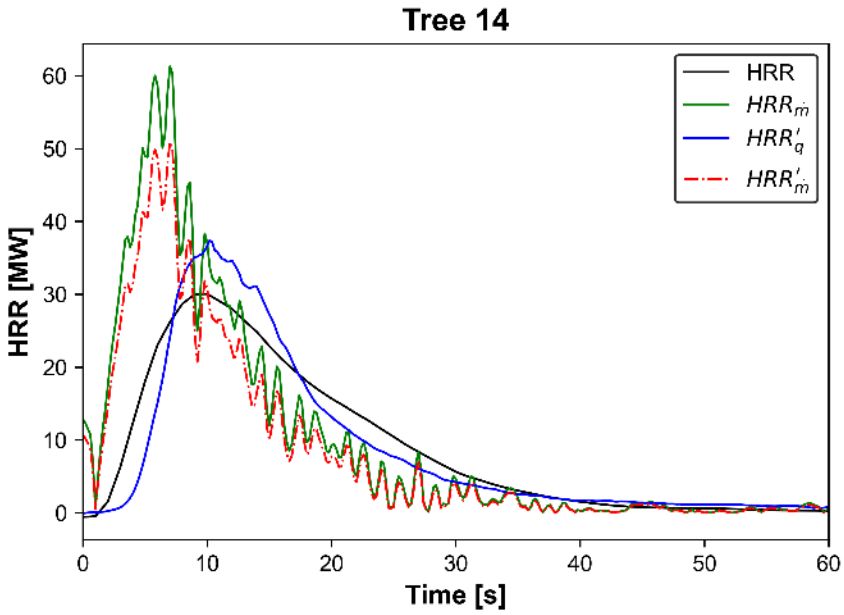

Figure G 14. The measured transient heat release rate (HRR), the calculated HRR based on the measured transient mass loss rate, and the corrected HRR profiles for Tree 14 based on the measured transient heat flux and mass loss rate profiles using Eqs. G1 and G2.

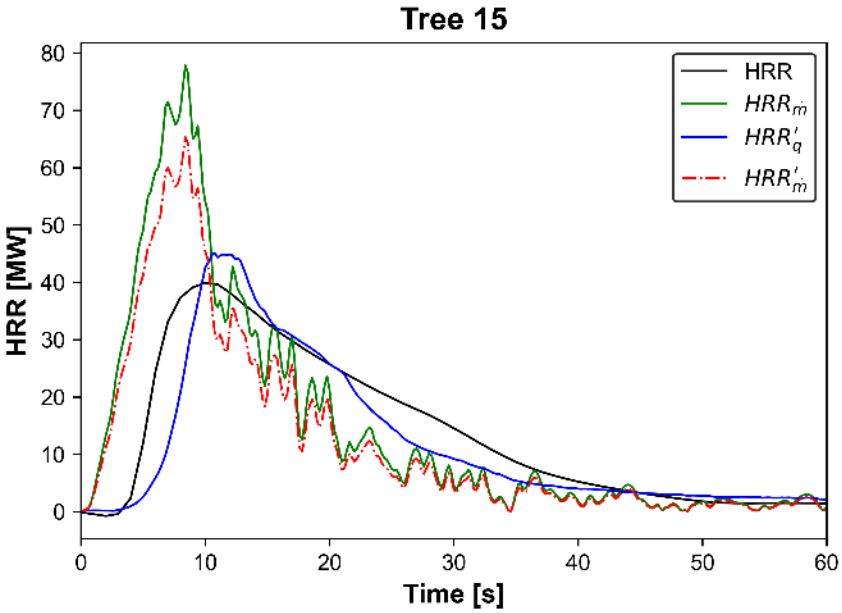

Figure G 15. The measured transient heat release rate (HRR), the calculated HRR based on the measured transient mass loss rate, and the corrected HRR profiles for Tree 15 based on the measured transient heat flux and mass loss rate profiles using Eqs. G1 and G2.

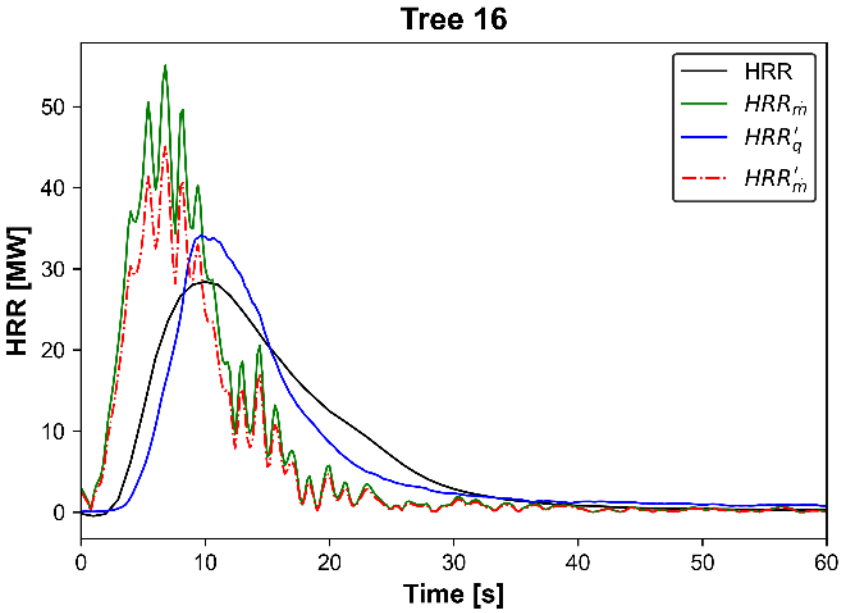

Figure G 16. The measured transient heat release rate (HRR), the calculated HRR based on the measured transient mass loss rate, and the corrected HRR profiles for Tree 16 based on the measured transient heat flux and mass loss rate profiles using Eqs. G1 and G2.

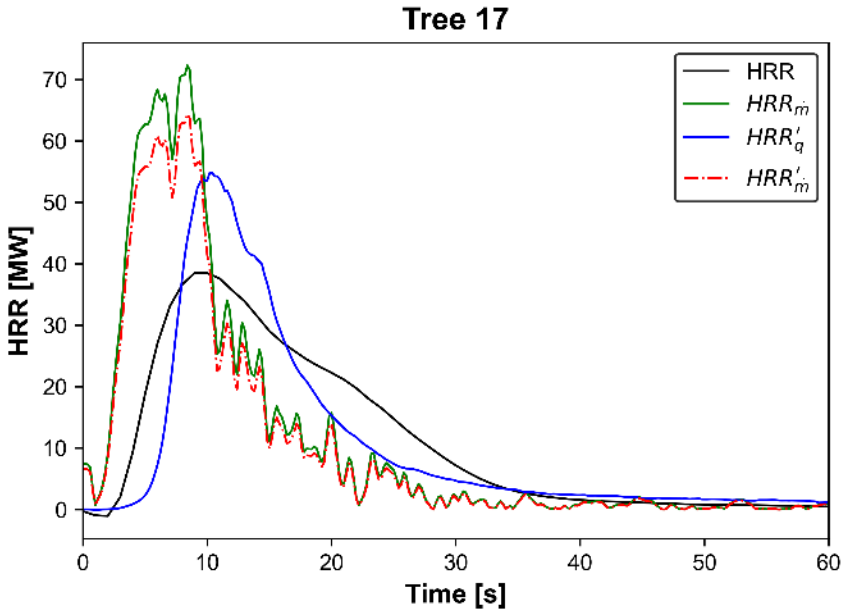

Figure G 17. The measured transient heat release rate (HRR), the calculated HRR based on the measured transient mass loss rate, and the corrected HRR profiles for Tree 17 based on the measured transient heat flux and mass loss rate profiles using Eqs. G1 and G2.

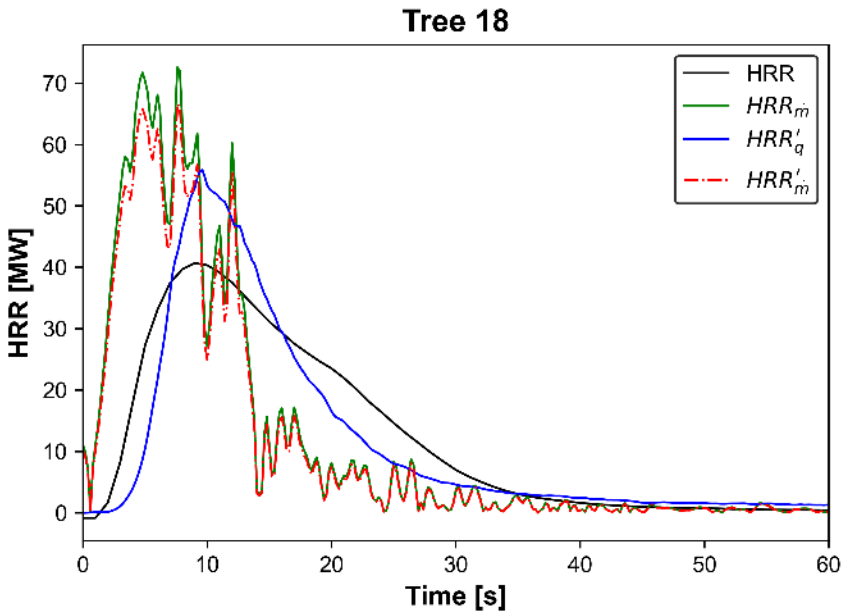

Figure G 18. The measured transient heat release rate (HRR), the calculated HRR based on the measured transient mass loss rate, and the corrected HRR profiles for Tree 18 based on the measured transient heat flux and mass loss rate profiles using Eqs. G1 and G2.